POLITECNICO DI TORINO

Master's Degree Program in Nanotechnologies for ICTs

Master's Degree Thesis

High-throughput measurement of mass at the attogram scale for nanoparticles in solution using Suspended Nanochannel Resonators

Supervisor

prof. Carlo Ricciardi

Candidate

Marco GAGINO

student ID: 255228

Internship Supervisor

Vincent Agache

ACADEMIC YEAR 2018-2019

Abstract

In this Master's Degree Thesis work I present the technological improvements of the Suspended Nanochannel Resonator (SNR) buoyant mass sensor technology developed in collaboration between the Manalis lab at the Koch Institute for Cancer Research – MIT and the CEA/Leti research center in Grenoble, France. $\sim 100nm$ thick piezoresistive gauges have been embedded in the hollow cantilevers of the SNR devices to allow a fully electrical piezoresistive readout mechanism of the beam's resonance frequency. This achievement made it possible to design arrays of SNR sensors that are fluidically connected either in series or in parallel to perform different functions. Here, I compare the piezoresistive readout mechanism to the previously used optical lever scheme showing that they have equivalent performances: the optimized design of the piezoresistive gauge element has no negative impact on the SNR noise and a limit of detection in the attogram order of magnitude can be achieved. Then, I describe the parallel SNR array technology and the way I characterized its performances and compared them to the well-established single-resonator SNR. The results show an order of magnitude improvement in the measurement throughput of nanoparticles with buoyant mass down to $10ag$, in aqueous solutions at concentrations as low as 10^8 particles/mL; polydisperse samples of particles with different sizes and mass can be measured using this technology and less than $20nm$ resolution in size difference can be achieved for gold nanoparticles.

The simultaneous implementation of piezoresistive gauges for electrical readout and of parallel SNR arrays effectively lowers the measurement time for this technology making it competitive with other established techniques for mass sensing in solution: future industrial applications are envisioned.

Acknowledgements

I would like to thank many people for the help and support that I was given during my training period in Boston and, overall, throughout the length of my Master's Degree.

First and foremost, my gratitude goes to my internship supervisor Vincent Agache for guiding me, training me and giving me the opportunity to work on a stimulating research topic, and to my colleague Georgios Katsikis who gave me several insights on how to improve as a researcher and encouraged me to apply for a PhD program.

In addition I thank Scott Manalis for hosting me in his laboratory at MIT and giving me encouraging feedback on my work, and all the people working in the Manalis lab: I had a great time with you all. In particular I would like to thank Max Stockslager, Mary Mu, and Scott Knudsen for the practical support to my work, the CTC team for the laughs we shared while working, and the people in the write-up room.

I would like to thank the CEA/Leti research center for sponsoring my training period in a foreign university.

Finally, thank you to my family, my friends, my Nanotech fellows, and all the people that I have met in the past two years while studying for the Master's Degree for the amazing support and the experiences we shared. Thank you to Marco Liffredo, Alberto Nardi, Nicolò Petrini and Giulio Tidei: Nanotech and Boston wouldn't have been the same without you guys.

Contents

List of Tables v

List of Figures vi

Introduction 1

1 Suspended Nanochannel Resonators allow for the measurement of mass of nanoparticles in solution at the attogram scale 7

1.1 SNR working principle: the resonance frequency of a cantilever depends on the added mass of nanoparticles 8

1.2 Family of SNR devices 12

1.2.1 Buoyant mass measurement with SNR 13

1.2.2 Parallel array SNR design 16

1.2.3 Density SNR design 18

2 Design and manufacturing of SNR devices embedding shallow piezoresistive gauges 21

2.1 The geometrical properties of SNR and the piezoresistive gauges are optimized for mass sensing at the attogram scale 22

2.1.1 Algorithm for minimization of mass limit of detection 25

2.1.2 Less than 1% variation in mass detection occurs around its optimal point 26

2.1.3 Optimization of parameters with doping profile simulation . 29

2.2 Manufacturing steps of SNR devices 32

2.2.1 Bottom SOI wafer: buried channels 32

2.2.2 Top SOI wafer: piezoresistor, electrical path and insulation . 34

2.2.3 Glass wafer: fluidic bypass channels and inlet ports 41
2.2.4 Silicon wafer: vacuum getter support 42

3 Exploring the capabilities of SNR sensors through simultaneous piezoresistive readout of multiple resonators 45
3.1 Piezoelectric driving of resonators and resonance frequency detection methods 46
3.2 How does the optical readout compare to the piezoresistive readout? 50
3.3 Measuring properties of pSNR and its figures of merit 52
3.3.1 pSNR allows for a 9-fold increase in throughput 54
3.3.2 Trading off transit time of nanoparticles with measurement bandwidth in pSNR 57
3.3.3 The limit of detection of buoyant mass is 10 ag for pSNR . . 62
3.3.4 The dynamic range of detection of pSNR is limited at high concentrations 64
3.3.5 pSNR can measure polydisperse samples 66

4 Conclusions and outlook 71

A Nomenclature of geometrical and material properties of SNR 77

B Measurement setups and LabVIEW scripts for SNR operation 79

C Results of optimization algorithm 83

D T7-like virus buoyant mass measurement and limit of detection threshold 86

E Flaws of pSNR current technology 87

List of Tables

1.1 Summary of single-resonator SNR geometrical properties and resonance frequency. 15
1.2 Summary of pSNR geometrical properties and resonance frequency. 17
1.3 Summary of density SNR design geometrical properties and resonance frequency. 19
2.1 Optimization parameters that the algorithm derived based on the boundary conditions and performances constraints reported here. . 24
A.1 Nomenclature of geometrical and material properties of SNR. 78
C.1 Design parameters for different types of single-resonator SNR devices (table 1.1) obtained using the optimization algorithm described in chapter 2. 84
C.2 Design parameters for single-resonator SNR devices and one of the resonators in the *A1* pSNR device (see tables 1.1, 1.2) obtained using the optimization algorithm described in chapter 2 after the parametric sweep study and using the dopant profile simulated with the SILVACO software. 85

List of Figures

1.1 Working principle of a Suspended Nanochannel Resonator 9

1.2 (a) First, second and third mode normalized oscillation amplitudes vs the normalized cantilever length. (b,c,d) Relative resonance frequency shift consequent to a nanoparticle flowing through the U-shaped buried channel embedded in the SNR when the cantilever oscillates at its first (b), second (c) or third (d) mode. 11

1.3 SEM images of the U-shaped buried channel embedded in an earlier architecture of SNR and optical microscope image of a single-resonator SNR device. 14

1.4 Schematics of a particle going through the fluidic channels of a single-resonator SNR device from the sample-load bypass (pinched flow pressures mode), through the buried channel, to the sample-collect bypass. 14

1.5 Optical microscope image of a parallel SNR array (top) and schematic of a particle going through the fluidic channels of a pSNR (bottom). 18

1.6 Optical microscope image of a density SNR design showing the mixer between the middle bypass channel and the buried channel of a D0 type (left). Schematics of a particle going through the fluidic channels of a density SNR design (right). 19

2.1 Cross sectional view of a SNR device showing the vacuum chamber were resonators are free to oscillate in. 23

2.2 Cross sectional view of a SNR cantilever. 24

2.3 Mass resolution of one of the resonators in a pSNR array (SNR#10 in *A1*) plotted as a function of the normalized piezoresistive gauge length, the normalized piezoresistive gauge thickness and the p-dopant concentration. 27
2.4 Mass resolution of one of the resonators in a pSNR array (SNR#10 in *A1*) plotted as a function of the normalized piezoresistive gauge length and the normalized piezoresistive gauge thickness. 28
2.5 Mass limit of detection of a resonator in the pSNR array (SNR#10, in *A1*) vs p-dopant ion implantation dose and energy. Results of a SILVACO simulation that takes into account the presence of a $10nm$-thick screen oxide layer used during the implantation steps. The dashed line represents the thermomechanical limit for this device. 30
2.6 Variation of estimated limit of mass detection throughout the resonators in pSNR arrays of type *A0* and *A1* due to the design choice of fixing the piezoresistance value R_{pzr} of the gauge in all cantilevers of the array. 30
2.7 Summary of optimization steps used to design the geometrical parameters of the SNR resonator, the buried channel and the piezoresistive gauge. 31
2.8 Doping profile of the n-type Silicon device layer of the bottom SOI after epitaxial growth of the $520nm$ Silicon layer. 33
2.9 Schematic of the bottom SOI wafer after epitaxial growth of n-doped Silicon $520nm$, growth of the $7nm$ thick top thermal oxide (step 1), and etching of the $700nm$ deep buried channel (halfway through step 2). 34
2.10 Cross section of top and bottom SOI wafers after thermal oxide is grown on both Silicon device layers (step 2 and 3), front-side fusion bonding of the wafers and removal of Silicon bulk and BOX layer of the top SOI wafer (step 3). 35
2.11 Simulation of the doping profile of the Silicon device layers of the top and bottom SOI wafers after full-sheet implantation of Phosphorous in the top Silicon layer and annealing step. 36
2.12 Simulations of the p-type doping profile after patterning of P++ conductive traces and annealing step. 37

2.13 Simulations of the n-type doping profile after patterning of N+ isolation traces and annealing step. 38
2.14 Simulations of the p-type doping profile after patterning of P++ piezoresistive elements and spike annealing step. 39
2.15 Cross section of top and bottom SOI wafers after the implantation steps that defined the piezoresistive gauge, the conductive paths and the isolation traces (step 4), the passivation of the top Silicon layer (shown in green) and the deposition of the metal pads (step 5). . . 40
2.16 Cross section of top and bottom SOI wafers after the removal of the PECVD TEOS layer from the surface of the SNR resonator, and the etching of the U-shaped trench around the cantilever and the bypass-to-buried channels inlet port (step 6). The *A-A'* section is reported in figure 2.2 41
2.17 Cross section of the glass wafer after etching of the bypass channels, SNR domes, and recess above the metal pads; the fluidic inlet ports are etched through the wafer thickness via ultrasonic drilling (step7). 42
2.18 Cross section of the glass wafer and the SOI stack after anodic bonding, grinding of the SOI backside Silicon bulk, patterning of the $5\mu m$ wide ditches and release of the SNR resonators through drilling of a cavity in the underlying Silicon and BOX layers (step 8). 43
2.19 Cross section of the Silicon wafer after gold deposition for eutectic bonding, $200\mu m$ Silicon etchig and getter deposition (step 9). 43
2.20 Cross section of the full stack of Silicon/SOI/SOI/glass wafers being patterned and implanted to manufacture SNR devices of different types. The eutectic bonding of the bottom Silicon wafer with the SOI/glass wafers stack is shown (step 9). 44
3.1 Schematics of the optical setup readout mechanism for the SNR's closed-loop resonance frequency detection and driving of the piezoceramic actuator. 47
3.2 Schematics of the piezoresistive setup readout mechanism for the SNR's closed-loop resonance frequency detection and driving of the piezoceramic actuator. 48
3.3 Yield statistics of tested pSNR arrays. 50

3.4 Comparison of Allan deviation analyses based on noise measurements performed with the same *SNR1* device on the electrical and optical readout systems. 53
3.5 Comparison of 80nm-diameter gold nanoparticles count events in a 44 minutes long experiment between a single-resonator SNR and a parallel array of SNRs. 54
3.6 Summary of throughput and transit time per cantilever in pSNR and a single-resonator SNR. 55
3.7 Buoyant mass histograms resulting from each of the 9 SNRs in the parallel array used for this analysis. 56
3.8 Simulation of the normalized time-dependent resonance frequency signal of a cantilever oscillating at its first flexural mode when a nanoparticle flows through the U-shaped buried channel. 58
3.9 Energy recovery vs particles transit time of the resonance frequency signal being filtered by the CIC filter of order m and with a bandwidth BW with respect to the unfiltered signal. 59
3.10 Ratio of filtered and unfiltered resonance frequency shift peak heights vs particles transit time. 60
3.11 Estimated sample diameter vs particles transit time through the U-shaped buried channel of a SNR. 61
3.12 The resonance frequency shift distortion of a high-speed 80nm-diameter gold nanoparticle going through the SNR is the cause of the mass underestimation. The plot shows the resonance frequency shift caused by two particles travelling at the transit time limit and below it. . . 61
3.13 Allan deviation analysis of a pSNR device of type *A1* with 8 resonators working in piezoresistive mode. 63
3.14 Quality factor statistics of tested pSNR arrays. 64
3.15 Dynamic range of measurement throughput (number of counted particles through the SNR per minute) with respect to sample concentration of 40nm-diameter gold nanoparticles. 65
3.16 Time snapshot of the first-mode resonance frequency shift consequent to the flow of 40nm-diameter gold nanoparticles through the buried channel of an SNR; the sample is highly concentrated (9 10^{10} particles/mL) and double-occupancy events occur. 66

3.17 Polydisperse sample of $20nm$, $40nm$, $60nm$-diameter gold nanoparticles measured through a pSNR array of type *A1*. 67
3.18 Time snapshot of the resonance frequency shift consequent to the flow of gold nanoparticles of different size through the buried channels of resonators in a pSNR array. 67
3.19 (a) Open-loop frequency sweep showing the resonance peaks of the SNR cantilevers in the pSNR array used for the analysis in figures 3.17 and 3.18.The quality factors of each of the four resonators in use are reported above each resonance peak. (b) Allan deviation analysis of the same resonators converted into limit of mass detection in attograms. The device in use has relatively high quality factors $Q \sim$ 2,000 and consequently has low limits of mass detection in the order of $10ag$. 68
3.20 Estimated transit times of $20nm$, $40nm$, $60nm$-diameter gold nanoparticles through the 4 active resonators in a pSNR array and comparison between transit times grouped according to nanoparticles size. 69
B.1 LabVIEW script used to control pressure levels in the four vials connected to the inlets of the two bypass channels of either a single-resonator SNR or a pSNR array. 79
B.2 LabVIEW script used to drive the piezoelectric ceramic in open-loop mode. 80
B.3 LabVIEW script used to drive the piezoelectric ceramic in closed-loop mode. 81
B.4 LabVIEW script used to display and save the resonance frequency shifts of N simultaneously locked resonators in a pSNR array. 82
D.1 Estimated buoyant mass of a T7-like virus measured in filtered ($200nm$) de-ionized water using a single-resonator SNR of type $SNR3$. . . . 86
E.1 Optical microscope image of a pSNR device showing air bubbles leaking into the de-ionized water filled vacuum chamber were resonators are sealed in. 87
E.2 Open-loop frequency sweep of two parallel SNR arrays of type showing the difference between a low quality factor device of type *A0* and a high quality factor device of type *A1*. 88

Introduction

The subject of nanometrology is of particular interest for industrial applications and in several research fields for the need of accurately measuring properties of nanomaterials, nano-objects and nanoparticles whose natures are either artificial or biological [1]. In the first case, particles of different chemical composition may result as byproducts of industrial processes and may cause health and environmental issues if not properly treated: for this class of so-called engineered nanoparticles (ENPs) properties such as size, chemical composition, surface area and surface charge are studied to characterize their reactivity. Biological samples of different nature and size scale such as cells [2, 3], bacteria [4], viruses [5, 6], exosomes [7] and assembled vesicles for drug-delivery [8] are often characterized in terms of size, mass, density and concentration to study their functions and composition and require instruments that are able to perform non-destructive measurements in aqueous solutions. Different technologies can be used for this purpose and all have their advantages and drawbacks when it comes to evaluating properties such as the limit of detection, the measurement speed, the ability to measure polydisperse samples, and the presence of restrictions on the nature of the nanoparticles that can be measured with a certain technique and/or the fluid in which they are suspended in [9]. The most relevant examples in biology-related nanometrology are the instruments based on light scattering such as the Dynamic and Static Light Scattering (DLS, SLS) [10, 11], the Resistive Pulse Sensing (RPS) technique [12, 13], and the Nanoparticle Tracking Analysis (NTA) [14]. DLS is based on the measurement of the light intensity fluctuations of a laser beam being scattered by particles in Brownian motion in an aqueous solution; the Stokes-Einstein equation is then used to derive the hydrodynamic radius of the analyte from the coefficient

of diffusion that can be extracted from the scattered light fluctuations measurement. This method is rapid (a few minutes are required to make an analysis) and relatively cheap, it has a wide dynamic range in terms of particles size ranging from a few nanometers to some tens of micrometers, it requires small volumes of sample, and it is compatible with solvents of different nature. Unfortunately though, DLS is based on the ensemble light scattering measurement of the whole sample which means that the size estimation is biased towards particles that have the highest scattering efficiency, typically the largest ones: polydisperse samples cannot be accurately measured using this technique. Similarly to DLS, NTA uses a high temporal-resolution video acquisition system and high contrast microscopy to extract the diffusion due to Brownian motion of individual particles in a sample: single particle resolution can thus be achieved. With this technique it is possible to measure plydisperse samples with particles hydrodynamic radii in the range of some tens of nanometers to some micrometers. However, there are some restrictions on the sample concentration which must be in the $10^8 - 10^9$ particles/mL range, the equipment is generally more expensive than DLS, and only highly scattering particles can be detected through this technique. RPS and Tunable RPS is based on the flow of nanoparticles through a pore which causes variations of ionic currents. Single particle resolution is also achieved with this technique, and with TRPS it is possible to change the size of the pore to maximize the dynamic range of particles size that can be measured; the drawback of this technology is that the medium in which the sample is suspended in has to be conductive. Suspended Micro/Nano-channel Resonator (SMR/SNR) devices [15, 16, 17] represent an innovative solution for the characterization of physical properties of biological samples such as buoyant mass, size, density, and stiffness. Nanoparticles are suspended in a fluid medium which is then forced to flow through a micro/nano-fluidic channel that is embedded in the core of a resonating beam. The small added mass of the nanoparticles that transit through the beam in a short period of time cause a shift in the resonance frequency that can be directly correlated to the physical properties of the analyte, mainly its buoyant mass. Single particle resolution can be achieved with SMR and SNR meaning that polydisperse samples can be measured with this technique. The sample concentration dynamic range is relatively wide and in the range of $10^8 - 10^{11}$ particles/mL; particles as small as a few tens of nanometers can be measured and there is no restriction on the nature of fluid where particles are

suspended in.

In the context of nanometrology for biological samples and with the goal of achieving attogram scale mass resolution for the characterization of nanometer scale biological matter such as viruses and exosomes, the Suspended Nanochannel Resonator (SNR) [18] technology was developed by miniaturization of the manufacturing procedures for the well-established SMR devices. Its operation and ability to measure biological samples of different nature such as exosomes and DNA origami-gold nanoparticles aggregates was demonstrated some years ago [19] using the optical lever readout scheme which is effective and sensitive but also bulky as it requires several optical components. Thanks to the collaboration of the Manalis lab at the Koch Institute for Cancer Research – MIT and the CEA/Leti research canter in Grenoble – France, a shallow piezoresistive readout gauge was successfully designed and embedded into the active element of the SNR device, the fixed-free hollow beam that contains a U-shaped fluidic nanochannel. This electrical element is innovative in the Micro/Nano Electro-Mechanical Systems (MEMS/NEMS) field as it must be carefully designed and precisely manufactured to avoid any electrical short-circuit with the fluid flowing underneath and at the same time its geometrical properties must be optimized to allow both a good signal-to-noise ratio of the electrical current flowing through the piezoresistor, and a limit of mass detection for the SNR sensor that would approach the thermomechanical limit of an oscillating resonator: at the scales of the current technology the mass resolution reaches a few attograms. The most effective way to embed the resonance frequency sensing unit into the device itself and get rid of the optical external apparatus is through the piezoresistive readout mechanism; in fact, its functionality has already been demonstrated in the SMR devices [20]. The alternative electrical readout mechanisms such as the capacitive [21, 22] and piezoelectric [23] sensing schemes are either not compatible with a fixed-free beam vibrating in its out of plane flexural modes or they do not allow for an optimal limit of mass detection. In fact, the capacitive sensing is less technologically challenging when implemented for in-plane cantilever vibrations rather than out of plane. Moreover, when the mechanical components are scaled down to the nanoscale the capacitive readout efficiency is reduced due to parasitic effects: the stray capacitances with the substrate, adjacent electrodes and interconnects overcome the transduction capacitance. The

piezoelectric sensing requires additional layers on the cantilevers to serve as the active transduction element and its electrodes: not only these additional layers add complexity to the manufacturing process but they also increase the stiffness and the effective mass of the resonator leading to a lower buoyant mass sensitivity. The advantage in having a fully-integrated electrical readout mechanism over an external optical apparatus is the ease of scaling the single-resonator configuration of the SNR technology to an array of resonators that are fluidically connected either in parallel or in series, allowing for different functions. Once again, this capability has already been demonstrated for SMR devices to measure single-cell growth rates through a serially connected array of resonators [2], but it has never been explored with the nanoscale version of the sensor so far. In the case of parallel arrays of SNR resonators, there is an increase in measurement throughput with respect to the single-resonator version: as a consequence, the time required for the sensor to analyze a nanoscale sample in solution is effectively reduced to some tens of minutes. The ability to measure mass down to some attograms in a relatively short time makes this technology competitive with respect to the previously described state-of-the-art instruments. For this reason, during my Master's Degree Thesis training period I adapted the existing SMR piezoresistive readout setup to be able to also sense signals from the SNR devices, and I compared the efficiency of the fully-electric readout mechanism to the optical lever scheme. Once this capability was fully optimized for single-resonator SNR devices, I explored the performances of the parallel SNR arrays and characterized their throughput, dynamic range of operation and ability to measure polydisperse samples.

In the following chapters I present the work that I carried out in the Manalis lab during my six months Master's Degree Thesis training period. In chapter 1 I describe the working principle of Suspended Nanochannel Resonator devices and how variations in the technology design allow for the exploitation of different functionalities; the parallel SNR array design is described here. In chapter 2 I show the design optimization rules that were carried out to embed the shallow piezoresistive gauge into the SNR devices and to reach the attogram order of magnitude mass resolution. Furthermore, I list the manufacturing steps that were used to fabricate the different types of SNR devices. In chapter 3 I give a review of the methods used to actuate the sensors and measure their resonance frequency variation which is directly correlated to the buoyant mass of the nanoparticles being measured. I also present the results of the characterization analysis I did to compare the performances of the piezoresistive readout mechanism with the optical lever scheme, and I demonstrate the capabilities of the parallel SNR array devices through the analysis of its measurement throughput, limit of mass detection, dynamic range of analyte concentration, and ability to measure polydisperse samples. Finally, in chapter 4 I give a summary of the manuscript, I talk about the future work that can be done to improve the parallel SNR technology and its piezoresistive readout method, and I present the envisioned outlooks for these sensors.

Chapter 1

Suspended Nanochannel Resonators allow for the measurement of mass of nanoparticles in solution at the attogram scale

Suspended Nanochannel Resonators (SNR) are NEMS nanofluidic devices that can measure the buoyant mass of a wide range of synthetic and biological nanoparticles in solution down to the attogram ($10^{-18}g$) scale. The working principle is simple: the resonance frequency of a hollow oscillating cantilever depends on the beam's mass which changes when particles in solution flow through a U-shaped fluidic channel of sub-micrometric cross-sectional dimensions which is embedded in the resonator. To increase the performances of this device, the cantilever is sealed inside a vacuum chamber that maximizes its quality factor by minimizing energy dissipation due to air damping. SNRs can in principle measure not only mass but also physical properties of particles at the nanoscale such as density and size through the Archimedes principle reaching resolutions of some attograms in buoyant mass and a few tens of nanometers in size for materials as dense as gold [19].

Moreover, the device allows for the detection of heterogeneous samples which can be suspended in any kind of medium, with no restrictions on its conductivity or fluorescence. These characteristics make SNR technology a better fit with respect to the techniques that are currently available on the market and that have been previously described when it comes to measuring biological matter in suspension such as viruses and exosomes. Light scattering methods (DLS, SLS) are not able to resolve polydisperse samples, current Tunable Resistive Pulse Sensing (TRPS) machines such as Spectradyne are not able to resolve particles below $50nm$ in size and require a conductive medium for the sample, Nanoparticle Tracking Analysis (NTA) can only sense highly-scattering or fluorescent nanoparticles[9].
In this chapter I will talk about the working principle of SNR resonators and present a few examples of applications of this technology that are currently being developed in the Manalis group at the Koch Institute, MIT. During my six months internship I have worked on some of these applications and in the next chapters I will focus deeper into the characterization experiments I have designed and performed to determine the efficiency of a piezoresistive readout mechanism for nanoresonators and to explore the capabilities of a specific variation of the SNR technology, the parallel SNR array.

1.1 SNR working principle: the resonance frequency of a cantilever depends on the added mass of nanoparticles

As mentioned in the introduction paragraph to this chapter, the SNR is a vacuum-sealed resonating cantilever which embeds a U-shaped buried channel (Figure 1.1); the latter is connected to two bypass channels which enable the loading of a sample containing nanoparticles dispersed in a buffer fluid (left bypass channel) and its collection (right bypass channel). The cantilever can be forced to oscillate at one of its flexural vibration modes, whose resonance frequency can be written as [24]:

$$\omega_r = \lambda_n^2 \sqrt{\frac{k}{m_{eff}}} \tag{1.1}$$

where λ_n is the modal eigenvalue such that $cos\lambda_n cosh\lambda_n + 1 = 0$, k is the cantilever

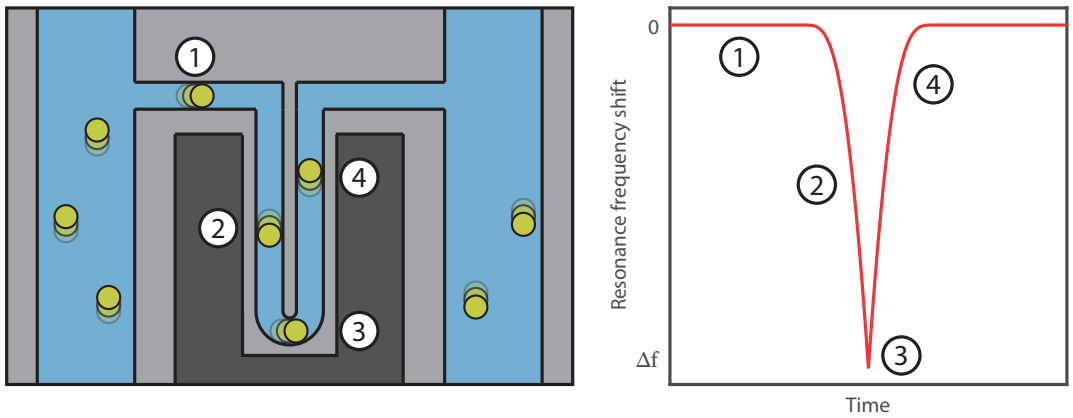

Figure 1.1. Working principle of a Suspended Nanochannel Resonator: a nanoparticle flowing through a U-shaped channel embedded in an oscillating cantilever causes a position-dependent variation in its resonance frequency. In the plot on the right side of the image, Δf is the maximum change in resonance frequency, when the particle reaches the tip of the cantilever. $\Delta f > 0$ when the particle's density is smaller than the fluid's; $\Delta f < 0$ if the particle's density is larger than the fluid's.

stiffness and m_{eff} is its effective mass which can be computed from its geometrical and material properties (for the symbols definitions refer to Appendix A).

$$m_{eff} = 0.25 \times m_{cantilever} = 0.25 \times [m_{lid,top} + m_{lid,bottom} + m_{middle}] \tag{1.2}$$

$$m_{lid,top} = m_{lid,bottom} = \rho_{Si} L_{res} w_{res} t_{lid} \tag{1.3}$$

$$m_{middle} = \rho_{Si} L_{res} w_{res} t_c + (\rho_{water} - \rho_{Si})\, w_c t_c \left[\pi\,(w_c + w_{int}) + 2\left(L_c - \frac{w_{int}}{2} - w_c\right)\right] \tag{1.4}$$

As I will describe more thoroughly in chapter 2, the U-shaped buried channel is etched in Silicon and it is sealed by two lids of masses $m_{lid,top}$ and $m_{lid,bottom}$. The coefficient $\frac{m_{eff}}{m_{cantilever}} = 0.25$ in equation (1.2) is mode-independent and comes from taking into account the normalized oscillation amplitude (so-called modal shape) $U_n(x)$ of a resonating cantilever along its length x, and modeling the total vibrating mass of the cantilever $m_{cantilever}$ as a point mass m_{eff} at the tip of mass-less beam.

m_{eff} is computed by integrating the kinetic energy of the cantilever along its length L_{res} and equating this term to the kinetic energy of a mass-free oscillator with a point mass m_{eff} at its tip [25]. The normalized modal shape is:

$$U_n(x) = A_n \left(cos\frac{\lambda_n}{L_{res}}x - cosh\frac{\lambda_n}{L_{res}}x \right) + B_n \left(sin\frac{\lambda_n}{L_{res}}x - sinh\frac{\lambda_n}{L_{res}}x \right) \tag{1.5}$$

A_n and B_n are the mode coefficients such that $A_n/B_n = (cos\lambda_n - cosh\lambda_n)/(sin\lambda_n - sinh\lambda_n)$ [26, 24]. Considering the added mass of a nanoparticle going through the resonator's buried channel to be negligible with respect to the total mass of the cantilever, it is possible to use Rayleigh-Ritz theorem to compute the balance between the kinetic and potential energies over a full cycle of oscillation when a particle changes the mass of the system and extract the variation in resonance frequency consequent to this event as a function of position along the cantilever's length [24].

$$\frac{\delta\omega_r}{\omega_r}(x) \simeq \frac{1}{\sqrt{1 + \frac{\delta m}{m_{eff}} U_n^2(x)}} \tag{1.6}$$

Combining equations (1.5) and (1.6) and solving for the first mode $n = 1$ one can track the relative change in the resonator's resonance frequency $\frac{\delta\omega_r}{\omega_r}$ as a nanoparticle of buoyant mass $m_b = \delta m$ flows forwards and backwards through the buried channel (Figure 1.1, right). Since for $n = 1$, $U_n(x)$ is a monotonically increasing function from the beam fixed end (1) to its tip (3), if the m_b is positive (i.e. the density of the nanoparticle is larger than the density of the buffer fluid it is suspended in), the resonance frequency decreases as the bead flows towards the U-turn of the cantilever. At this point, $U_n(L_c)$ is maximum and the resonance frequency is minimum; it increases again when the nanoparticle travels in the second half of the buried channel from (3) to (4) to the right bypass channel. The cantilever's resonance frequency goes back to its baseline value, ω_r. For a nanoparticle going through the U-shaped buried channel when the cantilever oscillates at higher modes $n > 1$, the resonance frequency shift shape $\frac{\delta\omega_r}{\omega_r}(x)$ has a different shape with a number of local minima and maxima that depends on the number of nodes and antinodes of the modal shape. Figure 1.2 shows the normalized modal shape $U_n(x/L_{res})$ for the first three modes n = 1,2,3 and the resonance frequency shift shape $\frac{\delta\omega_r}{\omega_r}(x/L_{res})$ that comes from a nanoparticle flowing through the U-shaped buried channel during oscillation of the cantilever at either one of these modes.

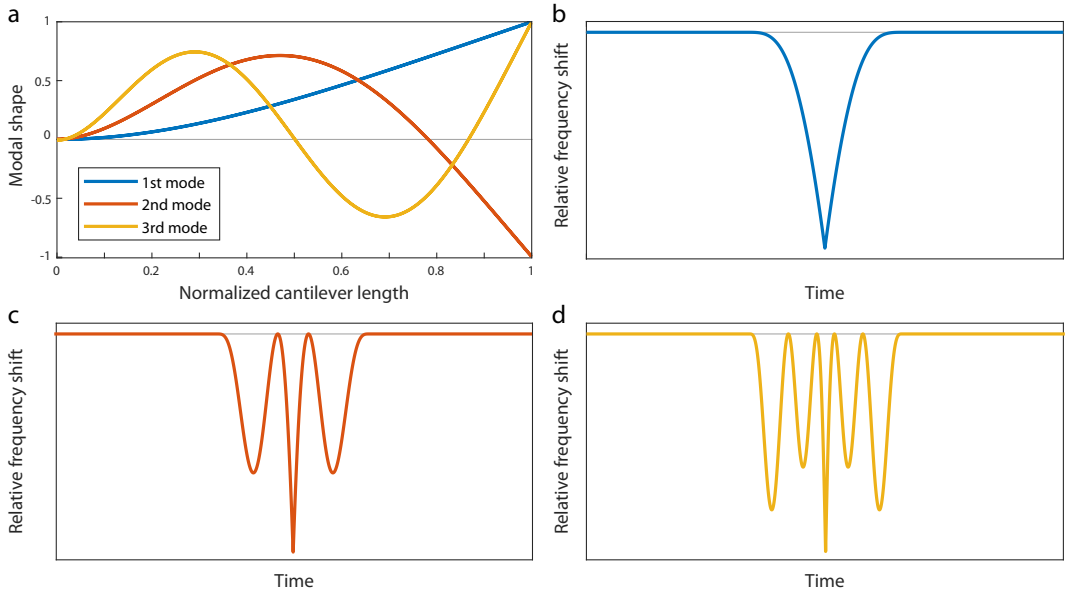

Figure 1.2. (a) First, second and third mode normalized oscillation amplitudes vs the normalized cantilever length. (b,c,d) Relative resonance frequency shift consequent to a nanoparticle flowing through the U-shaped buried channel embedded in the SNR when the cantilever oscillates at its first (b), second (c) or third (d) mode.

For a nanoparticle at the tip of the buried channel in a resonator oscillating at its first mode, equation (1.6) can be simplified and approximated to:

$$\frac{\delta\omega_r}{\omega_r}(x = L_c) \simeq -\frac{1}{2}\frac{\delta m}{m_{eff}}U_n^2(x = L_c) \simeq -\frac{1}{2}\frac{\delta m}{m_{eff}} \tag{1.7}$$

The result in equation (1.7) is mode-independent and oscillation amplitude independent due to the normalization of the mode shape U_n, and it allows to directly correlate an easily measurable quantity, the first mode height peak, to the buoyant mass of the analyzed particle. In fact, by measuring the resonance frequency shift peak height $\delta\omega_r$ and knowing the cantilever's resonance frequency ω_r and effective mass m_{eff}, it is possible to have an estimate of the nanoparticle's buoyant mass $m_b = \delta m$ that has flown in the channel. Consequently, the SNR responsivity R_m measured in mHz/ag is defined as:

$$R_m := \frac{1}{2\pi}\frac{\delta\omega_r}{\delta m} \tag{1.8}$$

In practice, R_m is extracted for each SNR device by using monodisperse calibrated beads, and its value is used to measure the buoyant mass of unknown samples. Unfortunately, nanoparticles that are much smaller than the buried channel cross section do not always reach its tip L_c but will flow in a wider region between L_c and $L_c - w_c$ meaning that the buoyant mass detection at the tip of a cantilever oscillating at its first mode is always affected by some error [27]. To eliminate this position-dependent error, higher modes operation of SNRs have been studied and implemented: instead of measuring the resonance frequency shift height at the tip of the cantilever, it is possible to solve equation (1.6) at the known position x_{an} of one of the antinodes for $n = 2,3,..$ and calibrate SNR accordingly. Since particles run parallel to the cantilever's length at its antinodes, their mass estimation will not be affected by the position-dependent error. Moreover, the intrinsic mass sensitivity $\delta m \propto R_m^{-1}\sqrt{1/\omega_r Q_n}$ increases for higher vibration modes $n > 1$ mainly due to the increase in resonance frequency [28]. By setting the geometrical parameters of the cantilever and the embedded buried channel, and consequently varying the effective mass of SNR, it is possible to design architectures of SNR and SMR (the larger implementation with mass resolutions in the order of $\sim fg$, $10^{-15}g$) that target samples of different sizes: from viruses, to bacteria, to cells.
In the next section I will present some of the applications that can be exploited using different architectures of SNRs.

1.2 Family of SNR devices

By looking at equation (1.8), it is straightforward to notice that by measuring the resonance frequency shift δm due to the passage of a particle through the buried nanochannel, one directly has an information on its buoyant mass in SNRs that have been calibrated and for which R_m is known. It is possible to apply Archimedes principle in the design and operation of SNRs in such a way that size and density properties can be estimated after extraction of the buoyant mass information, and to fluidically connect several SNRs in parallel to enhance the measurement throughput. Moreover, the technology allows for a non-destructive analysis of samples and it performs efficiently with a large variety of fluids, which makes it suitable for measurements done on biological matter, such as viruses, bacteria, and cells. SMR devices, the larger scale version of SNRs, can in fact be

used to measure cellular mass growth over relatively large periods of time. Examples of SNR applications are given in the following sections of this chapter.

1.2.1 Buoyant mass measurement with SNR

The most simple SNR technology design requires a single resonator which embeds a U-shaped buried channel, and it allows for the measurement of a nanoparticle's buoyant mass. The buried channel, which is approximately as long as the cantilever it is embedded in ($L_c \simeq L_{res}$), extends out of the resonator and is connected fluidically to two so-called bypass channels, whose cross sections are much larger (figure 1.3). Four inlets (2 per bypass channel) make it possible to load the sample from and collect it into external vials or Eppendorf tubes. The vials can be pressurized using pressure regulators that are controlled by the user via a LabVIEW script (Figure B.1): the sample flow rate can be set quite easily, as well as the direction of flow. The flow rate of particles through the buried channel is given by its volume divided by the transit time; the former is computed from the geometrical properties of the device (table 1.1) and the latter is extracted using a MATLAB algorithm that computes the time difference between the moments where a particle enters the resonator and subsequently escapes from it. One bypass channel is dedicated to sample loading, while the second one is used for sample collection (figure 1.4). In the sample loading bypass, one inlet is connected to the fluid containing the sample to be tested, while the other is connected to a buffer solution: typically water for synthetic samples or PBS for biological matter. Buffer fluids are filtered through a $200nm$ membrane to reduce the risk of clogging of the buried channel. A high pressure (+ in the schematic in figure 1.4) is applied to both vials, creating the so-called pinched flow: a mix of the sample and the buffer solution will be forced to flow through the buried channel and into the resonator. The sample collection bypass is connected to two empty vials; one of them is pressurized to a high pressure state (+, figure 1.4), meaning that the fluid coming from the buried channel will be forced to flow towards the fourth inlet which is connected to a vial that is pressurized to a low pressure state (-, figure 1.4). Since the high-pressure and low-pressure regulators are independent from one another, it is possible to finely control the flow rate of particles traveling through the resonator. The diluted sample collected in the low-pressure vial can be used for further analyses, as it is not

damaged by the measuring process.

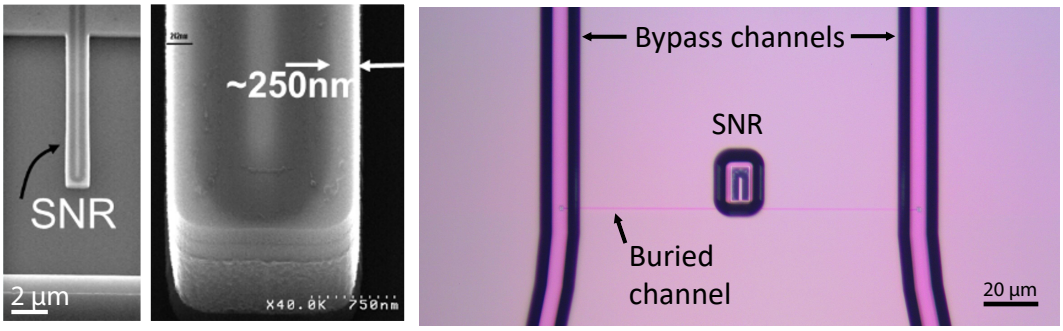

Figure 1.3. SEM images of the U-shaped buried channel embedded in an earlier architecture of SNR (left). Optical microscope image of a single-resonator SNR device (right) showing sample-load and sample-collect bypass channels and the buried channel extending out of the vacuum chamber that seals the cantilever.

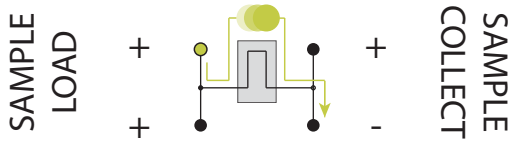

Figure 1.4. Schematics of a particle going through the fluidic channels of a single-resonator SNR device from the sample-load bypass (pinched flow pressures mode), through the buried channel, to the sample-collect bypass.

In the case of Suspended Nanochannel Resonators, the cross-sectional width and height of the buried channel are below $1\mu m$, and the cantilever effective masses are quite small compared to the larger version of the technology, SMR. These properties allow for the detection of particles with buoyant masses as low as a few tens of attograms. A summary of SNR types developed by the Manalis lab at MIT in partnership with CEA/Leti (Grenoble, France) and their properties is given in the table 1.1. From *SNR0* to *SNR3*, the effective mass of the resonator is increasingly lower, meaning that the relative resonance frequency will be increasingly higher and so will be the absolute mass sensitivity of the device [28]. To measure buoyant mass, it is necessary to perform first a calibration of the device in use which means measuring the average resonance frequency shift $\overline{\Delta f_r}$ produced at the cantilever's

$t_c = 700nm$
$w_{ext} = 1\mu m$
$w_{int} = 500nm$

Resonator type	f_r (MHz)	L_{res} (μm)	$R_{m,typ}$ (mHz/ag)	w_c (nm)	w_{res} (μm)
SNR0	1.5	32.5	5	1000	4.5
SNR1	2.5	25.0	15	700	3.9
SNR2	3.5	21.0	20	700	3.9
SNR3	4.5	17.5	30	700	3.9

Table 1.1. Summary of single-resonator SNR geometrical properties and resonance frequency. t_c and w_c are the buried channel depth and width, w_{int} and w_{ext} are the channel-to-channel and channel-to-sidewalls spacings, f_r is the resonance frequency, L_{res} and w_{res} are the resonator's length and width, $R_{m,typ}$ is a typical value of mass responsivity.

tip by a sample with known mass $m_{b,sample}$, and deducing the frequency-to-mass conversion parameter, i.e. mass responsivity measured in mHz/ag, as expressed by equation (1.9).

$$R_{m,calib} = \frac{\overline{\Delta f_r}}{m_{b,sample}} \tag{1.9}$$

The buoyant mass of an unknown sample is thus measured by dividing ITS average resonance frequency shift by the responsivity $R_{m,calib}$ measured in the calibration step.

Given the geometrical properties of SNRs and their designed mass resolutions, gold nanoparticles with diameters in the range of $10nm$ to $80nm$ are ideal for calibration as long as the measured samples have similar density: their buoyant masses are in the range of a few tens of attograms to a few femtograms. Particle size has to be carefully selected depending on the SNR type because of the inertial trapping phenomenon: nanoparticles get stuck at cantilever's tip instead of flowing out of it. Trapping occurs more frequently for SNR designs that have higher resonance frequencies or for SNR devices whose cantilevers are excited at modes larger than the first because centrifugal forces at the tip are quadratically proportional to f_r meaning that heavier particles have a higher chance of not having enough momentum to leave the nanochannel U-turn when they reach it. If many big particles get stuck at the resonator's tip, the nanochannel may get clogged; it is however fairly easy to unstuck particles from the channel end by inverting the flow direction and

it is possible to overcome the trapping problem in the first place by reducing the driving force and increasing the sample's flow rate.

1.2.2 Parallel array SNR design

Single-resonator SNRs are able to measure the buoyant mass of samples with a relatively wide range of concentrations but they are limited in terms of throughput, i.e. the number of resonance frequency shift events per unit of time. In fact, the analysis on a low concentration sample can take as long as a couple hours if one considers a statistically significant number of events to be above 100. Increasing the flow rate of particles running through the fluidic channels of the device has a positive effect on the measurement throughput, but there is a limit of transit time through the buried channel above which the resonance frequency shift signal is distorted by the readout circuitry implemented at the Manalis lab [29], meaning that the resulting measured buoyant mass will be inaccurate. To overcome the throughput limitations of single-resonator SNRs, the parallel array SNR design (pSNR) has been developed. As the name suggests, a pSNR chip contains an array of 10 resonators whose buried channels are fluidically connected in parallel to the sample-load and sample-collect bypass channels (figure 1.5). When a pinched flow is established in the sample-load bypass channel (the upper one in the schematic) by pressurizing at the high state (+) both vials connected to the inlets, the sample is forced to flow into the 10 buried channels, go through the resonators, and then escape into the sample-collect bypass channel where there is a high pressure difference in between its two inlets (+ on one side, - on the other). If a sample with a given concentration is analyzed for a given time and flow rate with pSNR, there is a 10-fold increase in throughput with respect to the same analysis performed using a single-resonator SNR. In other words, the pSNR design allows for a 10-fold decrease in measurement time, which is crucial for low concentration samples. pSNR also provides redundancy of available SNR resonators when measuring a sample that has high chances of clogging the channels or getting trapped at their ends.

A summary of pSNR architectures developed by the Manalis lab at MIT in partnership with CEA/Leti (Grenoble, France) and their properties is given in table 1.2. In terms of performance, resonance frequency, and responsivity, one can say that the pSNR *A0/1* type resembles *SNR0/1* type single-resonator devices.

$t_c = 700nm$
$w_c = 1\mu m$
$w_{int} = 500nm$

A0 res#	1	2	3	4	5	6	7	8	9	10
L_{res} (μm)	33.75	33.50	33.25	33.00	32.75	32.50	32.25	32.00	31.75	31.50
w_{ext} (μm)					1					
w_{res} (μm)					4.5					
f_r (MHz)					1.5					
$R_{m,typ}$ (mHz/ag)					5					
A1 res#	1	2	3	4	5	6	7	8	9	10
L_{res} (μm)	26.80	26.60	26.40	26.20	26.00	25.80	25.60	25.40	25.20	25.00
w_{ext} (nm)					500					
w_{res} (μm)					3.5					
f_r (MHz)					2.5					
$R_{m,typ}$ (mHz/ag)					15					

Table 1.2. Summary of pSNR geometrical properties and resonance frequency. t_c and w_c are the suspended channel depth and width, w_{int} and w_{ext} are the channel-to-channel and channel-to-sidewalls spacings, f_r is the resonance frequency (the frequency spacing between one resonator and the next is in the order of a few tens of kHz), L_{res} and w_{res} are the resonator's length and width, $R_{m,typ}$ is a typical value of mass responsivity.

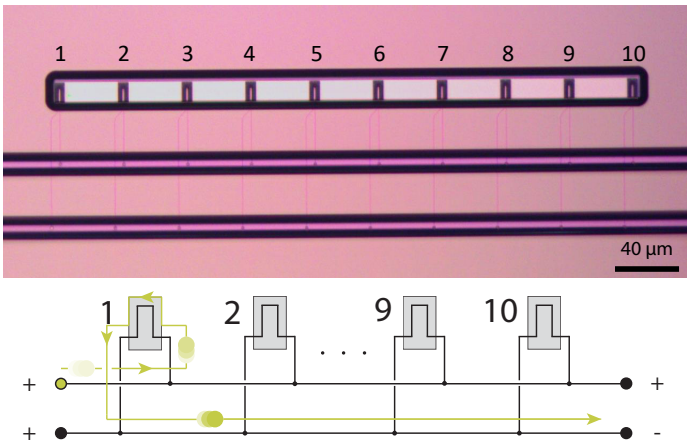

Figure 1.5. Optical microscope image of a parallel SNR array (top) and schematic of a particle going through the fluidic channels of a pSNR (bottom).

All cantilevers belonging to a pSNR array have the same geometrical properties, except for their length: there is a small change ($0.25\mu m$ for A0 type pSNR; $0.20\mu m$) in this quantity from one resonator to the next one that allows for an increment in resonance frequency of $\Delta f_{res} \approx 30kHz$ that makes it possible to sense the individual signals coming from different cantilevers at the same time.

1.2.3 Density SNR design

A sample of unknown density ρ_S and volume V_S is suspended in a buffer fluid with known density ρ_1 and it is flown through the sample-load bypass channel (Figure 1.6). When pinched flow is established, the sample goes through the first resonator (SNRa) and its buoyant mass $m_{B,1}$ is estimated through the measured average resonance frequency shift $\overline{\Delta f_a}$ and the resonator's responsivity R_{SNRa} computed in a previous calibration step.

$$m_{B,1} = \frac{V_S}{\rho_S - \rho_1} = \frac{\overline{\Delta f_a}}{R_{SNRa}} \tag{1.10}$$

A fluid of known density ρ_2 runs through the middle bypass channel (blue in figure 1.6) which crosses the buried channel of SNRa. A mixer has been fabricated by patterning holes at the interface between the two channels so that the sample enters SNRb being diluted of a known mixture of fluids 1 and 2. Ideally, the sample

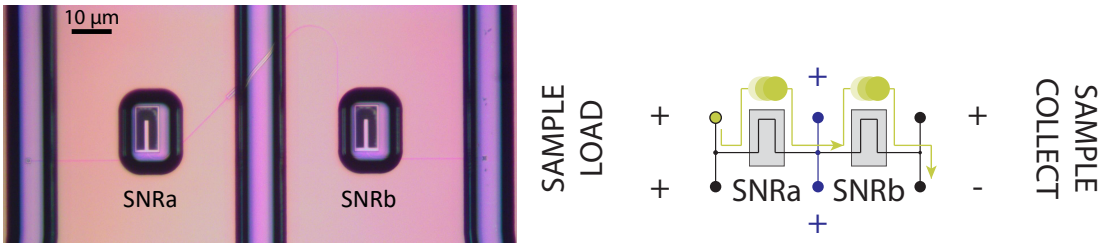

Figure 1.6. Optical microscope image of a density SNR design showing the mixer between the middle bypass channel and the buried channel of a D0 type (left). Schematics of a particle going through the fluidic channels of a density SNR design (right). The sample is injected from the sample-collect bypass, goes through SNRa, is mixed with a second buffer fluid in the middle (blue) bypass channel, goes through SNRb and exits into the sample-collect bypass channel.

$$t_c = 700nm$$
$$w_c = 1\mu m$$
$$W_{ext} = 1\mu m$$
$$w_{int} = 500nm$$
$$w_{res} = 4.5\mu m$$
$$f_r = 1.5MHz$$
$$R_{m,typ} = 5mHz/ag$$

D0/D1 resonator #	SNRa	SNRb
L_{res} (μm)	32.50	31.50

Table 1.3. Summary of density SNR design geometrical properties and resonance frequency. t_c and w_c are the suspended channel depth and width, w_{int} and w_{ext} are the channel-to-channel and channel-to-sidewalls spacings, f_r is the resonance frequency (the frequency spacing between SNRa and SNRb is in the order of a few hundreds of kHz), L_{res} and w_{res} are the resonator's length and width, $R_{m,typ}$ is a typical value of mass responsivity. D0 and D1 density SNR designs are equivalent in terms of geometrical properties of the employed resonators. They differ in the design of the mixing unit between the buried channel and the middle bypass channel.

that reaches the second resonator is mainly diluted into fluid 2, so the buoyant mass $m_{B,2}$ is measured as.

$$m_{B,2} = \frac{\overline{\Delta f_b}}{S_{SNRb}} \simeq \frac{V_S}{(\rho_S - \rho_2)} \tag{1.11}$$

The sample's volume can then be measured as

$$V_S = \frac{\rho_2 - \rho_1}{\frac{1}{m_{B,1}} - \frac{1}{m_{B,2}}} \tag{1.12}$$

and its density as

$$\rho_S = \rho_2 + \rho_2 \frac{1 - \frac{\rho_1}{\rho_2}}{1 - \frac{m_{B,1}}{m_{B,2}}} \tag{1.13}$$

With this device it is possible to extract the mass and density of any sample in solution without estimating its volume. Measurements of this kind can also be performed using a single-resonator SNR where two fluids are running in the two bypass channels. The sample runs through the resonator in fluid #1 and mixes with the second fluid in bypass #2. Then, pressure regulators are switched and the sample runs backwards in the resonator towards the waste. This technique requires a precise control of pressures but it can be automated (see figure B.1). Moreover, the mixing interface used in the density SNR design is not as efficient as a Y junction followed by a microfluidic mixer because the sample can easily escape from the buried channel towards the middle bypass channel, especially for particles whose size is much smaller than the mixer wells size. Nevertheless, the density SNR design allows to easily scale up the measurement throughput by fluidically connecting several of these devices in parallel.

The currently explored applications of the SNR technology were described in this chapter but they are not limited to these examples. Several other uses of these devices and their microscale counterpart, the SMR, were explored in the Manalis lab such as the non-invasive stiffness measurement of biological matter through the node deviation analysis at the antinode of a cantilever oscillating at its second flexural mode [3] and the mass accumulation rate measurement of cells through serially connected SMRs [2].
In the next chapters I will first give a brief overview of the design and fabrication steps performed at CEA/Leti (Grenoble) that led to the development of the piezoresistive gauges embedded in hollow nanocantilevers, and then I will describe the methods used to characterize parallel SNR arrays using the newly employed piezoresistive readout mechanism; finally, I will show the results of this analysis.

Chapter 2

Design and manufacturing of SNR devices embedding shallow piezoresistive gauges

The collaboration between the Manalis lab at MIT and the CEA/Leti research center in Grenoble led to the development of Suspended Nanochannel Resonator devices embedding in the same hollow cantilever structure a sub-micron wide fluidic channel (the smallest device that was manufactured has a buried channel with a cross section of $700 \times 700 nm^2$) and a shallow ($\sim 100 nm$ thick) piezoresistive gauge allowing for a purely electrical readout of resonance frequency. The aim of this chapter is first to give a hint of the optimization process that was used to design the geometrical properties of the single-resonator SNR, density SNR and parallel SNR arrays that I previously introduced, with focus on the latter technology; then, I will describe the manufacturing steps used to fabricate these devices. The design and fabrication steps that I will talk about in this chapter were performed by people working in the two institutes prior to the beginning of my training period.

All SNR-based designs are built using 2 SOI wafers properly etched and doped to perform the mechanical and electrical functions of the device, a Silicon wafer that supports a getter and seals from the bottom the vacuum chamber hosting the resonators, and a glass wafer that has the purpose of embedding the fluidic

channels and inlets and sealing from the top the vacuum chamber hosting the resonators (figure 2.1). For mass sensing optimization reasons that will be explored later in this chapter and to maximize the size dynamic range of the sensor, most of the device layer material of the two SOI wafers is etched away to delineate the buried channel. For this reason, only a narrow region (less than $\sim 100nm$) in the device layer of the top SOI wafer can be used to embed a piezoresistor made by implantation of Boron dopant in Silicon (figure 2.2): SILVACO simulations were carried out to study the doping profile at the cantilever's top face. Moreover, an optimization algorithm was developed by the researches involved in this project to extract the geometrical parameters of the resonator, the embedded channel and the piezoresistor allowing for a minimization of the absolute mass limit of detection. The design process is described in the next section.

2.1 The geometrical properties of SNR and the piezoresistive gauges are optimized for mass sensing at the attogram scale

The SNR technology enabling a fully electrical piezoresistive readout mechanism of the cantilever resonance frequency was designed by means of an optimization algorithm which adjusts the geometrical parameters of the resonators, fluidic nanochannel, and piezoresistive gauge to minimize the mass limit of detection of the device and reach attogram resolution. This algorithm is based on the open source *PiezoD* code developed by the Pruitt lab [30]; the cantilever geometry was modified to adopt the hollow configuration embedding the U-shaped buried channel. Moreover, the algorithm was adapted to optimize the parameters for mass detection rather than force sensing and the piezoresistor frequency noise terms were converted to an equivalent mass detection limit at a given measurement bandwidth. The optimization procedure was carried out for eight geometrical parameters (table 2.1): the cantilever length L_{res}, the piezoresistive gauge thickness t_{pzr} and length L_{pzr}, the buried channel width w_c and height t_c, the distance between the two branches of the U-shaped channel w_{int} and their distance to the sides of the cantilever w_{ext}, the thickness t_{lid} of the top and bottom Silicon lids sealing the buried channel. The boundary conditions of this optimization procedure were set by manufacturing

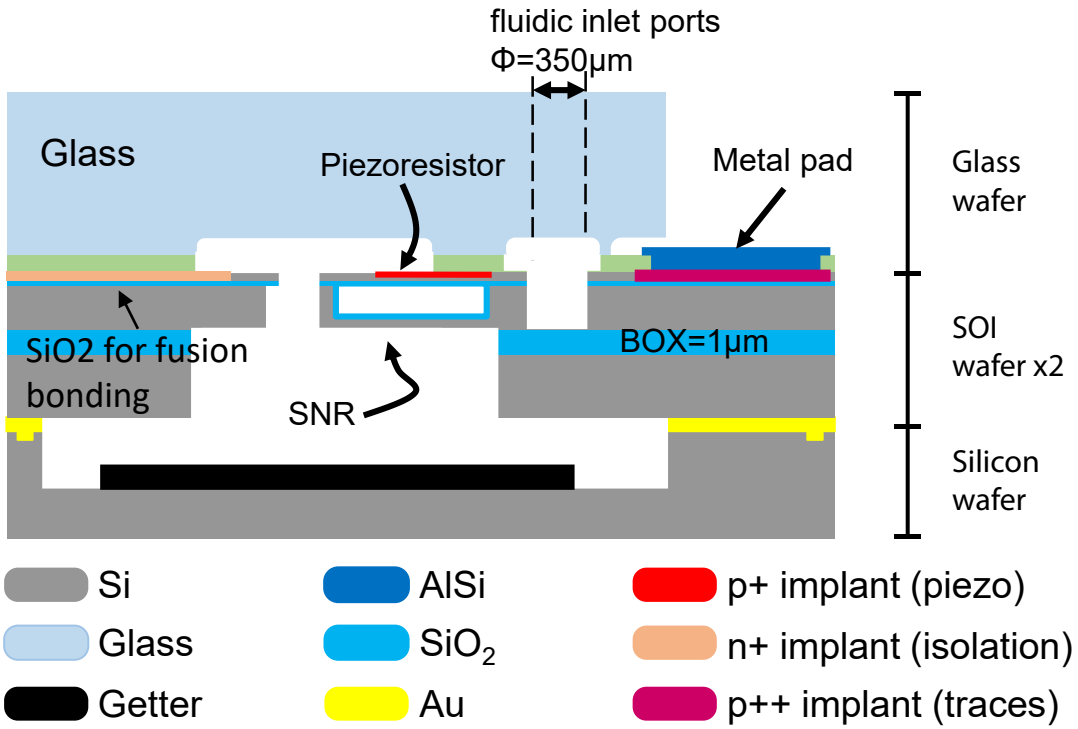

Figure 2.1. Cross sectional view of a SNR device showing the vacuum chamber were resonators are free to oscillate in. Two SOI wafers are top-to-top fusion bonded: the bottom SOI is used to define the mechanical components of SNR, the top SOI hosts its electrical components such as the piezoresistive element, the substrate isolation area and the conductive traces. The top glass wafer hosts the fluidic components (bypass channels and inlets); the bottom Silicon wafer hold the getter in place below the vacuum chamber.

technology constraints and design goals. For example, the minimum channel height $t_{c,min}$ was set to $700nm$ to allow for a wide range of nanoparticles with different sizes to be measured while minimizing the probability of clogging events, and the minimum thickness of the cantilever $t_{min} = t_{c,min} + 2t_{lid,min}$ was set to $1.1\mu m$ considering that the top lid is made entirely out of the device layer ($\sim 200nm$) of a SOI wafer; the minimum internal and external walls thickness were set to $500nm$ considering the limitations of the lithographic steps and to ensure enough bonding area of the two SOI wafers in the resonators. The lids and walls volumes should be minimized to ensure a low effective mass of the cantilever and thus minimize the limit of mass detection. Furthermore, the buried channel was placed on the

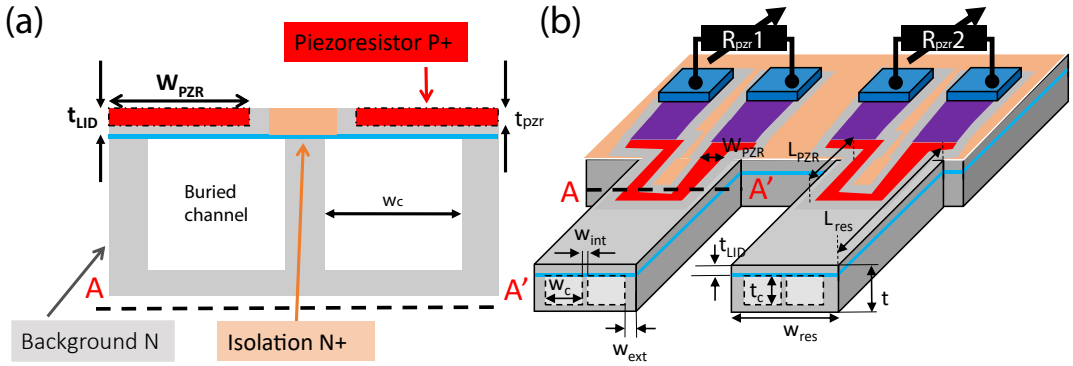

Figure 2.2. (a) Cross sectional view of a SNR cantilever showing the U-shaped buried channel, on top of which the U-shaped piezoresistor is patterned in the shallow upper lid region. (b) 3D schematics of a couple of SNR resonators showing their buried channels and U-shaped piezoresistors; the geometrical parameters symbols used here are reported in Appendix A. The electrical isolation regions and Aluminum metal pads are also shown. The section A-A' is shown in figure (a). The same color scheme for materials is used in figure 2.1.

neutral axis of the cantilever to maximize the quality factor by avoiding additional energy dissipation terms coming from net axial strain experienced by the fluid [31, 32]; the cantilever was assumed to be driven at the onset of non-linearity [29, 33]. The noise minimization procedure performed by the modified *PiezoD* algorithm is described in the next section.

Design parameters	Boundary conditions	Performances constraints
w_c	$700nm < w_c < 2\mu m$	f_r set by design
t_c	$700nm < t_c < 1\mu m$	Max temperature rise $< 4°C$
t_{lid}	$t_{lid} > 200nm$	Max signal attenuation $< 3dB$
w_{int}, w_{ext}	$w_{int}, w_{ext} > 500nm$	
t_{pzr}	$t_{pzr}/t_{lid} < 0.5$	
L_{pzr}	$10^{17} < N_p < 10^{20} at/cm^3$	
L_{res}	$V_b < 5V$	

Table 2.1. Optimization parameters that the algorithm derived based on the boundary conditions and performances constraints reported here. The symbols used here are listed in Appendix A and they are shown in the schematics of figure 2.2. Measurement bandwidth BW is set to $200Hz$ and SNR resonators quality factor Q is assumed to be 1,000. p-type dopant species is Boron.

2.1.1 Algorithm for minimization of mass limit of detection

The modified *PiezoD* algorithm that was developed to optimize the geometrical parameters of SNR computes the frequency noise components of the piezoresistive readout mechanism (Johnson, Hooge) and the thermomechanical noise limit for the given set of fixed parameters (table 2.1), converts it into an equivalent mass limit of detection, and minimizes the latter to reach attogram resolution. The resonator is assumed to have a high quality factor, $Q = 1{,}000$, and to be driven at the onset of its mechanical non-linearity, thus its RMS vibration amplitude is maximized and given by [34]:

$$< x_c >= 5.46 \, \frac{L_{res}}{\sqrt{2Q}} \tag{2.1}$$

For a given bandwidth ($BW = 200Hz$ in the algorithm), the frequency noise is given by the sum of three terms reported in equation (2.2) in the following order: thermomechanical noise, Hooge noise and Johnson noise [31].

$$< \delta\omega^2 >= \frac{k_B T \omega_r BW}{k < x_c^2 > Q} + \frac{1}{R_x^2} \frac{\alpha V_b^2 BW^2}{4 < x_c^2 > L_{pzr} w_{pzr} N_z} + \frac{1}{R_x^2} \frac{8 k_B T R_S L_{pzr} BW^3}{3 < x_c^2 > w_{pzr}} \tag{2.2}$$

k_B is the Boltzmann constant, T is the temperature of the cantilever, ω_r and k its resonance frequency and stiffness respectively, α is the Hooge's parameter, V_b the piezoresistance bias voltage, N_z is the total number of carriers per unit area, R_S is the sheet resistance. The geometrical parameters of the piezoresistor L_{pzr}, w_{pzr} are shown in figure 2.2. R_x, measured in V/m is the piezoresistance responsivity to displacement and is given by [35]:

$$R_x = V_b \gamma \beta^* \frac{3Et(L_{res} - 0.5L_{pzr})\pi_l}{8L_{res}^3} \tag{2.3}$$

γ is a geometry factor that accounts for a deterioration ($\gamma < 1$) of the piezoresistive effect due to parasitic resistance terms and it is defined as the ratio between the resistance of the strained region and the total piezoresistance, which accounts for unstrained regions, interconnects and contact pads. β^* is an efficiency factor accounting for less-than-ideal (i.e. not step-like) doping profiles defining the piezoresistance. E is Silicon's Young's modulus, π_l is the maximum longitudinal p-type piezoresistivity of Silicon along the *<110>* direction. The geometrical parameters of the cantilever and piezoresistor t, L_{res}, L_{pzr} are shown in figure 2.2.

From equation (1.7) it is possible to derive the equivalent mass limit of detection from the frequency noise of equation (2.2):

$$< \delta m^2 > = \frac{< \delta \omega^2 >}{R_m^2} = < \delta \omega^2 > \left(\frac{2 m_{eff}}{\omega_r} \right)^2 \tag{2.4}$$

where m_{eff} is the effective mass of the resonator computed from equation (1.2), and R_m is the mass responsivity of SNR in mHz/ag. Using this analytical formula, the algorithm can optimize the geometrical parameters of the cantilever and its embedded piezoresistive gauge by minimizing the equivalent limit of mass detection. For this first run of optimization, the doping profile defining the piezoresistive gauge was assumed to be constant. A few examples of results obtained using this code are given in table C.1. For example, a SNR device of type *SNR0*, whose designed resonance frequency is $f_r = 1.5MHz$, has an estimated mass resolutions below $1ag$ which is mainly limited by the thermomechanical noise of the cantilever (i.e. $\delta m \approx \delta m_{th}$) meaning that an optimized piezoresistive element does not deteriorate the performances of the SNR technology: the piezoresistive readout mechanism does not add a significant amount of noise into the system as will be demonstrated in chapter 3. For this design case, the doping concentration is $N_p = 4.2\ 10^{19} at/cm^3$, the ratio L_{pzr}/L_{res} is $\sim 33\%$ and the piezoresistance thickness is $100nm$, half the top lid thickness. Higher resonance frequency SNR devices (*SNR1*, *SNR2*, *SNR3*) have limits of mass detection in the same order of magnitude but higher frequency responsivity to mass variations R_m due to the shorter resonators and smaller effective mass.

2.1.2 Less than 1% variation in mass detection occurs around its optimal point

The previously described algorithm was modified to estimate how the mass limit of detection responds to variations of the optimized piezoresistor parameters. To do so, the equivalent mass noise was computed using equation (2.4) while three variables were swept in a range close to the optimized values reported in table C.1. This analysis was performed as a function of the normalized piezoresistive gauge thickness t_{pzr}/t, the normalized piezoresistive gauge length L_{pzr}/L_{res} and the p-dopant concentration; the contour plots in figures 2.3 and 2.4 report the results of

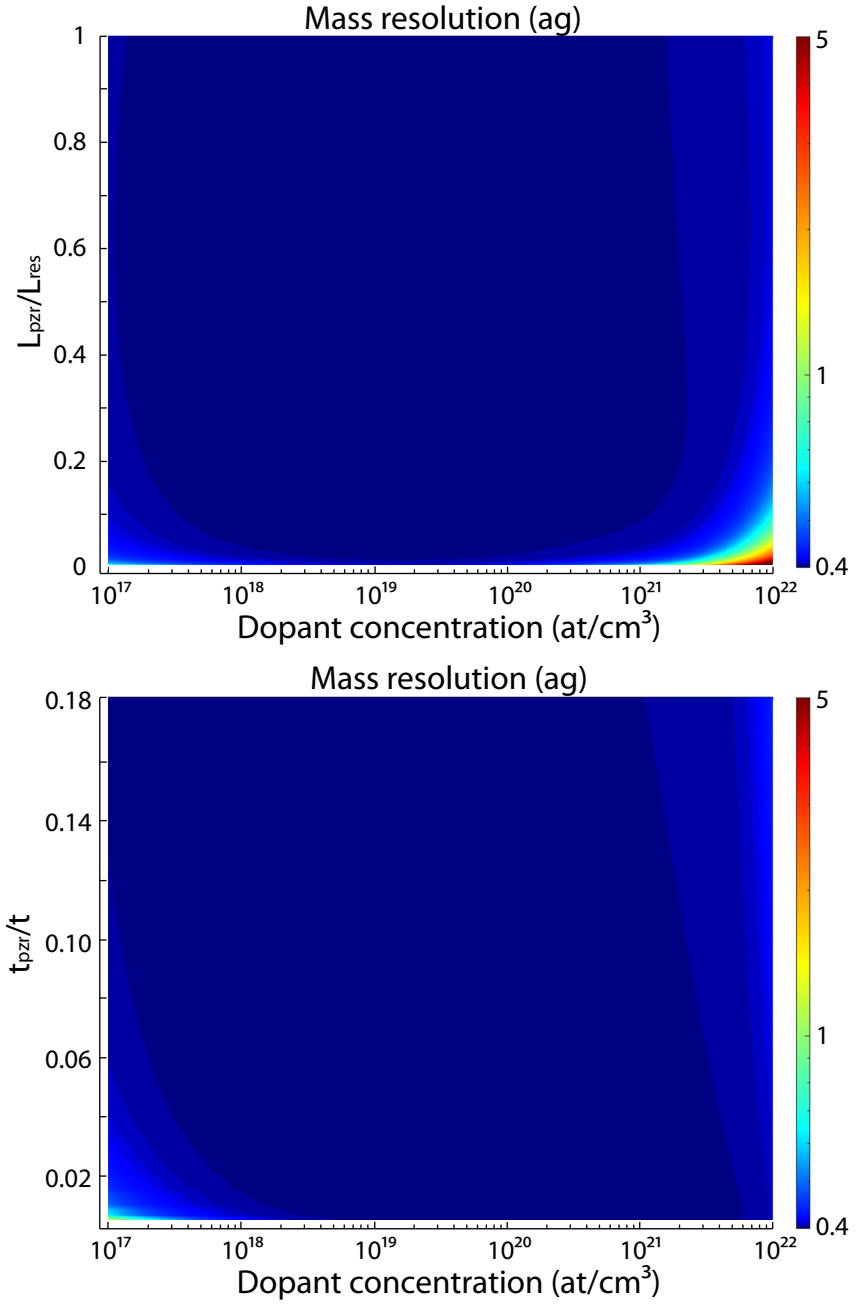

Figure 2.3. Mass resolution of one of the resonators in a pSNR array (SNR#10 in *A1*, table 1.2) plotted as a function of the normalized piezoresistive gauge length (top), the normalized piezoresistive gauge thickness (bottom) and the p-dopant concentration. The mass limit of detection is well below $1ag$ for a wide range of variability around the optimized values. In the top plot, the normalized piezoresistive gauge thickness is set to the optimized value $t_{pzr}/t = 0.1$; in the bottom plot the normalized piezoresistive gauge length is set to the optimized value $L_{pzr}/L_{res} = 0.4$.

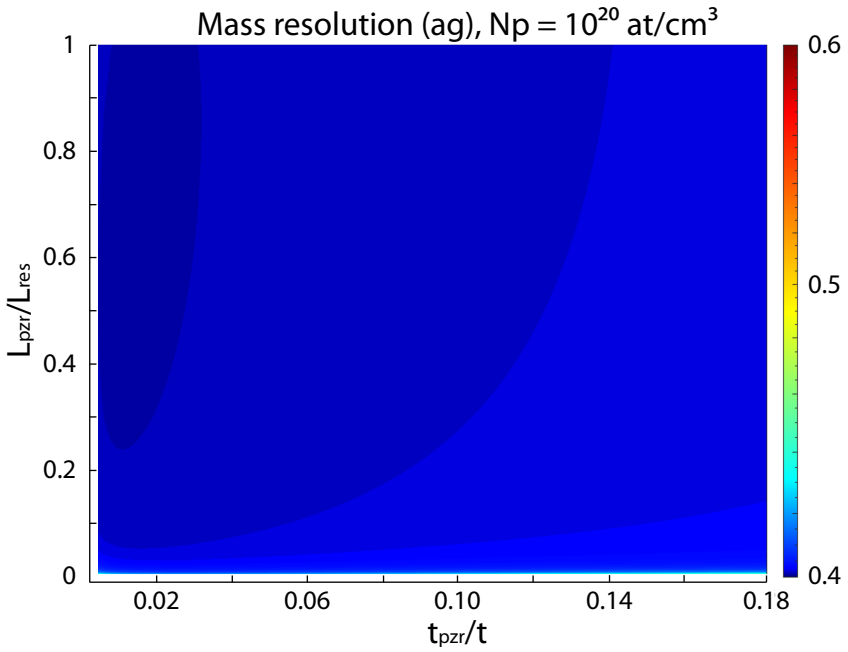

Figure 2.4. Mass resolution of one of the resonators in a pSNR array (SNR#10 in *A1*, table 1.2) plotted as a function of the normalized piezoresistive gauge length and the normalized piezoresistive gauge thickness; the p-dopant concentration is set to $N_p = 10^{20} at/cm^3$. The mass limit of detection is well below $1ag$ for a wide range of variability around the optimized values. Small variations of the mass resolution occur in this range: $0.4011ag$ to $0.4025ag$ from the the dark blue region of the plot to the light blue region.

this study for the highest resonance frequency resonator that has been designed for a pSNR array (SNR#10, *A1*).

The results of the optimization algorithm match with the parametric sweep study, and the latter shows that within a dopant concentration range of $10^{19} - 10^{20} at/cm^3$ little to no variation occurs in terms of limit of mass detection as long as $L_{pzr}/L_{res} > 0.05$: the relative change in mass resolution is $< 1\%$. Errors and variations in the technological process relative to the piezoresistive gauge fabrication shouldn't affect the performances of the device as long as the dopant is confined within a narrow region on the top of the cantilever and the fluidic channels are well isolated from it.

2.1.3 Optimization of parameters with doping profile simulation

The last steps in the design procedure were the optimization of the doping process used to embed the piezoresistive U-shaped gauge in the SNR resonators and the simulation of the doping profile by means of the SILVACO [36] software which is then used in the previously described algorithm to obtain once again the optimized geometrical parameters (table C.2). Targeting a Boron p-dopant concentration in the range of $10^{19} - 10^{20} at/cm^3$ and a junction depth at half the thickness of the top Silicon lid $\sim 100nm$ to ensure electrical insulation from the fluid underneath, doping profiles were simulated with ion implantation energies of $3, 4, 5keV$ and doses in the range $5\ 10^{14} - 3\ 10^{15} at/cm^2$; mass limit of detection was then computed using the optimization script embedding the results obtained from the simulations (figure 2.5). Once again, less than 1% variation in mass resolution is reported for the studied range. As a result, there is no limitation on the p-type ion implantation parameters so $5keV$ of energy and a dose of $7\ 10^{14} at/cm^2$ were chosen to ensure a robust doping process.
Finally, for the pSNR devices the piezoresistive element was set to be the same throughout the ten resonators in the array by fixing its geometrical parameters so that it would be easier from an electrical point of view to design readout amplification stages that are optimized for all cantilevers. This choice comes with the drawback of having non-optimized piezoresistive gauge parameters throughout the array and as a result the limit of mass detection changes as a function of the cantilever index (figure 2.6). There is a $\sim 16\%$ variation in mass resolution from the first to the last SNR resonator in the pSNR array but overall the estimated detection limit is still considerably good as it is $< 1ag$ for both *A0* and *A1* technologies.

A summary of the design process is given in figure 2.7. First the modified *PiezoD* algorithm is used to optimize the geometrical parameters of the SNR resonator, its buried nanochannel and the embedded piezoresistor. Then the piezoresistive gauge parameters are swept in the neighborhood of the optimized values to study the resulting variation of the mass resolution: the results show little to no dependence on the normalized length and thickness of the piezoresistor in the doping concentration range of $10^{19} - 10^{20} at/cm^3$. Finally, SILVACO simulations are performed

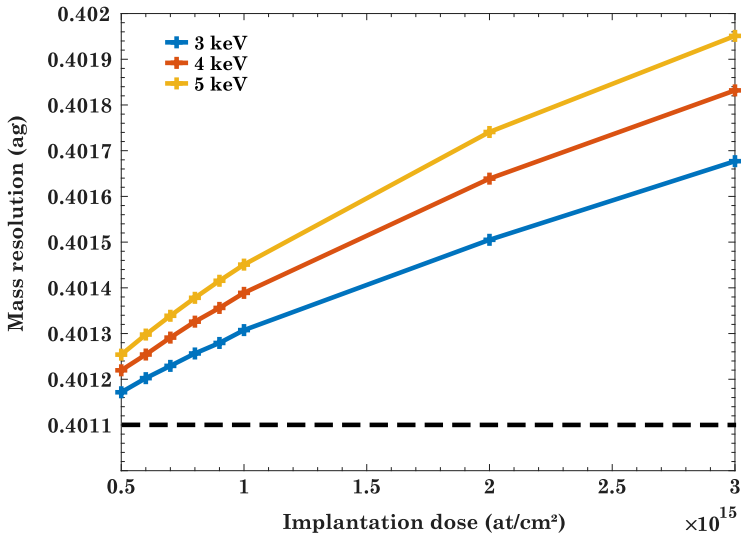

Figure 2.5. Mass limit of detection of a resonator in the pSNR array (SNR#10, in *A1*) vs p-dopant ion implantation dose and energy. Results of a SILVACO simulation that takes into account the presence of a $10nm$-thick screen oxide layer used during the implantation steps. The dashed line represents the thermomechanical limit for this device.

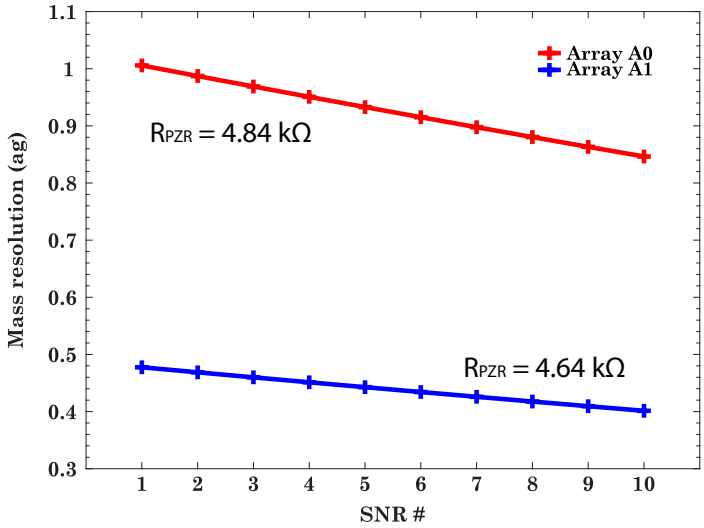

Figure 2.6. Variation of estimated limit of mass detection throughout the resonators in pSNR arrays of type *A0* and *A1* due to the design choice of fixing the piezoresistance value R_{pzr} of the gauge in all cantilevers of the array.

to optimize the ion implantation process and to determine the doping profile of the piezoresistive gauge. The results of the parametric sweep and the SILVACO simulations are used to perform a second run of the optimization algorithm and obtain the final design parameters.

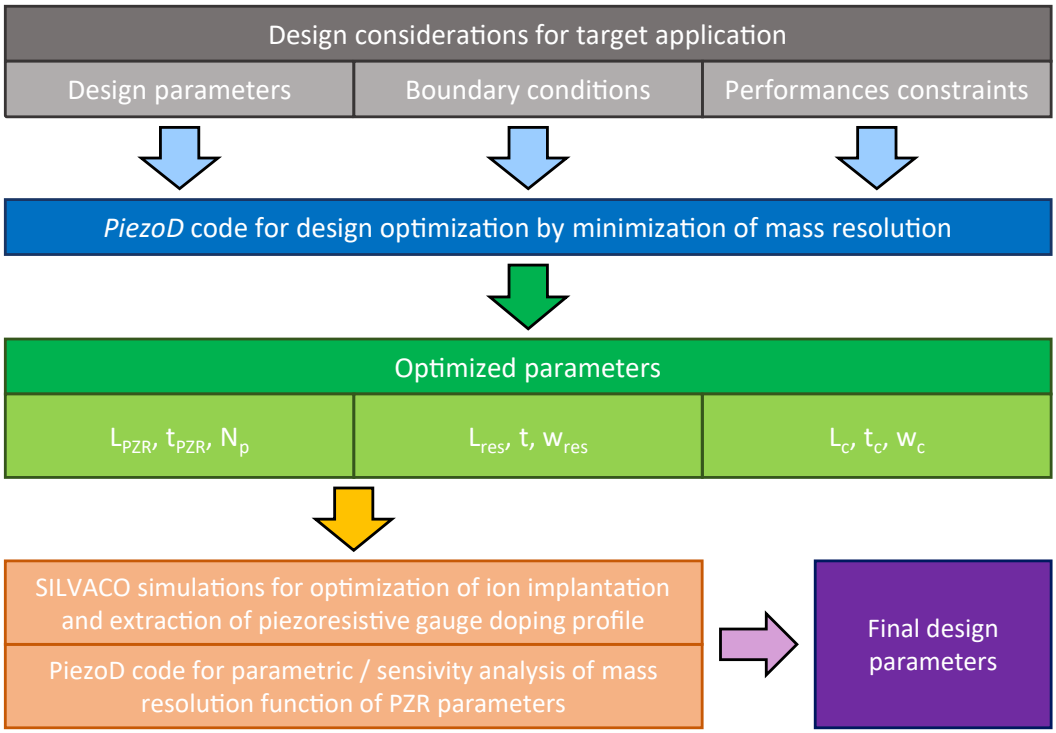

Figure 2.7. Summary of optimization steps used to design the geometrical parameters of the SNR resonator, the buried channel and the piezoresistive gauge.

2.2 Manufacturing steps of SNR devices

The following manufacturing steps have been used to fabricate the different types and designs of SNR devices such as the single-resonator SNR, the parallel SNR array and the density SNR design with geometries obtained from the previously described optimization scheme and reported in tables 1.1, 1.2, 1.3. As discussed in the introduction of this chapter, two SOI wafers are employed to manufacture the mechanical and electrical components of the devices and they are sandwiched between a top glass wafer and a bottom Silicon wafer that embed the fluidic channels and seal the resonators in a vacuum chamber. The color schemes used in the following cross section schematics follow the same pattern reported in figure 2.1. The ion implantation and annealing simulations results that I will report in this section were performed using the SILVACO software.

2.2.1 Bottom SOI wafer: buried channels

The bottom SOI wafer hosts the nanoscale cavities that will be used as buried channels inside the SNR resonators. From bottom to top it is made of a $725\mu m$ Silicon bulk, a $1\mu m$ SiO_2 Buried OXide (BOX) and a P-type $400nm$ thick top Silicon device layer.

1) Bottom SOI wafer preparation and N-type background doping of the Silicon device layer

The top Silicon device layer is full-sheet implanted with N-type Phosphorous dopant with a dose $10^{13} at/cm^2$ and an energy $140keV$; then, an annealing step is performed at $950°C$ for 30 minutes in N_2 for dopants activation.
A front-side epitaxy of $520nm$ thick n-doped (Phosphorous concentration of 4 10^{17} at/cm^3) Silicon is performed at $950°C$ (figure 2.8): the total n-doped Silicon device layer is now $920nm$. The wafer front side is protected by a $1.5\mu m$ thick PECVD SiO_2 layer while the backside is laser marked for future identification. The PECVD SiO_2 layer is removed with diluted HF and substituted by a growth of $7nm$ thick thermal oxide used as a protective layer.

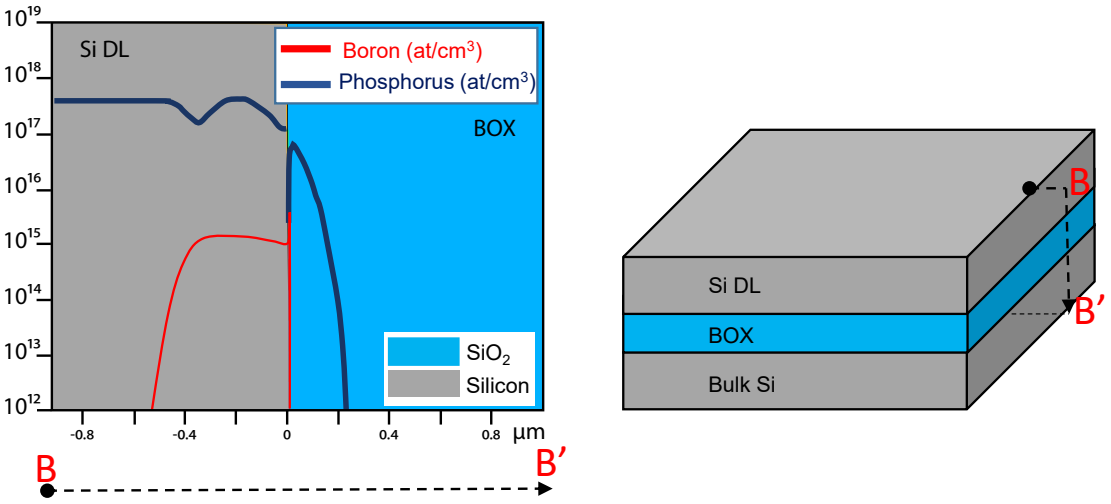

Figure 2.8. Doping profile of the n-type Silicon device layer of the bottom SOI after epitaxial growth of the $520nm$ Silicon layer. The profile is almost flat with Phosphorous dopant concentration in the range $2 - 4\ 10^{17} at/cm^3$.

2) Buried channel patterning on the device layer of the bottom SOI wafer

$120nm$ deep alignment marks are etched on the top Silicon layer of the bottom SOI with photolithography and Reactive Ion Etching (RIE) steps. The buried channels are then patterned on the top Silicon layer by means of DUV lithography and anisotropic RIE: $700nm$ deep trenches are patterned for all types of SNR technologies thus defining the thickness of the embedded fluidic nanochannels, t_c. The width of the channels are set with the photoresist mask and it is either $700nm$ or $1.1\mu m$ according to the device type. Figure 2.9 shows a schematic of the bottom SOI cross section up to this step of the manufacturing process.
The $7nm$ thick SiO_2 layer is then removed through chemical etching of 0.1% HF and it is substituted with a growth of $10nm$ thermal oxide that will be used as a protective layer for the next implantation steps and as a fusion bonding layer with the top SOI wafer. This oxide layer also covers the inner side of the buried channel.

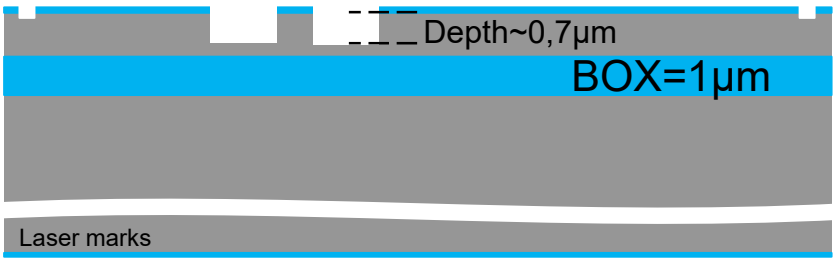

Figure 2.9. Schematic of the bottom SOI wafer after epitaxial growth of n-doped Silicon $520nm$, growth of the $7nm$ thick top thermal oxide (step 1), and etching of the $700nm$ deep buried channel (halfway through step 2).

2.2.2 Top SOI wafer: piezoresistor, electrical path and insulation

The top SOI wafer hosts the electrical components of the SNR devices: the shallow piezoresistors embedded in the resonators, the conductive paths from the gauge to the metallic pads, and the implantation of n dopants that ensure the electrical insultation of the previous elements. Moreover, the top Silicon layer will seal the buried channel patterned in the bottom SOI. From bottom to top the wafer is made of a $725\mu m$ Silicon bulk, a $2\mu m$ SiO_2 (BOX) and a P-type $220nm$ thick top Silicon device layer.

3) Top SOI wafer preparation and bonding with bottom SOI wafer

A $10nm$ thick thermal oxide is grown at $800°C$ on the surface of the Silicon device layer of the top SOI wafer. The two wafers are then aligned top-to-top and fusion bonded in vacuum at $10^{-2}mbar$; a high-temperature annealing is performed at $1100°C$ in a steam atmosphere to increase the bond strength between the wafers. The backside Silicon bulk of the top SOI wafer is then removed by successive steps of coarse and fine grinding to leave a $25\mu m$ thick Silicon handle, followed by a $TMAH$ etching that removes it completely. The BOX layer is also removed by means of a buffered oxide etchant solution. The result of these manufacturing steps are shown in figure 2.10: of the top SOI wafer, only the $200nm$ thick Silicon device layer is left.

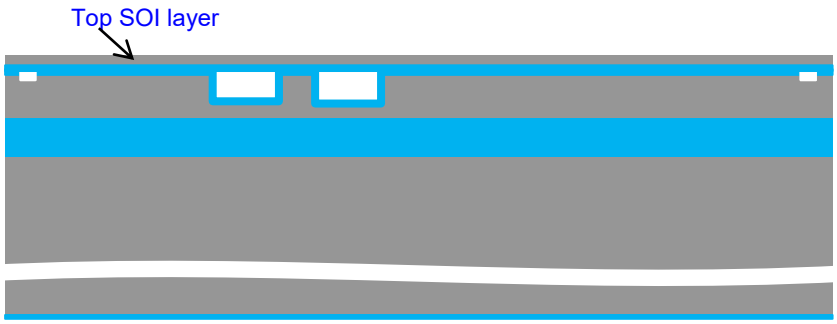

Figure 2.10. Cross section of top and bottom SOI wafers after thermal oxide is grown on both Silicon device layers (step 2 and 3), front-side fusion bonding of the wafers and removal of Silicon bulk and BOX layer of the top SOI wafer (step 3).

4) Implantation steps for piezoresistor, conductive paths and insulation

A pre-implantation $10nm$ thermal screen oxide is grown on the surface of the top Silicon layer at $800°C$ in a O_2 atmosphere. The n-type isolation background of the top Silicon layer is realized via the full-sheet implantation of Phosphorous ions at $70keV$ with a dose of $10^{13}at/cm^2$ (figure 2.11).
Photolithography and Boron implantation steps are carried out to define the P++ low-resistivity conductive traces that will connect the piezoresistive elements to the metal pads. The implantation is performed at $30keV$ with a dose of 5 $10^{15}at/cm^2$ (figure 2.12). Similar steps are carried out to define the N+ isolation traces in proximity of the conductive traces: a p-n junction will ensure the isolation between neighboring piezoresistive elements in a pSNR array. Phosphorous is implanted at $70keV$ with a dose of $10^{15}at/cm^2$ (figure 2.13). The wafer is then annealed at $1050°C$ for 30 minutes in a N_2 environment to obtain flat doping profiles.
The piezoresistive gauge elements are obtained by Boron implantation at $5keV$ with a dose of 7 $10^{14}at/cm^2$ followed by a spike annealing at $1050°C$ in N_2 atmosphere: the dopant is thus activated while limiting diffusion so that the piezoresistor is confined in a shallow region of the top SOI wafer. The junction depth for the piezoresistive gauge is $x_j \sim 110nm$ (figure 2.14).

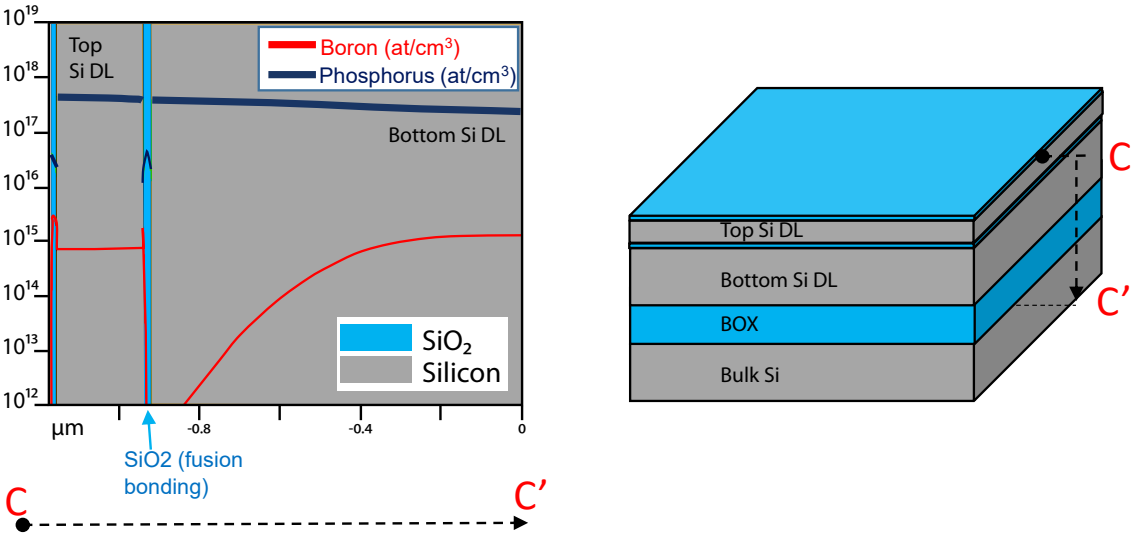

Figure 2.11. Simulation of the doping profile of the Silicon device layers of the top and bottom SOI wafers (separated by a $20nm$ thick thermal oxide for fusion bonding) after full-sheet implantation of Phosphorous in the top Silicon layer and annealing step. The n-dopant profile is quasi-flat throughout the Silicon thickness of both SOI wafers, at a concentration of $2.5 - 4.5\ 10^{17} at/cm^3$. A schematics of the SOI wafers layers involved in this process is shown on the left.

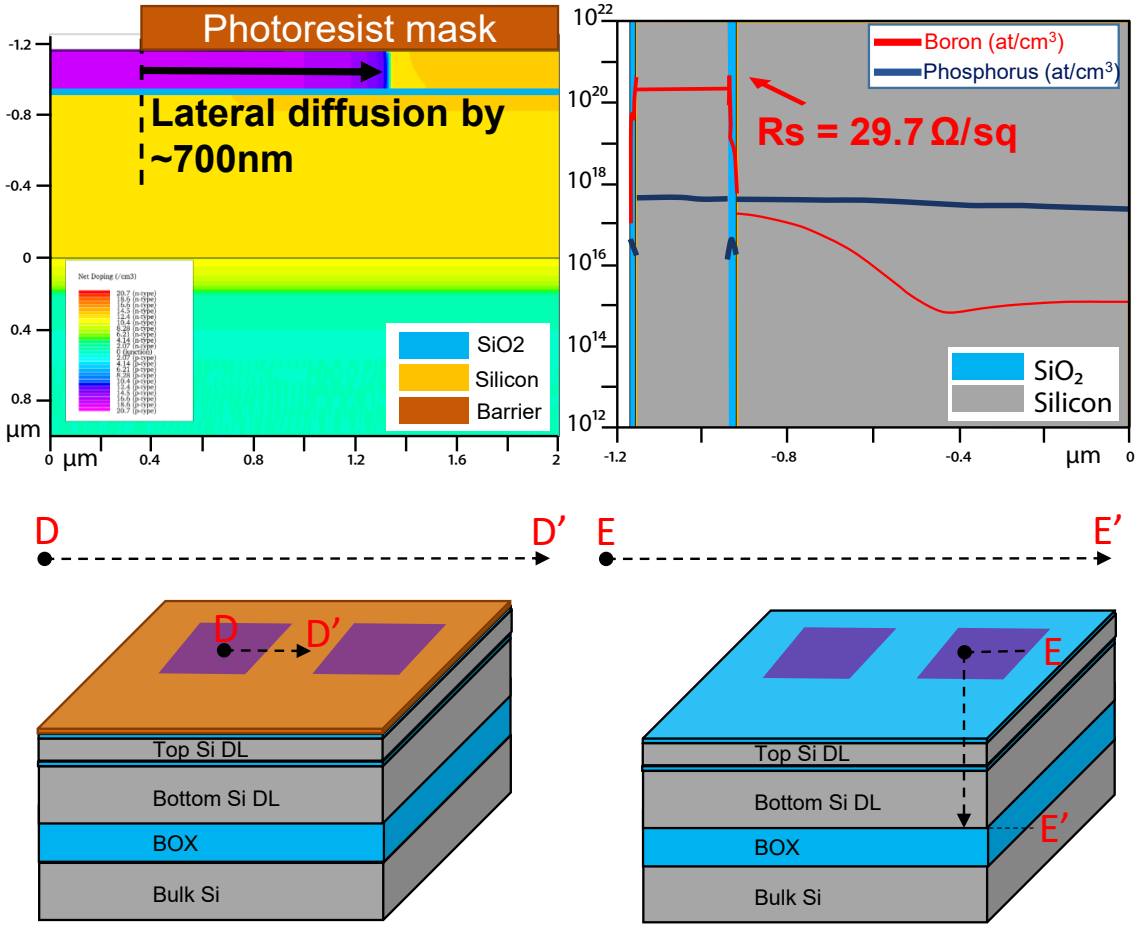

Figure 2.12. (left) Simulation of the 2D doping profile after Boron implantation in the top Silicon device layer to pattern P++ conductive traces. The simulation shows the $\sim 700nm$ wide lateral diffusion of p-dopant after annealing. The $20nm$ thick oxide bonding interface limits the vertical diffusion of the dopant. The lateral diffusion sets the minimum gap between the p-type conductive path and the n-type isolation traces. The color scale on the plot represents net doping levels in at/cm^3: red to green colors are for n-type dopings from high to low levels, green to purple color are for p-type dopings. Green is neutral (SiO_2 BOX layer in the plot). (right) Simulation of the doping profile of the Silicon device layers of the top and bottom SOI wafers (separated by a $20nm$ thick thermal oxide for fusion bonding) after implantation of Boron in the top Silicon layer and annealing step. The P++ conductive trace has a concentration of $\sim$ 2 $10^{20} at/cm^3$ leading to a sheet resistance of $29.7\Omega/\square$. Schematics of the SOI wafers layers involved in these processes are shown on the bottom.

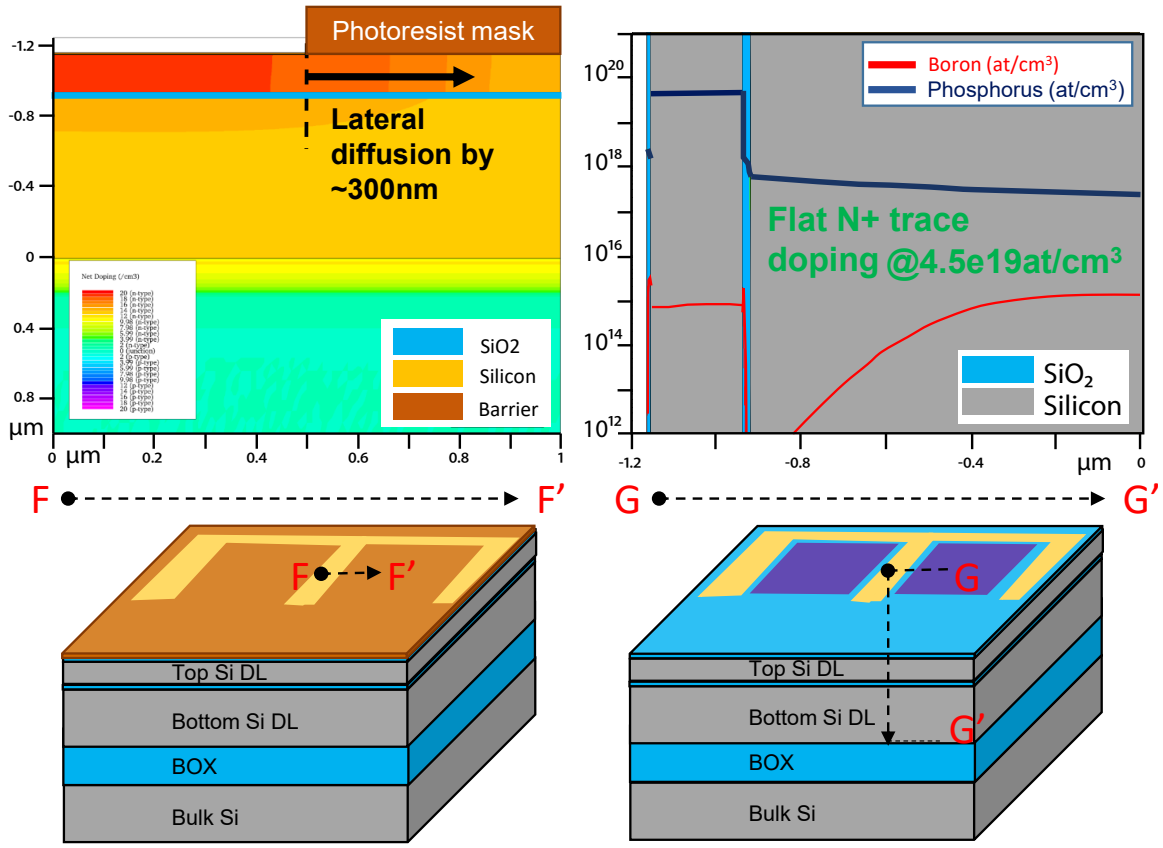

Figure 2.13. (left) Simulation of the 2D doping profile after Phosphorous implantation in the top Silicon device layer to pattern N+ isolation traces. The simulation shows the $\sim 300nm$ wide lateral diffusion of n-dopant after annealing. The $20nm$ thick oxide bonding interface limits the vertical diffusion of the dopant. The lateral diffusion sets the minimum gap between the p-type conductive path and the n-type isolation traces together with the previous constraint of figure 2.12. The color scale is the same used in figure 2.12. (right) Simulation of the doping profile of the Silicon device layers of the top and bottom SOI wafers (separated by a $20nm$ thick thermal oxide for fusion bonding) after implantation of Phosphorous in the top Silicon layer and annealing step. The N+ isolation trace has a concentration of $\sim 4.5\ 10^{19} at/cm^3$ and a flat profile. Schematics of the SOI wafers layers involved in these processes are shown on the bottom.

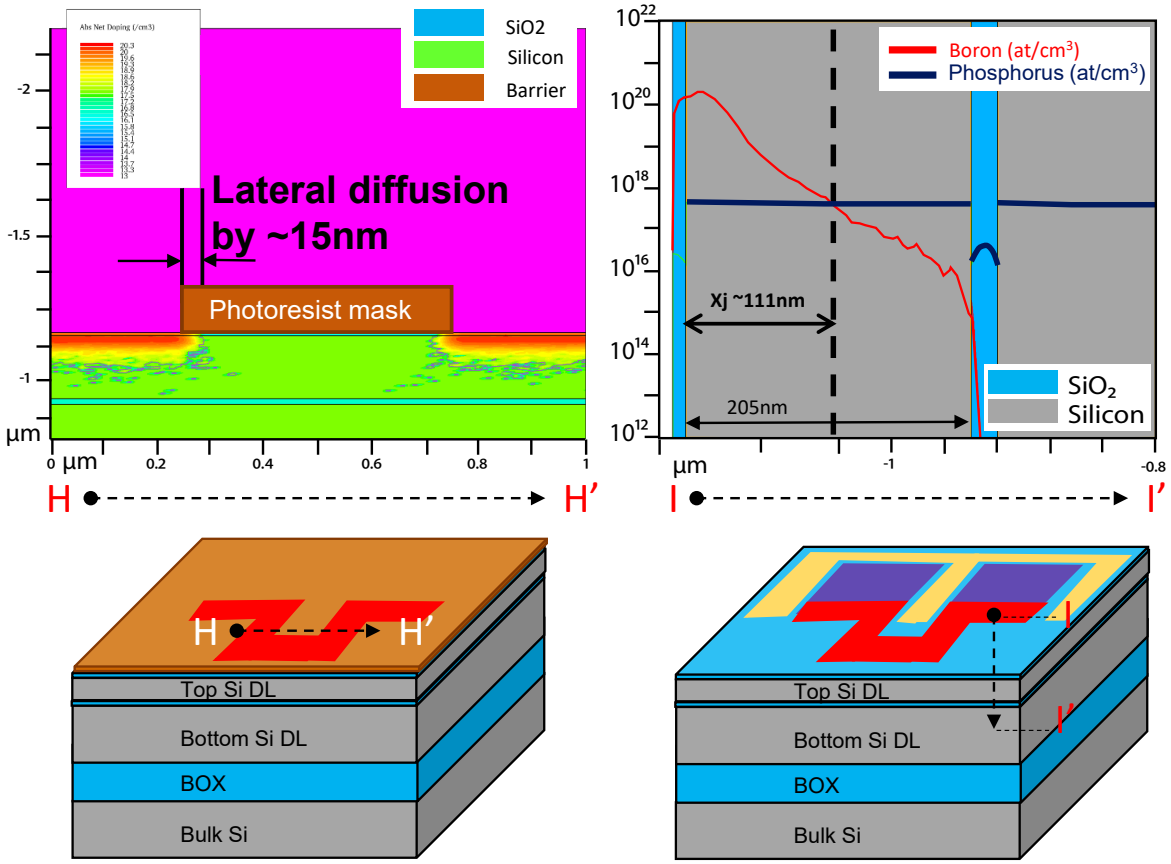

Figure 2.14. (left) Simulation of the 2D doping profile after Boron implantation in the top Silicon device layer to pattern the P++ piezoresistive element. The simulation shows the $\sim 15nm$ lateral and vertical diffusion of p-dopant after spike annealing. The color scale represents the net p-type doping from highest (red) to lowest (purple) concentrations. (right) Simulation of the doping profile of the Silicon device layers of the top and bottom SOI wafers (separated by a $20nm$ thick thermal oxide for fusion bonding) after implantation of Boron in the top Silicon layer and spike annealing step. The P++ piezoresistive element has a shallow peak concentration of $\sim 2\ 10^{20} at/cm^3$ and a junction depth $x_j \sim 110nm$ which is close to half the top Silicon layer thickness. Schematics of the SOI wafers layers involved in these processes are shown on the bottom.

5) Passivation of top Silicon layer and metal pads deposition

A $500nm$ thick PECVD TEOS oxide is deposited at $400°C$ on the top Silicon layer to passivate it with respect to contamination from the pyrex wafer that occurs during anodic bonding with the top SOI wafer. This layer is then chemical-mechanically polished to reduce the surface roughness and optimize the bonding with the glass wafer: $100nm$ of the layer is thus removed. The PECVD oxide is then selectively removed through RIE from the areas where the metal pads will be deposited.
A $650nm$ thick *AlSi* layer is sputtered on the front-side of the wafers stack and the metallic pads are patterned by chemical etching. Figure 2.15 shows the manufacturing steps performed up to this point.

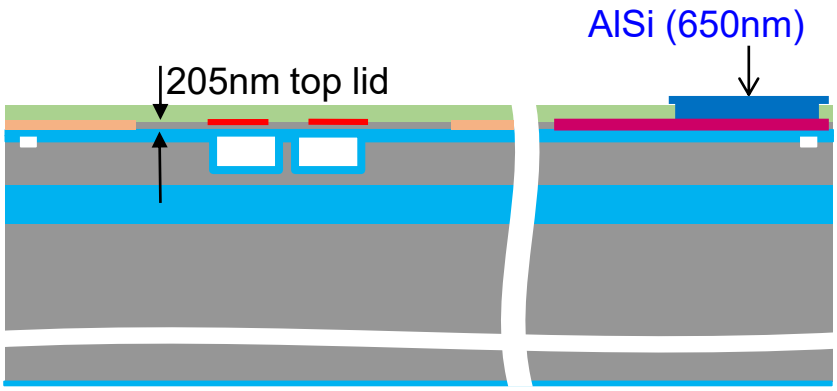

Figure 2.15. Cross section of top and bottom SOI wafers after the implantation steps that defined the piezoresistive gauge, the conductive paths and the isolation traces (step 4), the passivation of the top Silicon layer (shown in green) and the deposition of the metal pads (step 5).

6) SNR resonators top patterning

First, the PECVD TEOS oxide is patterned and removed from the SNR surface to avoid thermal expansion mismatch with the underlying Silicon layers. Then, steps of DUV lithography and RIE etching are performed to remove the side walls of the SNR resonator: a $10\mu m$ wide U-shaped trench is patterned around the cantilever through both device layers of the bottom and top SOI wafers. During the same manufacturing step, the $3\mu m$ wide access ports of the buried channels to

the bypass channels are etched through the Silicon device layers. Figure 2.16 shows the manufacturing steps performed up to this point.

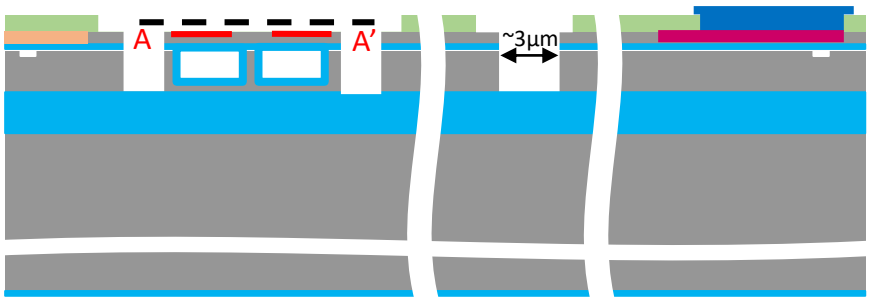

Figure 2.16. Cross section of top and bottom SOI wafers after the removal of the PECVD TEOS layer from the surface of the SNR resonator, and the etching of the U-shaped trench around the cantilever and the bypass-to-buried channels inlet port (step 6). The *A-A'* section is reported in figure 2.2

2.2.3 Glass wafer: fluidic bypass channels and inlet ports

The borosilicate float 33 glass wafer hosts the fluidic bypass channels that bring the fluid to the buried channel, the fluidic inlet ports that connect the bypass channels to the external vials, and a dome that will be aligned to be above the SNR resonators to allow flexural modes of vibration. The $500\mu m$ thick glass wafer will also seal from the top the vacuum chamber hosting the SNR resonators.

7) Glass wafer preparation

First a standard *SC1* + piranha cleaning procedure is performed. Then, a $1\mu m$ thick amorphous Silicon layer is deposited to protect both sides of the wafer. The backside is patterned through RIE removing the amorphous Silicon layer and etching down to $500nm$ into the glass wafer to define alignment marks. The front-side of the wafer is then patterned via chemical etching to define the $10\mu m$ thick and wide bypass channel, the dome above the SNR and the regions above the metal pads. The amorphous Silicon layer is removed through 1% *HF* washing followed by *TMAH* for $90°C$ for 30 seconds. Finally, the $350\mu m$ wide inlet ports are etched through the glass wafer full thickness via ultrasonic drilling (*Bullen Ultrasonic Inc.*). Figure 2.17 shows the manufacturing steps performed up to this point.

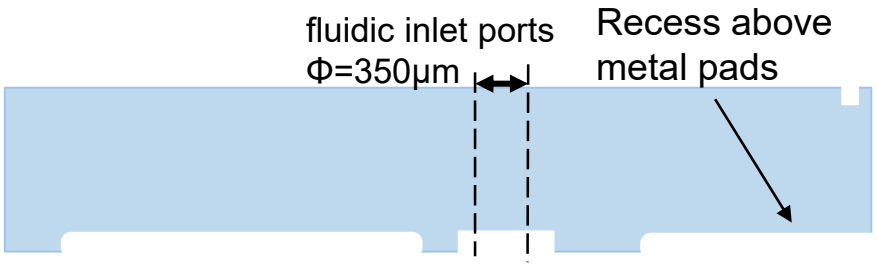

Figure 2.17. Cross section of the glass wafer after etching of the bypass channels, SNR domes, and recess above the metal pads; the fluidic inlet ports are etched through the wafer thickness via ultrasonic drilling (step7).

8) Anodic bonding of the glass wafer with the top Silicon layer of the SOI stack

The glass wafer is cleaned through *SC2* + 1% *HF* to remove particles residuals from the surface. The glass wafer and the SOI stack are aligned by means of the alignment marks and the are successively brought into contact while anodic bonding is performed at $400°C$ under primary vacuum for 15 minutes, with $3kN$ and $700V$ of applied force and voltage. The SOI stack backside is grinded to end up with a $200\mu m$ thick Silicon bulk and $5\mu m$ wide ditches are patterned through photolithography and RIE around the periphery of each SNR chip. The purpose of this trench is to retain the excess of molten gold that will be consequent to the eutectic bonding with the bottom Silicon wafer: this step is crucial to avoid contamination of the vacuum chamber and the getter. Finally, a step of photolithography and deep RIE is performed to drill a cavity in the bottom Silicon bulk layer below the SNR resonators. This step is followed by selective etching of the BOX layer in the same cavity region to release the SNR cantilevers from the backside. Figure 2.18 shows the manufacturing steps performed up to this point.

2.2.4 Silicon wafer: vacuum getter support

The Silicon wafer hosts the getter material that will improve the vacuum inside the chambers of SNR over extended period of times. The Silicon wafer used in this process is polished on both sides.

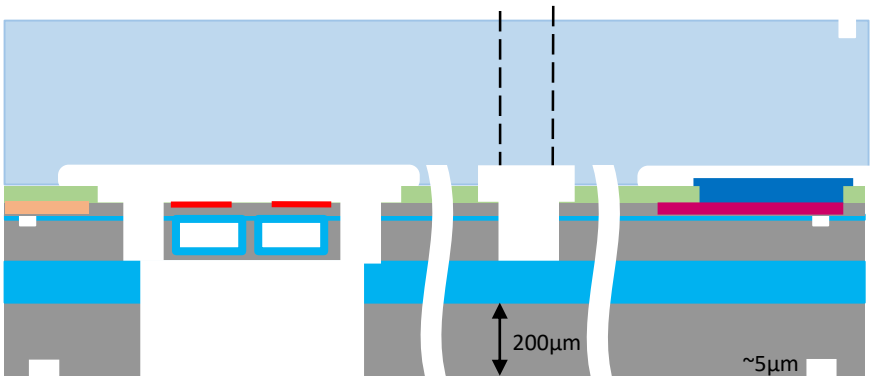

Figure 2.18. Cross section of the glass wafer and the SOI stack after anodic bonding, grinding of the SOI backside Silicon bulk, patterning of the $5\mu m$ wide ditches and release of the SNR resonators through drilling of a cavity in the underlying Silicon and BOX layers (step 8).

9) Silicon wafer preparation and getter deposition

A bilayer of Ti/Au is full-sheet deposited on the front-side of the wafer and chemically etched in correspondence of the cavities hosting the SNR resonators. Then, Silicon is etched through down to a $200\mu m$ thickness via anisotropic etching by *ICP* to define the cavities hosting the *SAES* getter material. The latter is deposited through a shadow mask. Figure 2.19 shows the manufacturing steps performed up to this point.
Finally, Eutectic bonding is performed between the bottom Silicon wafer and the SOI/glass stack (figure 2.20).

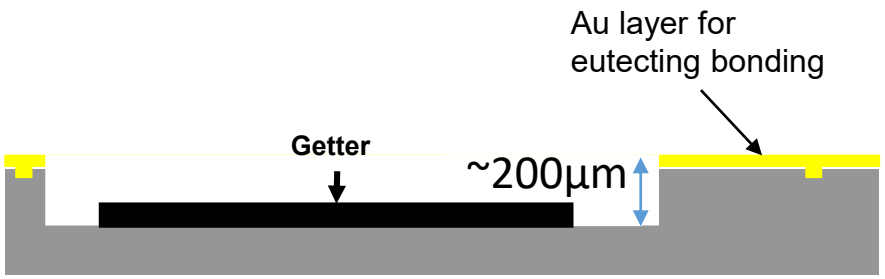

Figure 2.19. Cross section of the Silicon wafer after gold deposition for eutectic bonding, $200\mu m$ Silicon etchig and getter deposition (step 9).

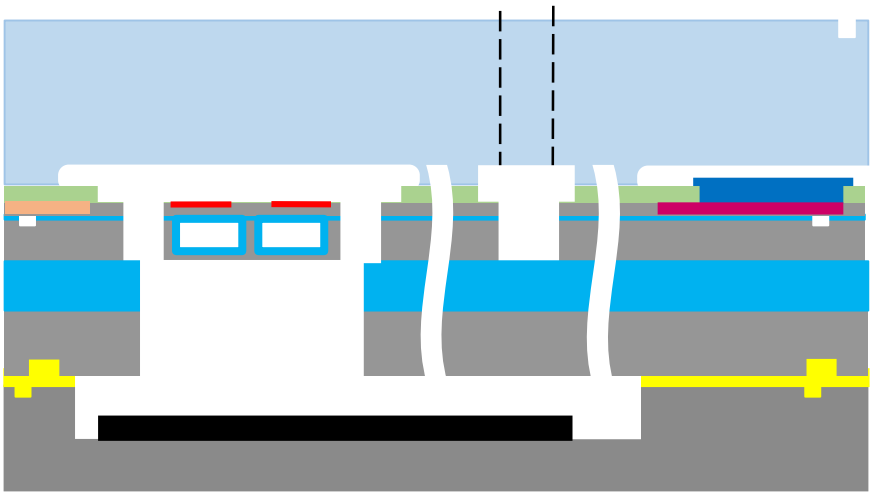

Figure 2.20. Cross section of the full stack of Silicon/SOI/SOI/glass wafers being patterned and implanted to manufacture SNR devices of different types. The eutectic bonding of the bottom Silicon wafer with the SOI/glass wafers stack is shown (step 9). A glass lid protects the underlying metal pads from oxidation until the device is ready to be used.

Chapter 3

Exploring the capabilities of SNR sensors through simultaneous piezoresistive readout of multiple resonators

As mentioned before in chapter 1, Suspended Micro/Nanochannel Resonators are extremely versatile in terms of the type and nature of samples they can detect, the fluid in which particles are suspended in, and the physical properties they are able to measure, such as mass, density and stiffness. In chapter 2 I described how a piezoresistive gauge embedded in a hollow cantilever structure has been designed, optimized and fabricated at such small scales. This achievement is crucial to allow simultaneous readout of several resonators at the nanoscale: a number of SNRs can in fact be connected fluidically in series or in parallel allowing for different functionalities with respect to the single-resonator SNR. The latter case allows for an increase in throughput that makes measurements faster without affecting accuracy; thinking about a future market application, SNR sensors would be built in parallel

arrays so as to be competitive with other techniques for characterization of nanoparticles in suspension in terms of measurement speed. The piezoresistive readout capability has already been successfully implemented for hollow microcantilevers (like the SMRs [20]) but to date, there is no report of any hollow nanocantilever that embeds both a fluidic channel and a shallow piezoresistor allowing an electrical readout of resonance frequency. Hence, the focus of this chapter, and conversely of my internship period in the Manalis lab, is first the analysis of the performances of the electronic piezoresistive readout mechanism compared to the optical readout mechanism previously used for SNR, and then the implementation of the parallel array SNR design (so-called pSNR). I will be describing the methods used to actuate the sensors, the technologies used to acquire data and extract the sample buoyant mass, and the characterization measurements that I have performed on the pSNR do demonstrate its functionality. The goal is to show the potentialities of the piezoresistive readout mechanism and pSNR technology in terms of stability, resolution, and speed.

3.1 Piezoelectric driving of resonators and resonance frequency detection methods

SNR resonators are piezoelectrically driven: the manufactured chips that contains the SNR oscillator, the bypass channels and the inlets are mounted on top of a PCB which incorporates a piezoelectric ceramic (American Piezo Co. APC841). A FPGA board (Altera Cyclone IV on DE2-115) generates a sinusoidal signal at the SNR's resonance frequency f_r which drives the ceramic's oscillations making the suspended beam resonate. The SNR's frequency is continuously measured and its value is fed back into the FPGA which is programmed to keep the driving signal fixed at f_r. To quantify the displacement of the resonators over time and consequently their resonance frequency, two different approaches can be used involving either an optical lever method or a piezoresistive measurement. The latter is typically simpler to implement and use but requires more effort on the manufacturing of the SNR. A quick review of the components and functionality of these setups is give here.

Optical setup: a LASER beam is reflected by the resonator surface and tracks its frequency of deflection

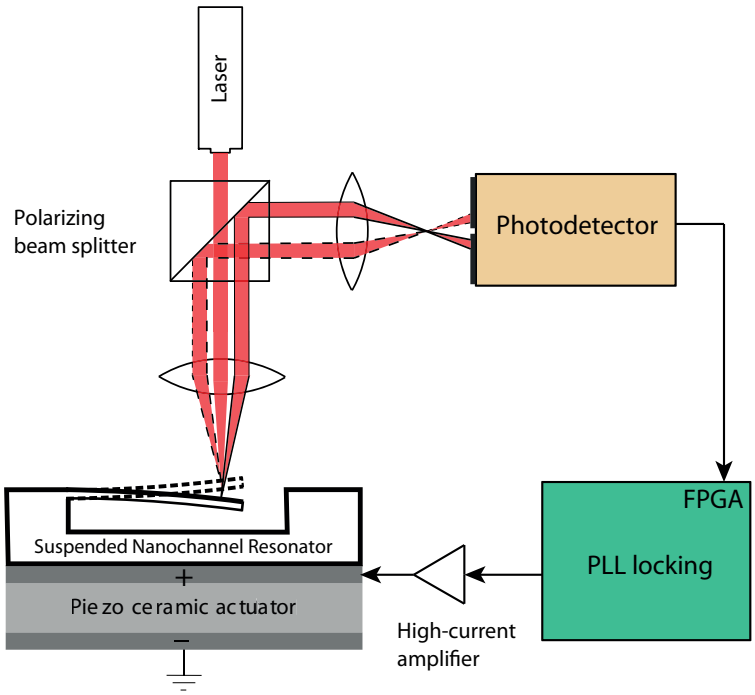

Figure 3.1. Schematics of the optical setup readout mechanism for the SNR's closed-loop resonance frequency detection and driving of the piezoceramic actuator.

The optical measurement is performed using the well-established optical lever method: a LASER beam (coherent source at 635 nm, 5 mW power) is reflected by the SNR cantilever's tip and is focused at the middle point of a split photodiode (Hamamatsu S4204) [19]. When the resonator's tip oscillates at a certain resonance frequency f_r, the beam moves sideways on the two faces of the photodiode which transforms the optical signal into two electrical signals of frequency f_r. As the two resulting waves are in phase opposition, it is possible to extract the amplified differential signal at the same frequency. The latter is converted into a digital signal (Terasic AD/DA conversion board) and fed to the FPGA which is programmed to perform a Phase-Locked Loop (PLL) feedback function [29]: the resonator's driving signal will be adjusted to keep the cantilever oscillate at its fixed resonance

frequency in a closed-loop manner (figure 3.1). The output signal of the FPGA is amplified by a high current operational amplifier (LT1210) providing $42dB$ gain, which is necessary to drive the piezoelectric ceramic. The user can interface with the setup using LabVIEW scripts (Appendix B): it is possible to set the driving amplitude of the SNR and the rate at which the resonance frequency is sampled. Resonators are usually driven with signals that maximize the signal-to-noise ratio while reducing the risk for trapping events at the tip of the U-shaped buried channel; to have the best signal-to-noise ratio, SNR should be driven at the onset on mechanical non-linearity [29, 33].

Electrical setup: a piezoresistive gauge senses the bending of the resonator

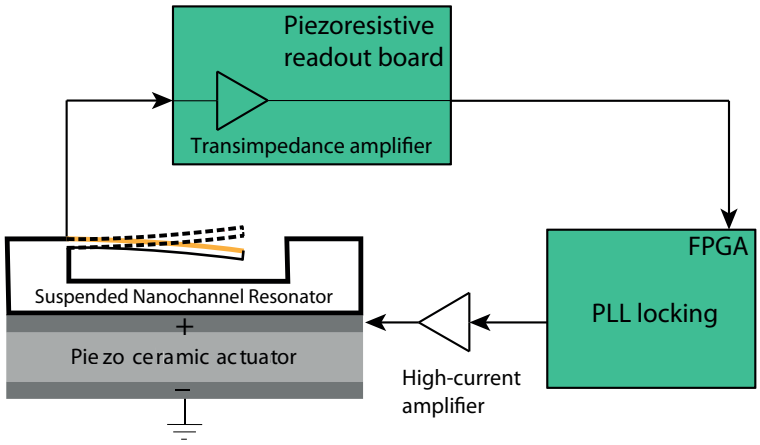

Figure 3.2. Schematics of the piezoresistive setup readout mechanism for the SNR's closed-loop resonance frequency detection and driving of the piezoceramic actuator.

To expand the functionalities of the SNR technology, a piezoresistive readout mechanism has been developed. As described in chapter 2, during SNR's manufacturing steps a piezoresistive gauge is built in the resonator, below the embedded nanofluidic channel. The measured gauge's resistance at rest is typically $\sim 6k\Omega$ and it is biased with a voltage of $V_b = 1V$ which in the context of this work has proven to be the value maximized the signal-to-noise ratio without overheating the

structure. The resonator is set into motion at a frequency f_r with the same PLL feedback loop used for the optical setup; as the cantilever moves up and down, the resistance of the gauge changes at a rate f_r due to the piezoresistive properties of p-doped Silicon [37]. The current variations are sensed by a transimpedance amplifier circuit that feeds a voltage signal to the FPGA (figure 3.2).
The immediate advantage of the electrical readout over the optical is the ease with which the user can set the buoyant mass measurement: while the electrical setup is "plug-and-play", the optical requires some user experience for the collimation of the LASER, the alignment of the beam's spot on the cantilever's tip, and the alignment of the reflected beam at the middle point of the split photodiode. The optical setup is also bulkier and it requires additional instrumentation, lenses and mirrors, and an optical microscope for the alignment step; the piezoresistive setup only needs a readout board and the FPGA implementing the PLL feedback function. Moreover, the piezoresistive setup allows for the simultaneous readout of several resonators: the parallel and density designs rely on this capability. Each of the 10 cantilevers in the parallel array SNR oscillates at its own resonance frequency. Each signal is individually sensed by a dedicated transimpedance amplifier and processed by the FPGA which is able to multiplex between the 10 frequency components of the signal.
The main drawback of the piezoresistive setup over the optical lever method is that it has to rely on the efficiency of the manufacturing process: unfortunately, at the current first stage of this technology, some of the piezoresistive gauges may not be properly connected to the metallic pads used for wire-bonding to the PCB, resulting in resistance values being too high ($\sim$ tens or hundreds of $M\Omega$) with respect to the typical measured value of $\sim 6k\Omega$ and detected resonance peaks being too faint to properly lock the feedback loop on a fixed f_r value. When dealing with parallel array SNRs, the measured yield in a 10-cantilevers chip of resonators whose deflections can be sensed piezoresistively is typically 70-90% (figure 3.3).

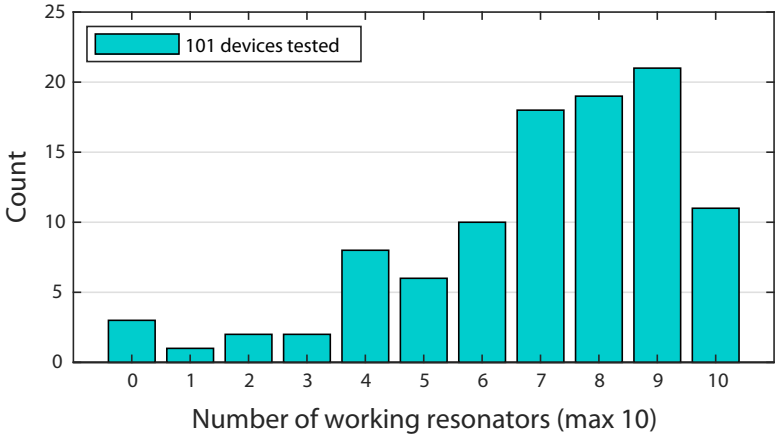

Figure 3.3. Yield statistics pSNR arrays that I tested during my training at Manalis lab. A total of 101 pSNR devices (A0 and A1, table 1.2) were tested as the buried channels were still empty (without any fluid loaded in the chip). Typically, only 7 – 9 resonators out of the 10 that are built have a resonance frequency which can be sensed in open-loop mode (figure B.2). Only a few (>10) of the tested pSNR chips had all 10 resonators being functional.

3.2 How does the optical readout compare to the piezoresistive readout?

While the optical readout mechanism is well-established for both SMR and SNR technologies, the piezoresistive readout mechanism had never been tested before for nanoscale hollow fluidic structures. I therefore studied the frequency stability of SNR's first mode resonance frequency using the piezoresistive scheme and I compared the results of this analysis with the ones I obtained through the optical readout mechanism. For this purpose, the Allan deviation analysis is typically the preferred method in literature [19, 16, 38]. The Allan deviation σ_f of a cantilever's resonance frequency in a given averaging time τ is [19, 39]:

$$\sigma_f(\tau) \simeq \sqrt{\frac{1}{2(N-1)} \sum_{k=2}^{N} \left(\frac{\bar{f}_k - \bar{f}_{k-1}}{f_r} \right)^2} \tag{3.1}$$

where $\bar{f}_k$ is the average resonance frequency over the time τ and N is the number of possible divisions of the total time T_{meas} over which resonance frequency data is collected. f_r is the average resonance frequency over the whole measurement time

T_{meas}.

$$\tau = \frac{T_{meas}}{2^N} \tag{3.2}$$

The highest number of divisions N_{max} is set by the measurement sampling rate f_s:

$$N_{max} = T_{meas} \times f_s \tag{3.3}$$

The Allan deviation gives an information on different frequency noise components when the averaging time τ is small and approaches the measurement sampling rate, and information on the drifting of the resonance frequency baseline over larger times. Moreover, it is possible to convert the Allan deviation, which effectively is a relative change in frequency $\frac{\delta f}{f}$, into an absolute mass resolution using the formulation derived from equation (1.7):

$$\delta m = -2\, m_{eff} \frac{\delta f}{f} \tag{3.4}$$

The effective mass m_{eff} can be extracted from the geometrical properties of the resonator in use (equation (1.2)) or it can be obtained through the measurement of resonance frequency and responsivity:

$$m_{eff} = \frac{f_r}{2R_m} \tag{3.5}$$

For the purpose of this analysis, the second approach was used as it accounts for variability in the manufacturing process meaning that it offers a more accurate estimate of the effective mass with respect to the modeled value. The resonance frequency f_r is measured by performing an open-loop frequency sweep of the piezoelectric ceramic driving signal and analyzing the resonator's response (figure B.2); the responsivity R_m is extracted from the calibration of SNR through gold nanoparticles, as described in chapter 1 (equation (1.9)). Considering $\sigma_f = \frac{\delta f}{f}$, the mass limit of detection at the averaging time τ is:

$$\delta m(\tau) = -\frac{f_r}{R_m} \sigma_f(\tau) \tag{3.6}$$

To perform the Allan deviation analysis on the piezoresistive readout mechanism I chose to use a device of type *SNR1* with the purpose of comparing later on in this chapter the frequency stability of a single-resonator SNR with that of a parallel SNR array; the best mass resolution in a pSNR is achieved using the *A1* type

(table 1.2) which is indeed comparable to that of a *SNR1* resonator. The chosen device has a fairly high quality factor Q = 2,480 allowing for low values of noise and consequently of mass detection [28]. In both piezoresistive and optical setups, the sampling rate, measurement bandwidth and piezoelectric ceramic driving amplitude are the same and they are optimized to maximize the signal-to-noise ratio. The same parameters were also set for the parallel SNR array device that was used for the frequency stability comparison with the single-resonator SNR: more details on this analysis will be given later on in this chapter. Filtered ($200nm$) de-ionized water was forced to run through the buried channel for T_{meas} = 60 minutes at a fixed pressure between the sample-load and the sample-collect bypass channels, while the resonance frequency of the cantilever was being measured with either one of the readout mechanisms. T_{meas} was set considering a worst-case typical timescale for low-concentrated samples flowing through single-resonator SNR. The Allan deviation was then extracted for both measurements and converted to limit of mass detection (figure 3.4).

The results of this analysis show that a high-Q resonator of type *SNR1* with optimized driving parameters can reach a minimum limit of detection of $\delta m_{min} \sim 10ag$ for both the optical and piezoresistive schemes. This mass resolution is ideal for measuring biological matter such as exosomes and viruses which have buoyant masses in water in the order of tens of attograms (Appendix D). Overall, the two methods yield equivalent results in terms of frequency stability versus averaging time meaning that optical and piezoresistive setups can be used interchangeably without introducing any significant source of noise into the measurement system. The promising results obtained with this analysis led to the use and characterization of the parallel SNR array technology which will be described in the following sections of this chapter: from this point forward, only the piezoresistive readout mechanism is used.

3.3 Measuring properties of pSNR and its figures of merit

To investigate the performances of the parallel SNR array technology (pSNR) I designed and carried out several experiments that are reported in this chapter. The

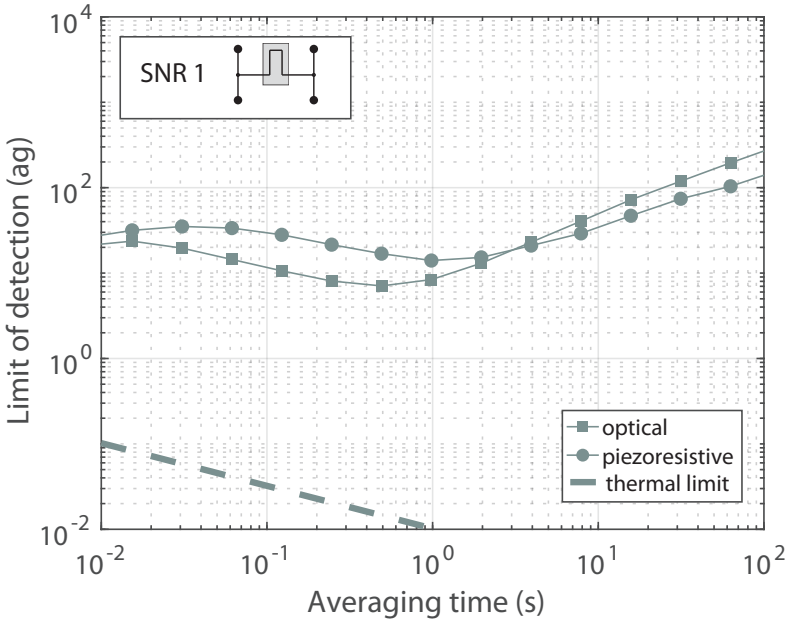

Figure 3.4. Comparison of Allan deviation analyses based on noise measurements performed with the same *SNR1* (table 1.1) device on the electrical and optical readout systems. The device quality factor is $Q = 2{,}480$, the measurement bandwidth is $BW = 100Hz$, the sampling rate is $6{,}25kHz$ (see figure B.3). The solid lines represent the extracted Allan deviations converted into limit of mass detection in attograms for the piezoresistive (circles) and optical (squares) readout mechanisms; the results are compared to the thermomechanical limit of detection, computed for a fixed-free beam. Inset shows top view schematic of cantilever (grey box) where black lines denote the fluidic channels and black dots the fluidic inlets and outlets.

focus is on the increase of throughput that pSNR allows with respect to a single-resonator SNR device, then I will talk about the throughput dynamic range with respect to sample concentration, the frequency stability (Allan deviation analysis) and how it compares to a single-resonator SNR, and finally the ability to measure polydisperse samples using pSNR and the technology's mass limit of detection. Generally speaking, it was observed that using a pSNR design made of an array of N resonators makes is possible to obtain a N-fold increase in throughput, and consequently a N-fold decrease in measurement time, with respect to a single-resonator SNR. As the following data will show, this improvement comes with almost no drawback with respect to a single-resonator SNR in terms of the the

devices mass limit of detection.

3.3.1 pSNR allows for a 9-fold increase in throughput

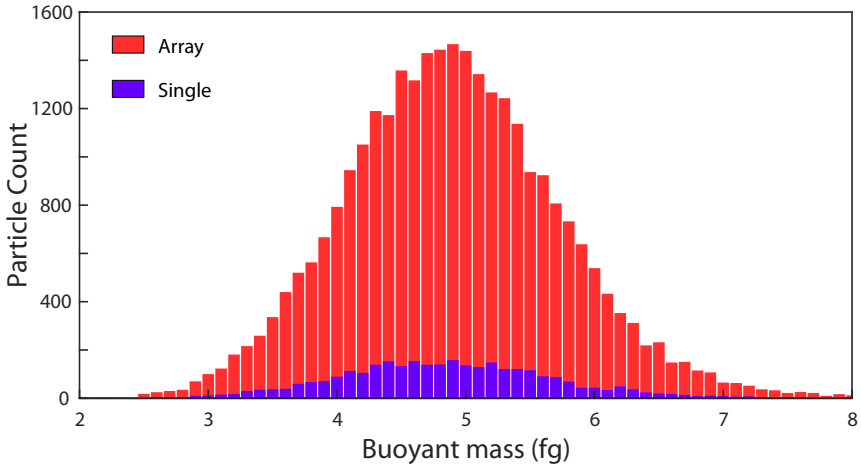

Figure 3.5. Comparison of 80nm-diameter gold nanoparticles count events in a 44 minutes long experiment between a single-resonator SNR (blue histogram) and a parallel array of SNRs (red histogram). A total of 29,347 particles were counted using the pSNR array and 3,133 were counted during the same time using the single-resonator SNR. The coefficients of variation in diameter are $CV = 5.6\%$ for the single-resonator SNR and 5.7% for the pSNR array.

A sample of 80nm-diameter gold nanoparticles (*BBI*, Coefficient of Variation CV $< 8\%$ [40]) with a concentration of 3.310^9 particles/mL was measured using a pSNR device of type *A0* and the results were compared with the ones obtained measuring the same sample with a single-resonator *SNR0* device, which has similar geometry and resonance frequency as the pSNR (tables 1.1, 1.2). The pSNR chip that I used for this analysis had 9 out of 10 resonators whose embedded piezoresistors were properly connected to the metallic pad on Silicon, which resulted in a 9.37 times increase in throughput with respect to the single-resonator SNR device of the same type (figure 3.5); the concentration of the sample, the duration of data acquisition, and the flow rate of particles going through the buried channel were kept the same for both measurements (figure 3.6). I found that average buoyant mass, particle count and coefficients of variation are equivalent throughout the array (figure 3.7). Using the current fluidic setup it was relatively challenging to set exactly the same

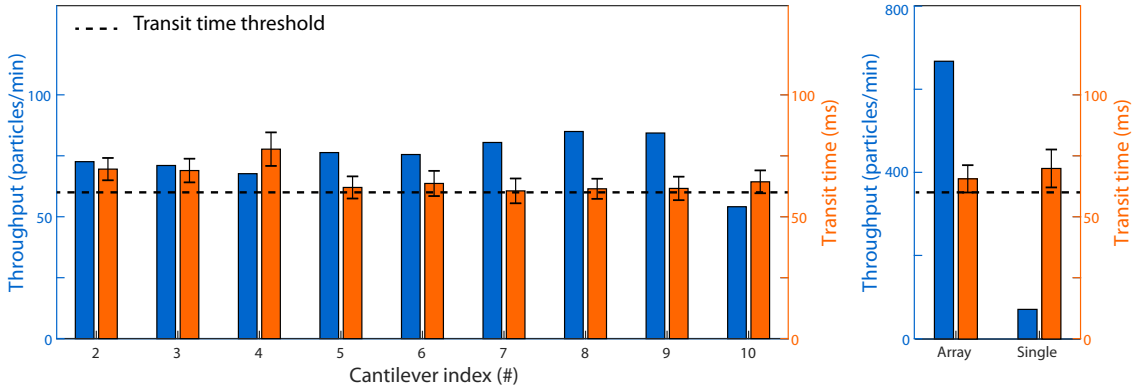

Figure 3.6. Summary of throughput and transit time per cantilever in pSNR and a single-resonator SNR. In the left bar plot the throughput and transit time of particles flowing in each SNR in the 9-resonators array used for the measurement in figure 3.5 is reported. The summed throughput and the averaged transit time are reported in the left bar plot and they are compared with the throughput and transit time of nanoparticles flowing in a single-resonator SNR of the same type as the array.

flow rate in different sets of experiments. Moreover, the sample runs through each resonator in the pSNR chip with a different transit time which is not controllable by the user. As a result, the average transit time of particles through the 9 resonators in the pSNR (i.e. $69.78ms$) is slightly larger than the transit time of particles in the single-resonator SNR ($65.54ms$) resulting in an increase in throughput which is larger than the expected $9\times$: the measured single-resonator SNR throughput is 71.20 particles/minute, while for the pSNR this value is 666.98 particles/minute. For this experiment, the flow rate of particles was pushed to the limit of transit time Δt_{tr} (i.e. the time difference between the moment the particle enters the resonator and the time at which it goes out of it) that can be achieved with a particular measurement bandwidth BW to maximize the throughput at a given sample concentration.

$$\Delta t_{tr} > \frac{12}{BW} \tag{3.7}$$

This rule was set for SNR based on the previous work done for these devices and the analysis of the resonance frequency peak distortion due to the CIC filter embedded in the PLL feedback mechanism [29] that I will elaborate on in the next section of this chapter. For transit times lower than the limit in euqation (3.7), the resonance frequency shift peak emerging from the passage of a particle through the resonator

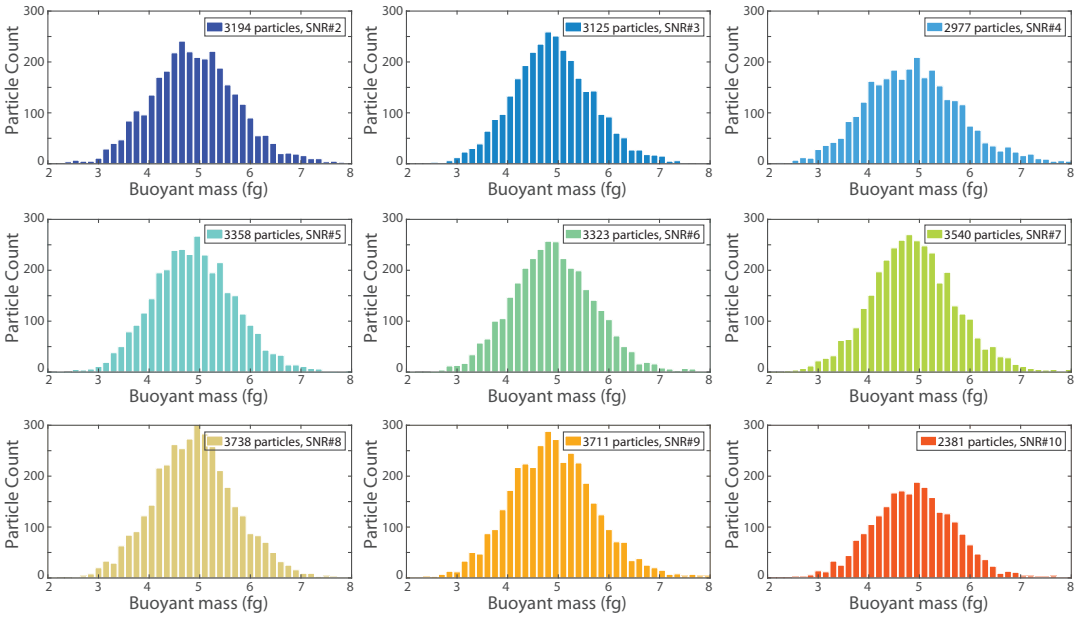

Figure 3.7. Buoyant mass histograms resulting from each of the 9 SNRs in the parallel array used for this analysis. The pSNR plot (red) shown in figure 3.5 is the result of a merging of these 9 histograms into a single one. Throughout the resonators distributed in the pSNR array, they all have equivalent average buoyant mass, throughput and coefficients of variation CV $\sim 5-6\%$.

is distorted and the particle's size is underestimated. In the measurements done for figures 3.5 and 3.6, the bandwidth was set to $BW = 200Hz$ resulting in a transit time limit of $\Delta t_{tr} = 60ms$. All resonators in the pSNR and the single-resonator SNR respect this limit to some acceptable degree of uncertainty. As the measurement bandwidth increases, the noise does as well so BW was set to a value that could preserve a good Signal-to-Noise ratio while maximizing the flow rate, typically in the range of $100Hz - 200Hz$.

Several pSNR devices were tested to find the one that would provide the maximum increase in throughput with respect to the single-resonator SNR. As it turns out, the yield of resonators working in piezoresistive mode in a pSNR array is not ideal and it is typically $70\% - 90\%$ (figure 3.3). Moreover, regardless of the number of properly connected resonators in an array, many pSNR chip failed quite rapidly after fluids have run through their channels for a while: typically a good chip did

not last for more than 2 days of measurements. This problem may lie in flaws in the design and fabrication steps and it is independent of the chosen readout mechanism. It was observed in fact that the vacuum chamber that encloses the 10 cantilevers in the array fails over time letting in either air or, worst case, the fluid currently in use. This particular technological flaw that does not affect single-resonator SNR devices probably may be due to a lower distance in pSNR between the vacuum chamber and the bypass channels: the contact area between the glass and Silicon layers is then reduced in pSNR with respect to single-resonator SNR meaning that the bonding is less effective. As a consequence, the resonators' quality factors Q degrade rapidly, and the magnitude of the resonance peak in the open-loop response (figure B.2) lowers making it harder for the PLL feedback loop to lock on f_r; the noise of individual resonators increases due to the lowering of Q and the increase in crosstalk between neighboring SNRs in the array (Appendix E).

3.3.2 Trading off transit time of nanoparticles with measurement bandwidth in pSNR

The resonance frequency measurement setup was simulated through a MATLAB model that has been developed in the Manalis lab: the response speed of the PLL feedback loop is limited by the CIC filter which can be modeled using a Butterworth low-pass filter [29]. The higher the bandwidth, the lower is the selectivity towards the resonance frequency the PLL system is trying to lock into meaning that the high-speed noise frequency fluctuations around the average value of f_r are not cutoff. Conversely, if the bandwidth is lower, the frequency noise is smaller but the transit time of nanoparticles going through the buried channel causing a shift in resonance frequency is limited by the speed of this transition compared to the value set for BW. The model implements equations (1.5) and (1.6) to extract the normalized resonance frequency shapes $f_r(t)$ of the cantilever during the passage of a nanoparticle through the U-shaped buried channel of a SNR resonator; the transit time of particles can be set and swept within a typical range, i.e. $10ms - 300ms$. The resonance frequency signal is then filtered through a Butterworth low-pass filter of order m and bandwidth BW, which are parameters that can be set by the user through the LabVIEW script that is used to control the PLL system (Figure B.3). Finally, the two resonance frequency shift shapes are compared at

different transit times. Figure 3.8 shows this comparison when particles are pushed with a flow rate such that the transit time is $\Delta t_{tr} = 10ms$ and $\Delta t_{tr} = 146ms$ while the bandwidth is set to three typical values used for the measurement of moderately fast particles, $BW = 100Hz, 150Hz, 200Hz$; the filter order is set to $m = 2$. The same analysis can also be performed by varying the bandwidth and parametrically sweeping the transit time. It is straightforward to notice that when

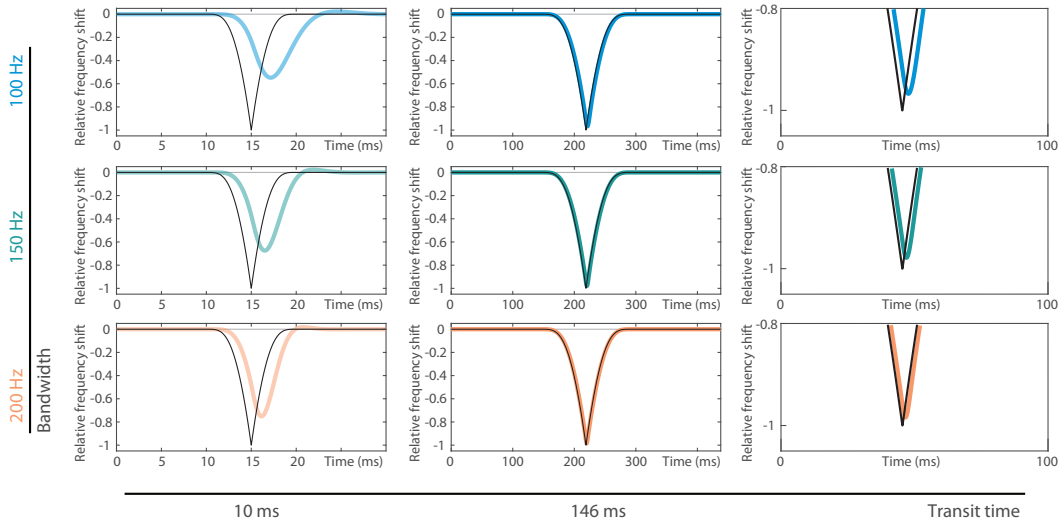

Figure 3.8. Simulation of the normalized time-dependent resonance frequency signal of a cantilever oscillating at its first flexural mode when a nanoparticle flows through the U-shaped buried channel. Different settings of transit time ($\Delta t_{tr} = 10ms, 146ms$) and measurement bandwidth ($BW = 100Hz, 150Hz, 200Hz$) are applied to the analytical model to study the distortion of resonance frequency shift peaks caused by the measurement system. The black thin lines in the plot represent the ideal response of the cantilever to a nanoparticle flowing through its embedded channel; the colored thick lines represent the actual filtered response of the system at different bandwidths. The left column shows different degrees of distortion for a low transit time. The middle column shows that for larger transit times the ideal and filtered signals overlap. The right column shows a zoomed-in image of the plots in the middle column: even though distortion is limited at high transit times, the peak height still depends on the bandwidth.

particles flow too fast in the buried channel ($\Delta t_{tr} = 10ms$) with respect to the bandwidth that was set by the user, the resonance frequency shift peak is distorted and its magnitude is not comparable to the unfiltered ideal peak leading to the underestimation of the analyte buoyant mass; this effect is largely reduced for slower

particles ($\Delta t_{tr} = 146ms$) but the peak height is still dependent on bandwidth. A careful quantitative analysis of this effect is needed to optimize the bandwidth-transit time trade-off. To do this, the energy spectral density of the resonance frequency is computed for both the filtered and unfiltered signals to understand what is the portion of the frequency spectrum that is cut out by the filter at a given bandwidth; their ratio, the so-called energy recovery, is plotted as a function of transit time for three typical values of bandwidth in figure 3.9. For a measurement

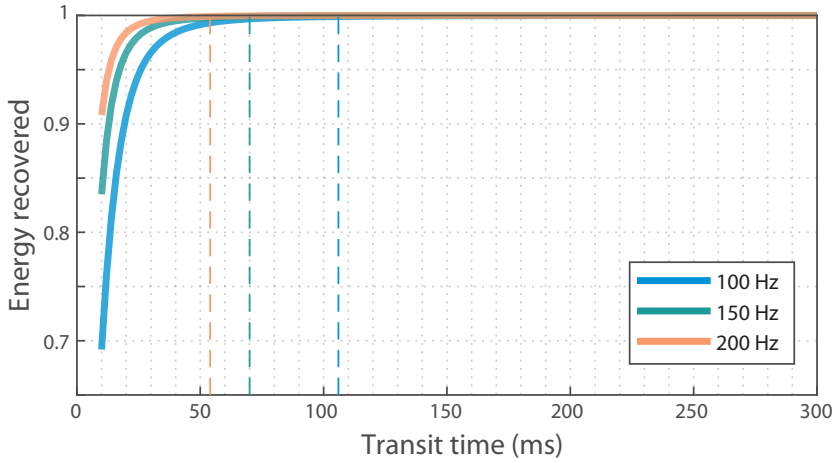

Figure 3.9. Energy recovery vs particles transit time of the resonance frequency signal being filtered by the CIC filter of order m and with a bandwidth BW with respect to the unfiltered signal. The energy spectral density of both the filtered and unfiltered resonance frequency signals is computed for all transit times in the studied range $10ms - 300ms$ and their ratio are plotted as a parametric function of the measurement bandwidth BW (solid lines). The dashed lines represent the transit time limits at each bandwidth for which 99.9% of the energy is recovered.

bandwidth $BW = 100Hz, 150Hz, 200Hz$, more than 99.9% of the energy spectral density is recovered (i.e. the ratio between the energy spectral densities of the filtered and unfiltered signals is $< 0.1\%$) when the transit time is larger than $106ms$, $70ms$ and $54ms$ respectively, leading to the following limit:

$$\Delta t_{tr,99.9\%} > \frac{10.5}{BW} \tag{3.8}$$

A second analysis is performed on the height of the first mode resonance frequency shift peak for both the filtered and unfiltered signals. Their ratio is plotted in figure 3.10 as a function of transit time and for three typical measurement bandwidth

values. This ratio is clearly growing at a slower rate than the energy recovery as

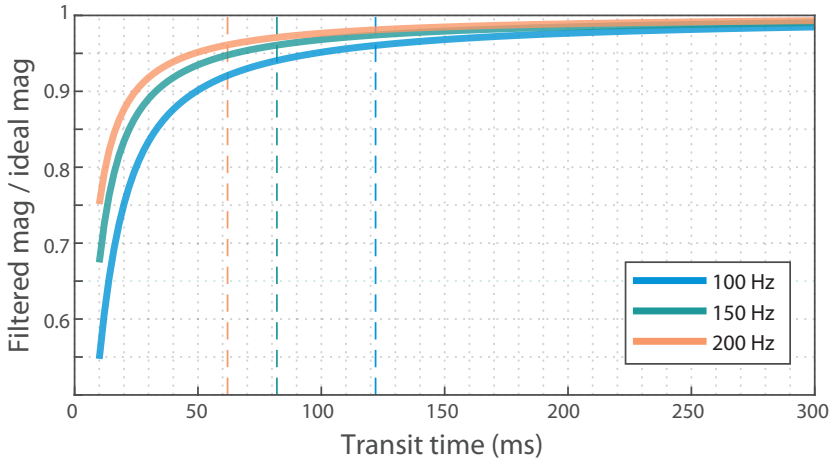

Figure 3.10. Ratio of filtered and unfiltered resonance frequency shift peak heights vs particles transit time (solid lines). The signal is filtered by a CIC filter of order m and with a bandwidth BW. The dashed lines represent the transit time limits at each bandwidth for which the ratio is $> 96\%$.

a function of particles transit time. To increase the measurement throughput of pSNR, the transit time limit was set by equation (3.7) which respects the energy recovery constraints and allows for a filtered-unfiltered peak height ratio $> 96\%$. For bandwidths $BW = 100Hz, 150Hz, 200Hz$, the minimum transit time is respectively $122ms$, $82ms$ and $62ms$.

The analytical model presented in this section is supported by data that I collected flowing $80nm$-diameter gold nanoparticles (*BBI*, CV $< 8\%$ [40]) at different speeds and fixed measurement bandwidth $BW = 100Hz$ through the buried channel of a single-resonator SNR of type *SNR0*; the results are shown in figures 3.11 and 3.12. The single-resonator SNR device was calibrated measuring the buoyant mass of the $80nm$-diameter gold nanoparticles sample flowing for 5 minutes through the buried channel at a speed larger than the limit set by equation (3.7), that is $\Delta t_{tr} = 148ms > \Delta t_{tr,lim} = 122ms$. The responsivity value was extracted from this measurement (equation (1.9)) and used to measure the buoyant mass of the sample which is ran at higher speeds; the same experimental settings were used for all measurements. Figure 3.11 shows indeed that measurements done for nanoparticles traveling with transit times lower than the limit cannot be trusted and figure

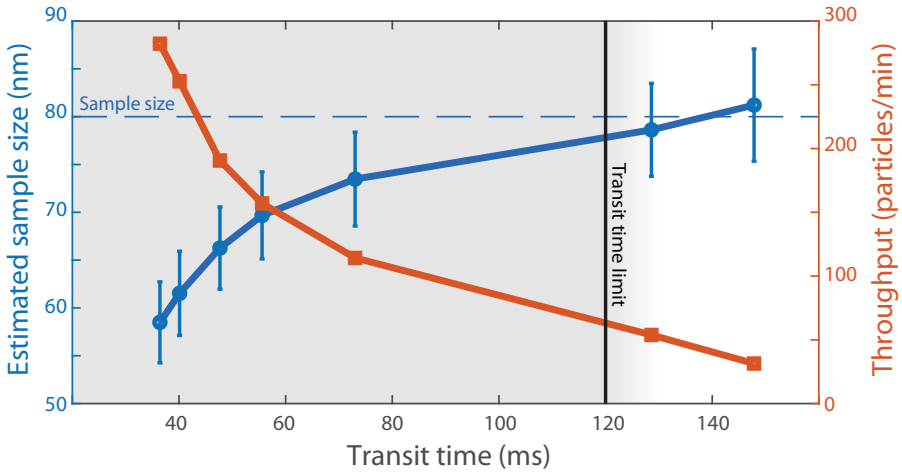

Figure 3.11. Estimated sample diameter (blue line) and measurement throughput (red line) vs particles transit time through the U-shaped buried channel of a SNR. The estimated sample size approaches the actual value (blue dashed line) when the transit time is set according to the rule in equation (3.7). The reference measurement (rightmost point in white area, $\Delta t_{tr} = 148ms$) was done with a transit time larger than the limit of $122ms$ (black vertical line) for this bandwidth; the measurement points in the gray region are all below the transit time limit so their sample size is underestimated.

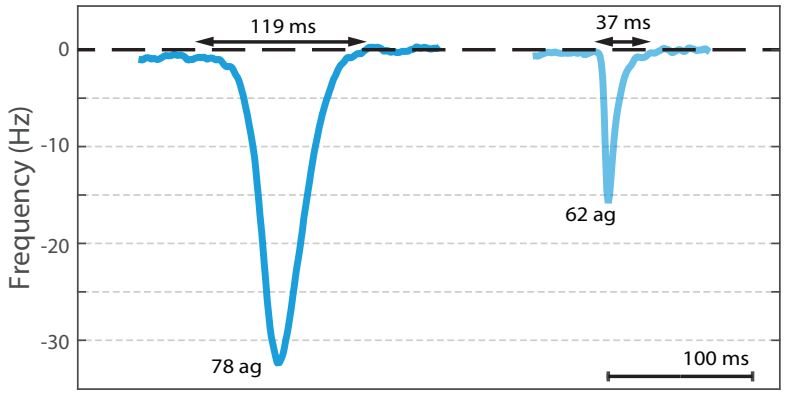

Figure 3.12. The resonance frequency shift distortion of a high-speed $80nm$-diameter gold nanoparticle going through the SNR is the cause of the mass underestimation. The plot shows the resonance frequency shift caused by two particles travelling at the transit time limit and below it. The peak is consequently smaller in height of a factor that fits with the analytical model.

3.12 shows the difference between a good measured resonance frequency peak and a filtered one. Effects such as the position-dependent error of nanoparticles reaching the U-turn of the channel at the tip of the cantilever (chapter 1, [27]) are not modeled in the analysis done so far but produce additional uncertainty in the height of the resonance frequency shift which may be dependent on the nanoparticles speed when flowing through the fluidic channel; in future works this phenomenon will have to be modeled analytically or through COMSOL simulations to be able to control its effect and to have a better fit of predictions to the measured data.

3.3.3 The limit of detection of buoyant mass is 10 ag for pSNR

In this section I present the work that I did to estimate the buoyant mass limit of detection for parallel SNR arrays through the Allan deviation analysis, similarly to what I did for a single-resonator SNR in the piezoresistive versus optical readout mechanisms comparison. Figure 3.13 shows the result of the Allan deviation analysis performed on the 8 active resonators in a pSNR device of type *A1* (table 1.2). σ_f was then converted to the equivalent limit of mass detection in attograms by means of the formulas presented for the single-resonator SNR analysis (equation (3.6)). The device that was used for this analysis was optimal in terms of quality factor meaning that cross-talk between neighboring resonators and noise of individual SNRs were minimal: the quality factors in the array were in the range $Q \sim 2{,}000 - 4{,}000$, which are two to four times larger than the value set during the design optimization process, $Q_{opt} = 1{,}000$. As a consequence, the Allan deviation extracted for this pSNR device has the same behavior throughout the 8 resonators in use and the minimum mass limit of detection is in the relatively narrow range of $2-10ag$, outperforming the single-resonator SNR of type *SNR1* used in the analysis of figure 3.4; the same measurement bandwidth, sampling rate and measurement time were used for both cases.

Parallel SNR arrays match the performances of single-resonator SNR devices when the quality factors of the individual resonators are high as to minimize cross-talk between neighboring cantilevers. Typically for $Q > 1{,}000$ the open-loop frequency response of resonators in an array shows well defined resonance peaks (figure

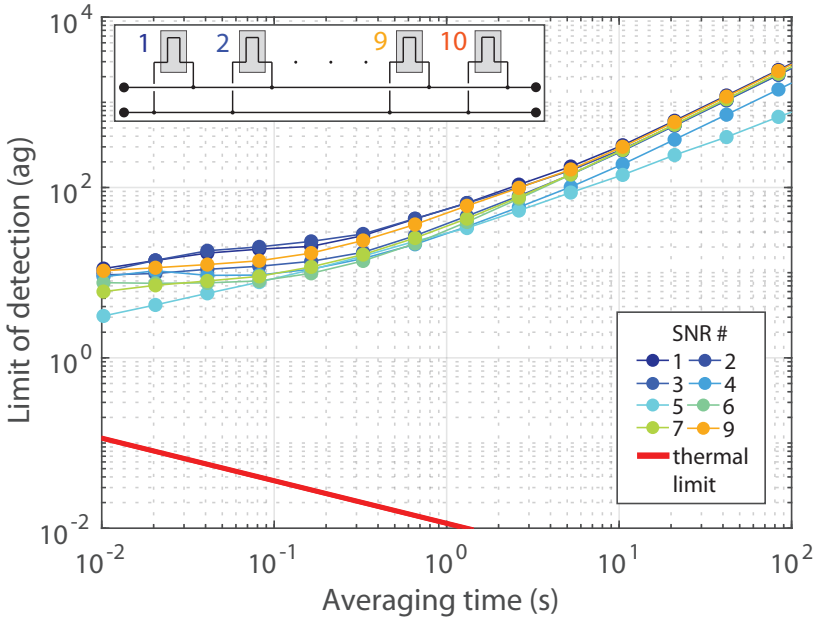

Figure 3.13. Allan deviation analysis of a pSNR device of type *A1* (table 1.2) with 8 resonators working in piezoresistive mode, each one having a high quality factor $Q \sim 2000 - 4000$. The measurement bandwidth is $100Hz$, the sampling rate is $6.25kHz$ (see figure B.3) and filtered ($200nm$) de-ionized water was forced to flow through the buried channel for 60 minutes. Each colored line represents the Allan deviation of a resonator in the array (same color scheme as the inset showing a schematics of the pSNR device) converted into limit of mass detection. The results are compared to the thermomechanical noise limit (red line) which is weakly dependent on the resonator geometry: all resonators have the same thermal limit to an acceptable degree of variation.

E.2); the filters implemented in each of the PLL feedback system dedicated to the N individual resonators are selective enough to efficiently cutoff frequency components resulting from the simultaneous excitation of the other $N-1$ cantilevers. Conversely, when the quality factor is smaller, adjacent resonance peaks in the open-loop frequency response tend to overlap and the filtering capability of the PLL feedback system is less effective. The manufactured cantilevers though are rarely so efficient in terms of quality factor and their measured Q is typically one order of magnitude lower than the value for which the optimization was carried out, $Q_{opt} = 1{,}000$ (figure 3.14). Single-resonator SNRs can be properly locked by the PLL feedback loop regardless of their efficiency, even though their buoyant mass

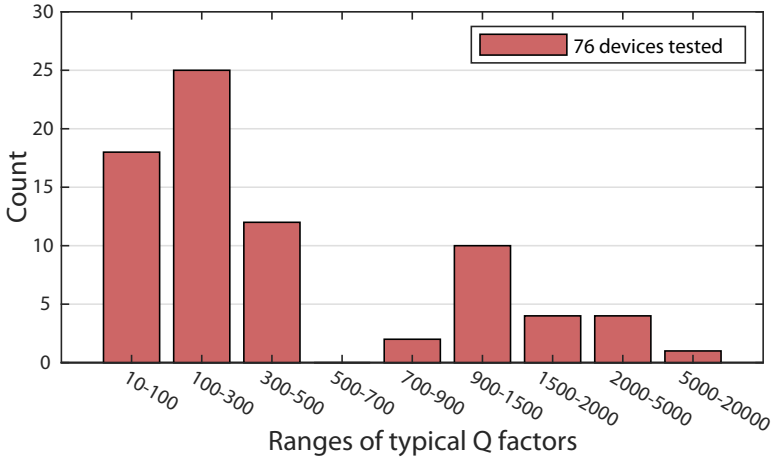

Figure 3.14. Quality factor statistics of pSNR arrays I tested during my training period at Manalis lab. Overall, within the same array, the typical quality factors of embedded resonators were equivalent to one another and out of 76 tested pSNR, a significant number of devices (>40) showed a quality factor $Q < 300$: the vacuum sealing of the chamber containing the array of resonators may not be as efficient as that of single-resonator SNRs. Based on empirical observation, only pSNRs whose resonators had quality factors $Q > 300$ could be effectively locked by the PLL feedback loop.

limit of detection worsens for lower quality factors. When it comes to parallel SNR arrays, relatively high quality factors play a crucial role into the functionality of the whole chip. I have observed that for $Q < 300$, the added noise and the cross-talk phenomenon make it impossible for the PLL feedback system to lock on all resonators in an array. As mentioned before, the vacuum of pSNR devices is generally worse than single-resonator SNRs which makes their quality factors degrade down to the most frequent range of values $Q_{typ} = 100 - 300$.

3.3.4 The dynamic range of detection of pSNR is limited at high concentrations

The dynamic range of throughput of pSNR arrays as a function of the sample concentration was measured and the results are shown in figure 3.15. $40nm$-diameter gold nanoparticles (*BBI*, CV $< 8\%$ [40]) were diluted several times in filtered ($200nm$) de-ionized water to obtain concentrations in the range 10^8 particles/mL to 10^{11} particles/mL. Each one of the twelve samples was measured using the same

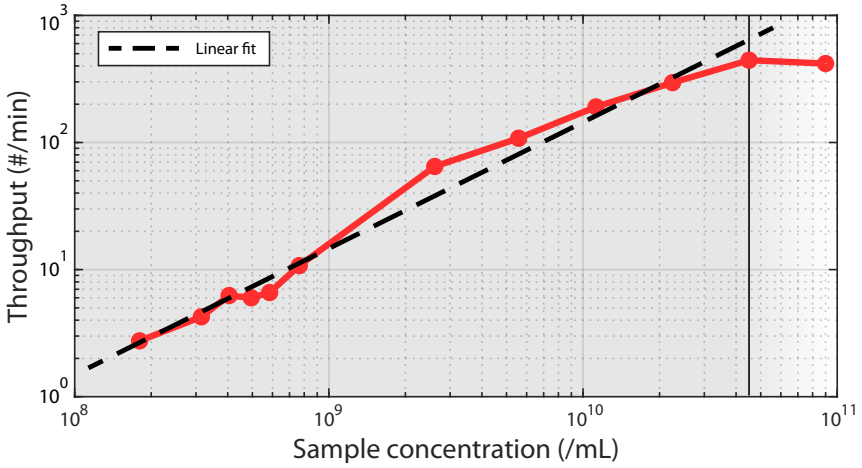

Figure 3.15. Dynamic range of measurement throughput (number of particles going through the resonator per minute) vs sample concentration of $40nm$-diameter gold nanoparticles. The red line shows the average throughput of 4 resonators in a pSNR array during 5-minutes experiments. The dashed line is the linear fit of data points in the linear region (gray area). The black solid line represents the highest concentration data point for which the plot can still be considered linear. Data is represented in a log-log plot and the first order fit of the measured points in the $10^8 - 4\ 10^{10}$ particles/mL range of concentration represents indeed a linear distribution as its slope in log-log scale is 0.99376. The 95% confidence interval of the fit's slope is $0.8913 - 1.0962$.

pSNR device of type *A1* (table 1.2) during a 5 minutes period; the bandwidth, the sampling rate and the sample transit time were kept the same throughout all the experiments (up to an acceptable degree of variability which is set by the accuracy of the pressure-control system). Data from each resonator have equivalent distribution of points and values throughout the array so the average throughput was extracted. For the purpose of measuring the throughput, it was not necessary to follow the rule of equation (3.7) limiting the transit time as the sample's buoyant mass was not estimated: the sample's flow rate is quite high for this analysis ($\Delta t_{tr} =\sim 45ms$ for a measurement bandwidth $BW = 150Hz$).

At low concentrations of the sample pSNR has no limit, provided that the number of particles entering the array of sensors is significant during the time frame of the measurement to extract a robust buoyant mass histogram (i.e. more than 100 counting events). Overall, the throughput scales linearly with the sample concentration up to a value of $\sim 4\ 10^{10}$ particles/mL. Above this limit, many nanoparticles may

flow simultaneously through the same resonator resulting in resonance frequency shift peaks overlapping one another (figure 3.16). As a result, part of the data acquired from highly concentrated samples is not reliable and has to be discarded by the MATLAB script that the research team in the Manalis lab developed thus limiting measurement throughput.

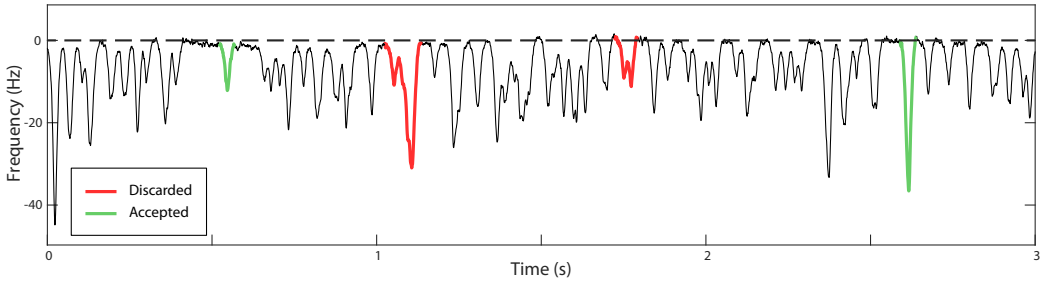

Figure 3.16. Time snapshot of the first-mode resonance frequency shift consequent to the flow of 40nm-diameter gold nanoparticles through the buried channel of an SNR; the sample is highly concentrated (9 10^{10} particles/mL) and double-occupancy events occur.

3.3.5 pSNR can measure polydisperse samples

One of the properties that make SNR technology competitive with respect to other techniques for size estimation of nanoparticles in solution like DLS is the ability to measure polydisperse samples and to discern populations of particles with different buoyant mass with high resolution. To demonstrate this capability, a polydisperse sample of 20nm, 40nm, and 60nm-diameter gold nanoparticles (BBI, CV $< 8\%$ [40]) was measured using a pSNR device (figures 3.17 and 3.18). The concentration of the three populations of particles suspended in filtered (200nm) de-ionized water were respectively 7 10^9 particles/mL, 3.9 10^9 particles/mL, and 3.02 10^9 particles/mL. The measurement was done using a pSNR array of type $A1$ (table 1.2) which has a better mass resolution (below 20ag, see Allan deviation analysis in figure 3.19) and sensitivity (typical values in the $15 - 20\,mHz/ag$ range) than the pSNR type $A0$. The measurement bandwidth was set to 150Hz and the transit times were conservatively set to 100ms, enabling a throughput of 438 nanoparticles/minute. Considering the 20nm-diameter gold nanoparticles have a buoyant

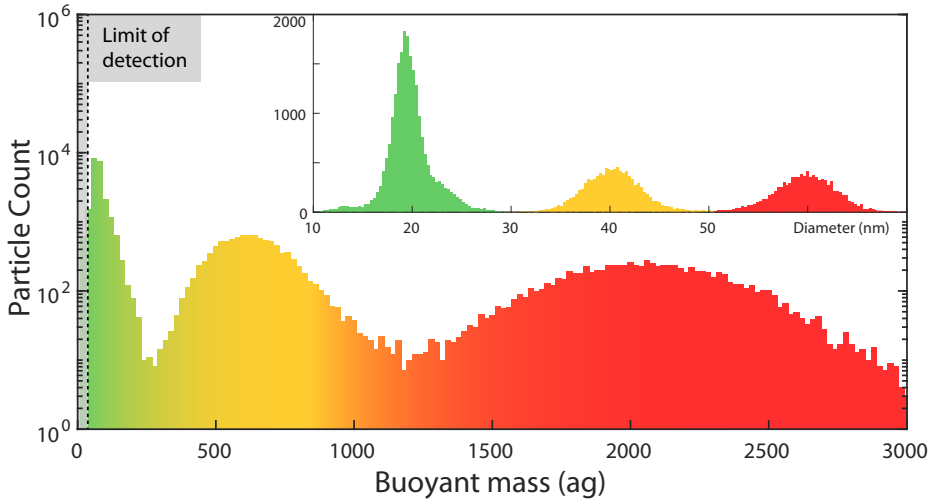

Figure 3.17. Polydisperse sample of $20nm$ (green), $40nm$ (yellow), $60nm$-diameter (red) gold nanoparticles measured through a pSNR array of type *A1*. The inset shows the diameter estimate of the three populations of particles which is extracted assuming spherical beads of uniform density. The gray area represents the practical limit of detection set in the MATLAB script for data post-processing: $47ag$.

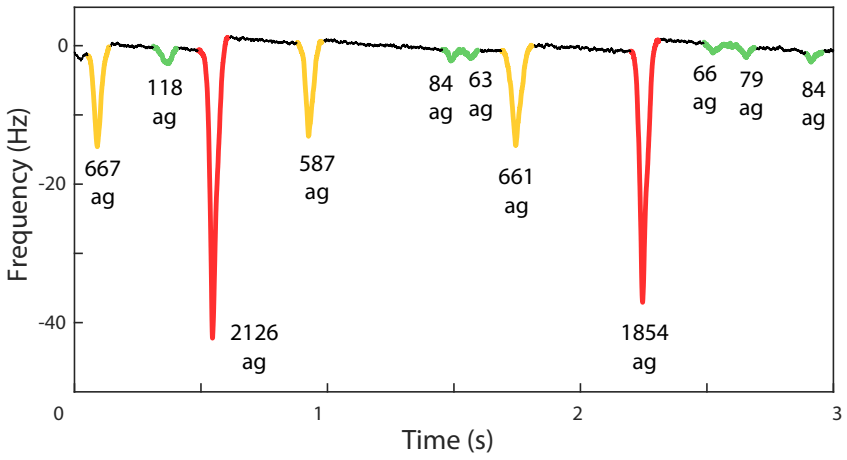

Figure 3.18. Time snapshot of the resonance frequency shift consequent to the flow of gold nanoparticles of different size (same color scheme as figure 3.17) through the buried channels of one of the resonators in a pSNR array. The buoyant mass in attograms extracted for all resonance frequency shifts is reported below each peak.

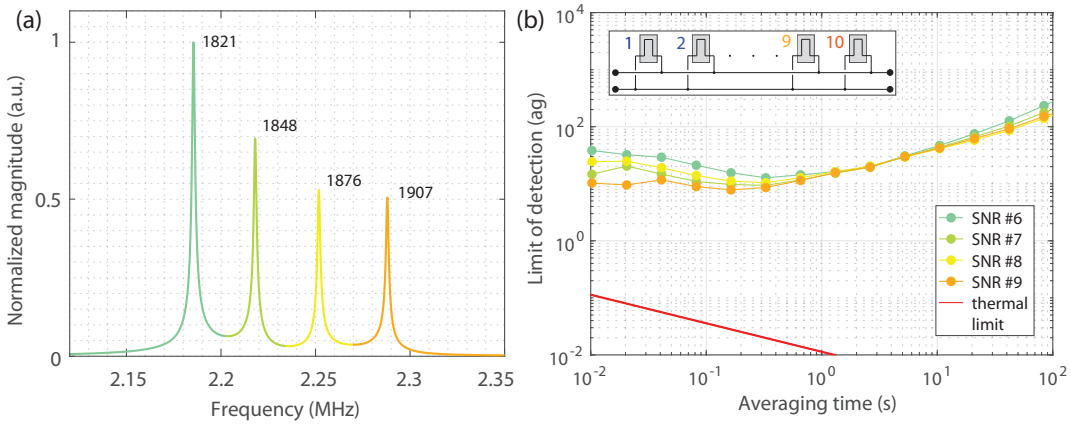

Figure 3.19. (a) Open-loop frequency sweep showing the resonance peaks of the SNR cantilevers in the pSNR array used for the analysis in figures 3.17 and 3.18.The quality factors of each of the four resonators in use are reported above each resonance peak. (b) Allan deviation analysis of the same resonators converted into limit of mass detection in attograms. The device in use has relatively high quality factors $Q \sim$ 2,000 and consequently has low limits of mass detection in the order of $10ag$.

mass $m_b(20nm) = 77ag$ which is relatively close to the mass detection limit of this device, the resonance frequency shift related to the flow of these beads through the buried channel of the cantilevers is small and quite close to the noise baseline (see green peaks in figure 3.18). The MATLAB script that was used to automatically recognize peaks from the collected data filters out all frequency shift points below a threshold which is set by the user to eliminate noise fluctuations. To be able to clearly distinguish a frequency shift peak from the oscillations of the noise baseline, the limit of detection threshold was set to $47ag$ for the four SNRs that were used in this pSNR device. The practical buoyant mass limit of detection of these SNR devices are indeed larger than the lowest mass resolution that can be estimated via Allan deviation analyses.

There is no appreciable variation of speed of nanoparticles flowing through the buried channels of different resonators distributed across a pSNR array, regardless of their size (figures 3.20a,b,c). Although the computed p-values for the nanoparticles transit time distributions don't allow for the null hypotheses to be discarded, it is reasonable to estimate transit times to be roughly the same for particles of

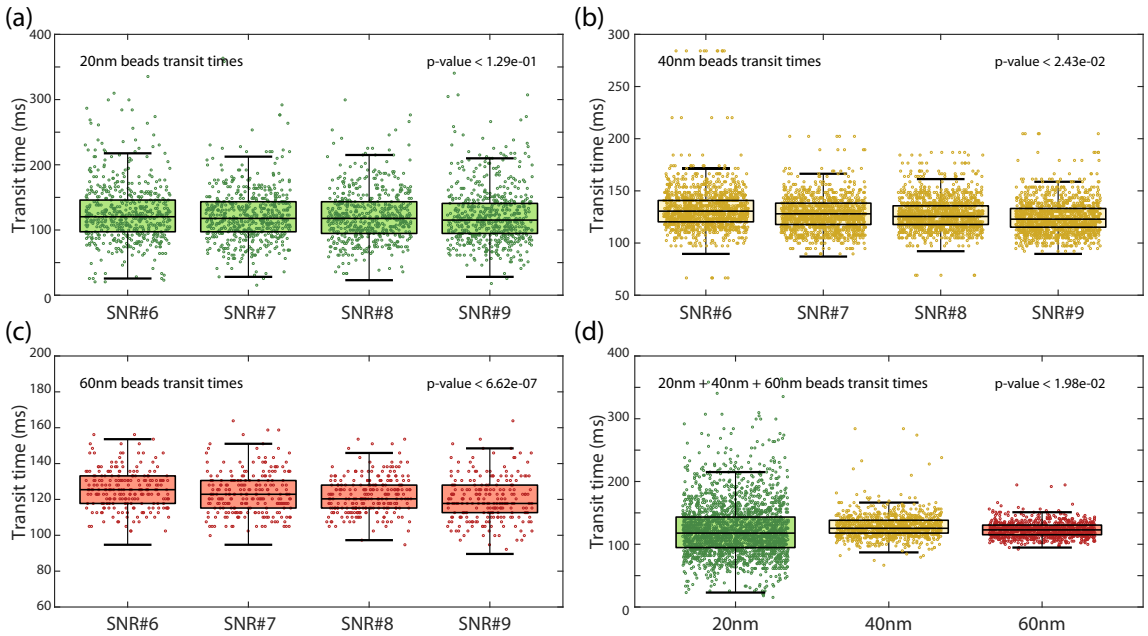

Figure 3.20. (a,b,c) Estimated transit times of $20nm$ (green), $40nm$ (yellow), $60nm$-diameter (red) gold nanoparticles through the 4 active resonators in a pSNR array. (d) Comparison between transit times grouped according to nanoparticles size. A tenth of the collected events are plotted in figures a-d.

the same size species flowing through 4 different resonators based on their mean values and standard deviation errors. Moreover, there is also no appreciable dependence of transit time on the diameter of particles that are much smaller than the cross section of the buried channel they flow through: flow rate is independent of sample size at this scale (see figure 3.20d). Once again, low p-values don't make it possible to claim that transit times are the same for the different size populations, but the low and non-monotonic variation of average transit time with respect to sample size do not allow to claim the opposite either. By observing that the average transit time and its standard deviation for the $20nm$, $40nm$, $60nm$-diameter gold nanoparticles are $(123.98 \pm 1.66)ms$, $(128.36 \pm 0.49)ms$ and $(122.86 \pm 0.41)ms$ respectively, one can claim that there is no appreciable difference in the transit times of nanoparticles suspended in the same water sample in this size order of magnitude.

In this chapter I have described the methods used to drive pSNR devices, measure simultaneously the resonance frequency of cantilevers in the array through the use of the newly implemented piezoresistive readout mechanism for hollow fluidic beams, and extract the buoyant mass of nanoparticles down to the attograms scale. To summarize, the piezoresistive readout mechanism offers equivalent performances to the well-established optical readout scheme and makes it possible to reach a mass resolution of $\sim 10ag$ for single-resonator SNR and pSNR devices of types *SNR1* and *A1* respectively. In fact, no significant difference in terms of limit of mass detection was observed between the two variants of the technology as long as the quality factors of the analyzed resonators are high enough as to allow simultaneous locking of all the resonators within an array, minimizing the effect of cross-talking between neighboring cantilevers. This constraint is crucial for pSNR operation and some improvements to the existing technology could be implemented to make these devices more reliable. Nevertheless, I characterized the performances of pSNR and compare them to the single-resonator SNR that could already be used through the optical readout mechanism: pSNR can offer a N-fold increase in measurement throughput or a N-fold decrease in measurement time without degrading the buoyant mass limit of detection or any other property that make SNR competitive with respect to other nanoscale characterization methods such as the ability of measuring polydisperse samples and the wide range of sample concentrations that can be detected.

Chapter 4

Conclusions and outlook

Shallow ($\sim 100nm$ thick) piezoresistive gauges were successfully embedded in the hollow cantilevers of Suspended Nanochannel Resonator devices thanks to a design study that optimized several geometrical parameters to reach attogram scale mass detection limit while electrically confining the piezoresistive element in a region where it is not exposed to the fluidic components of the device. Several simulations were performed to make sure that variations in the optimized parameters due to manufacturing process errors would not affect the mass resolution of SNR. The piezoresistive readout mechanism was tested using high-quality factors single-resonator SNR devices and compared to the performances of the optical lever readout scheme. The results of this analysis demonstrate that no relevant difference occurs between the two readout systems and that a limit of mass detection of 10 attograms, an order of magnitude higher than the designed value, can be achieved. The success of the piezoresistive readout gauge integration into hollow cantilevers paved the way for the design of different SNR architectures that allow additional functionalities with respect to the single-resonator technology: serially connected SNRs are able to measure the density of a sample, while parallel arrays of SNRs increase the number of particles that are measured within a timeframe. Parallel SNRs were demonstrated to allow a 10-fold increase in measurement throughput with respect to the single-resonator SNR, leading to a likewise decrease in measurement time: buoyant mass data of analyte particles flowing through the fluidic channels of this device can be collected in a few minutes. This improvement comes with no degradation of the performances of the low-throughput device: the limit

of detection is equivalent, the sample concentration dynamic range of detection is in the $10^8 - 10^{11}$ particles/mL range, the device is able to measure polydisperse samples. More than 100 parallel SNR arrays were tested and some statistics on their performances could be extracted: unfortunately, at the current stage of this technology the number of devices that work in a regime that approaches the optimized and predicted one is relatively small. The yield of SNRs in the array that can detect buoyant mass in piezoresistive mode is typically $70 - 90\%$: the gauge sensors may be not properly connected to the SNR chip metal pad due to errors in the manufacturing process. Moreover, the typical quality factor of SNRs in the array is in the $100 - 500$ range, as opposed to the designed 1,000, and devices fail quite rapidly in time. The bypass channels may be too close to the vacuum chamber enclosing the array of sensors leading to less-than-ideal vacuum sealing that fails rapidly due to either air or water filling the camber. Further optimization and design steps should be carried out in future works to limit these problems and maximize the efficiency and lifetime of these devices.

This technology is envisioned to reach measurement times lower than 10 minutes by the fabrication of devices with more than 10 SNRs in the array and by using post-processing methods currently developed in the Manalis lab that make it possible to overcome the bandwidth vs transit time limit and make particles flow even faster. Once the design is further optimized and the manufacturing problems are solved, the parallel SNR devices could be used for measurements of physical properties that go beyond the buoyant mass sensing; second mode actuation of the cantilevers would provide the means to measure stiffness and to eliminate the particles position-dependent error.

Bibliography

[1] Kim Hyun-A et al. “Nanometrology and its perspectives in environmental research”. In: *Environmental Analysis Health and Toxicology* 29.0 (2014), e2014016–. DOI: 10.5620/eht.e2014016.

[2] Nathan Cermak et al. “High-throughput measurement of single-cell growth rates using serial microfluidic mass sensor arrays”. In: *Nature Biotechnology* 34.10 (Sept. 2016), pp. 1052–1059. DOI: 10.1038/nbt.3666.

[3] Joon Ho Kang et al. “Noninvasive monitoring of single-cell mechanics by acoustic scattering”. In: *Nature Methods* 16.3 (Feb. 2019), pp. 263–269. DOI: 10.1038/s41592-019-0326-x.

[4] Scott M. Knudsen et al. “Determination of Bacterial Antibiotic Resistance Based on Osmotic Shock Response”. In: *Analytical Chemistry* 81.16 (Aug. 2009), pp. 7087–7090. DOI: 10.1021/ac900968r.

[5] J. Lizbeth Reyes Zamora and Hector C. Aguilar. “Flow virometry as a tool to study viruses”. In: *Methods* 134-135 (Feb. 2018), pp. 87–97. DOI: 10.1016/j.ymeth.2017.12.011.

[6] J. J. Ruz et al. “Physics of Nanomechanical Spectrometry of Viruses”. In: *Scientific Reports* 4.1 (Aug. 2014). DOI: 10.1038/srep06051.

[7] Huilin Shao et al. “New Technologies for Analysis of Extracellular Vesicles”. In: *Chemical Reviews* 118.4 (Jan. 2018), pp. 1917–1950. DOI: 10.1021/acs.chemrev.7b00534.

[8] Zhigang Liu et al. “Immunomodulating Nanomedicine for Cancer Therapy”. In: *Nano Letters* 18.11 (Sept. 2018), pp. 6655–6659. DOI: 10.1021/acs.nanolett.8b02340.

[9] Mario M. Modena et al. “Nanoparticle Characterization: What to Measure?” In: *Advanced Materials* (May 2019), p. 1901556. DOI: 10.1002/adma.201901556.

[10] Jörg Stetefeld, Sean A. McKenna, and Trushar R. Patel. “Dynamic light scattering: a practical guide and applications in biomedical sciences”. In: *Biophysical Reviews* 8.4 (Oct. 2016), pp. 409–427. DOI: 10.1007/s12551-016-0218-6.

[11] Philip J. Wyatt. “Measurement of Special Nanoparticle Structures by Light Scattering”. In: *Analytical Chemistry* 86.15 (July 2014), pp. 7171–7183. DOI: 10.1021/ac500185w.

[12] Jean-Luc Fraikin et al. “A high-throughput label-free nanoparticle analyser”. In: *Nature Nanotechnology* 6.5 (Mar. 2011), pp. 308–313. DOI: 10.1038/nnano.2011.24.

[13] Robert Vogel et al. “Quantitative Sizing of Nano/Microparticles with a Tunable Elastomeric Pore Sensor”. In: *Analytical Chemistry* 83.9 (May 2011), pp. 3499–3506. DOI: 10.1021/ac200195n.

[14] Vasco Filipe, Andrea Hawe, and Wim Jiskoot. “Critical Evaluation of Nanoparticle Tracking Analysis (NTA) by NanoSight for the Measurement of Nanoparticles and Protein Aggregates”. In: *Pharmaceutical Research* 27.5 (Mar. 2010), pp. 796–810. DOI: 10.1007/s11095-010-0073-2.

[15] T. P. Burg and S. R. Manalis. “Suspended microchannel resonators for biomolecular detection”. In: *Applied Physics Letters* 83.13 (Sept. 2003), pp. 2698–2700. DOI: 10.1063/1.1611625.

[16] Roberta Calmo et al. “Monolithic glass suspended microchannel resonators for enhanced mass sensing of liquids”. In: *Sensors and Actuators B: Chemical* 283 (Mar. 2019), pp. 298–303. DOI: 10.1016/j.snb.2018.12.019.

[17] A. De Pastina, D. Maillard, and L.G. Villanueva. “Fabrication of suspended microchannel resonators with integrated piezoelectric transduction”. In: *Microelectronic Engineering* 192 (May 2018), pp. 83–87. DOI: 10.1016/j.mee.2018.02.011.

[18] Jungchul Lee et al. “Toward Attogram Mass Measurements in Solution with Suspended Nanochannel Resonators”. In: *Nano Letters* 10.7 (July 2010), pp. 2537–2542. DOI: 10.1021/nl101107u.

[19] S. Olcum et al. “Weighing nanoparticles in solution at the attogram scale”. In: *Proceedings of the National Academy of Sciences* 111.4 (2014), pp. 1310–1315. DOI: 10.1073/pnas.1318602111.

[20] J. Lee et al. “Suspended microchannel resonators with piezoresistive sensors”. In: *Lab Chip* 11.4 (2011), pp. 645–651. DOI: 10.1039/c0lc00447b.

[21] Yazdi N., Ayazi F., and Najafi K. “Micromachined Inertial Sensors”. In: *Proceedings of the IEEE* 86.8 (1998), pp. 1640–59.

[22] Derek K. Shaeffer. “MEMS inertial sensors: A tutorial overview”. In: *IEEE Communications Magazine* 51.4 (Apr. 2013), pp. 100–109. DOI: 10.1109/mcom.2013.6495768.

[23] P Ivaldi et al. “50 nm thick AlN film-based piezoelectric cantilevers for gravimetric detection”. In: *Journal of Micromechanics and Microengineering* 21.8 (July 2011), p. 085023. DOI: 10.1088/0960-1317/21/8/085023.

[24] Andrew N. Cleland. *Foundations of Nanomechanics - From Solid-State Theory to Device Applications*. Springer, 2003.

[25] Stephen Timoshenko and D H Young. *Vibration Problems in Engineering*. Princeton, N.J., Van Nostrand, 1961.

[26] S. Dohn et al. “Mass and position determination of attached particles on cantilever based mass sensors”. In: *Review of Scientific Instruments* 78.10 (Oct. 2007), p. 103303. DOI: 10.1063/1.2804074.

[27] Jungchul Lee, Andrea K. Bryan, and Scott R. Manalis. “High precision particle mass sensing using microchannel resonators in the second vibration mode”. In: *Review of Scientific Instruments* 82.2 (Feb. 2011), p. 023704. DOI: 10.1063/1.3534825.

[28] Søren Dohn et al. “Enhanced functionality of cantilever based mass sensors using higher modes”. In: *Applied Physics Letters* 86.23 (June 2005), p. 233501. DOI: 10.1063/1.1948521.

[29] Selim Olcum et al. “High-speed multiple-mode mass-sensing resolves dynamic nanoscale mass distributions”. In: *Nature Communications* 6.1 (May 2015). DOI: 10.1038/ncomms8070.

[30] Joseph C. Doll, Sung-Jin Park, and Beth L. Pruitt. "Design optimization of piezoresistive cantilevers for force sensing in air and water". In: *Journal of Applied Physics* 106.6 (Sept. 2009), p. 064310. DOI: 10.1063/1.3224965.

[31] John E. Sader, Jungchul Lee, and Scott R. Manalis. "Energy dissipation in microfluidic beam resonators: Dependence on mode number". In: *Journal of Applied Physics* 108.11 (Dec. 2010), p. 114507. DOI: 10.1063/1.3514100.

[32] John E. Sader, Thomas P. Burg, and Scott R. Manalis. "Energy dissipation in microfluidic beam resonators". In: *Journal of Fluid Mechanics* 650 (Mar. 2010), pp. 215–250. DOI: 10.1017/s0022112009993521.

[33] D. S. Greywall et al. "Evading amplifier noise in nonlinear oscillators". In: *Physical Review Letters* 72.19 (May 1994), pp. 2992–2995. DOI: 10.1103/physrevlett.72.2992.

[34] J. L. Arlett and M. L. Roukes. "Ultimate and practical limits of fluid-based mass detection with suspended microchannel resonators". In: *Journal of Applied Physics* 108.8 (Oct. 2010), p. 084701. DOI: 10.1063/1.3475151.

[35] Sung-Jin Park, Joseph C. Doll, and Beth L. Pruitt. "Piezoresistive Cantilever Performance—Part I: Analytical Model for Sensitivity". In: *Journal of Microelectromechanical Systems* 19.1 (Feb. 2010), pp. 137–148. DOI: 10.1109/jmems.2009.2036581.

[36] *Silvaco Deckbuild*. 2019. URL: www.silvaco.com.

[37] Yozo Kanda. "Piezoresistance effect of silicon". In: *Sensors and Actuators A: Physical* 28.2 (July 1991), pp. 83–91. DOI: 10.1016/0924-4247(91)85017-i.

[38] Marc Sansa et al. "Frequency fluctuations in silicon nanoresonators". In: *Nature Nanotechnology* 11.6 (Feb. 2016), pp. 552–558. DOI: 10.1038/nnano.2016.19.

[39] James A. Barnes et al. "Characterization of Frequency Stability". In: *IEEE Transactions on Instrumentation and Measurement* IM-20.2 (1971), pp. 105–120. DOI: 10.1109/tim.1971.5570702.

[40] BBI Solutions. *Technical datasheet of 20nm, 40nm, 60nm, 80nm-diameter gold nanoparticles*. 2019. URL: https://www.bbisolutions.com.

Appendix A

Nomenclature of geometrical and material properties of SNR

L_{res}	SNR length
w_{res}	SNR width ($2w_c + 2w_{ext} + w_{int}$)
t	SNR total thickness ($2t_{lid} + t_c$)
w_c	Channel width
t_c	Channel thickness
t_{lid}	Lid thickness
w_{ext}	External wall width separating the channel to the SNR sidewalls
w_{int}	Internal wall width separating the buried channel legs
L_c	Buried channel length
ρ_{Si}	Density of silicon
L_{pzr}	Piezoresistor length
w_{pzr}	Piezoresistor width ($\frac{w_{res}-w_{wall}}{2}$)
t_{pzr}	Piezoresistor thickness ($\sim$ junction depth)
ρ_{water}	Density of water
k	Stiffness of cantilever
m_{eff}	Effective mass
S_ϕ	PSD of total phase noise
x_c	RMS vibration amplitude
ω_r, f_r	Resonance frequency
Q	Quality factor
BW	Measurement bandwidth
R_x	Displacement responsivity of the piezoresistor (V/m)

R_m	Mass responsivity of the cantilever (mHz/ag)
P_d	Power dissipation of piezoresistor
k_B	Boltzmann constant
V_b	Piezoresistor bias voltage
T	Cantilever temperature
α	Hooge's factor
β^*	Process dependent sensitivity factor
γ	Extra resistance factor due to contacts and traces
π_l	p-type piezoresistivity factor along <100> direction
R_S	Sheet resistance (Ohm/square)
N_z	Total number of carriers per unit area
N_p	Dopant concentration (per cc)
E	Young's modulus of silicon

Table A.1: Nomenclature of geometrical and material properties of SNR.

Appendix B

Measurement setups and LabVIEW scripts for SNR operation

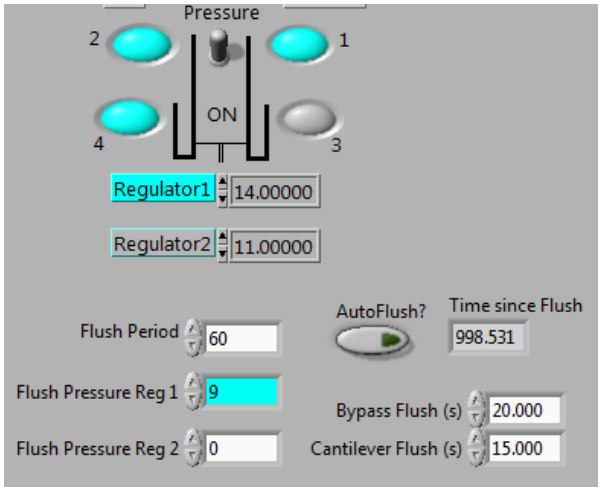

Figure B.1. LabVIEW script used to control pressure levels in the four vials connected to the inlets of the two bypass channels of either a single-resonator SNR or a pSNR array. The two inlets on the left are connected to the sample load bypass channel and are pressurized in pinched flow mode using regulator 1. One of the two vials connected to the sample collect bypass channel (on the right) is pressurized at a high pressure state, while the other pressure regulator (2, gray in the figure) is set to a lower value to control the speed of particles flowing through the buried channel. The AutoFlush mode is used to automatically switch the flow direction through the buried channel within a certain time period. This mode is used when the nanoparticles is the sample are heavy or sticky: in one period, first the sample flows through the buried channel from the sample-load to the sample-collect bypass, then some buffer (e.g. water) or cleansing fluid (e.g. bleach) flows backwards removing any residual particles that could get trapped at the cantilever's tip and preventing clogging of the device.

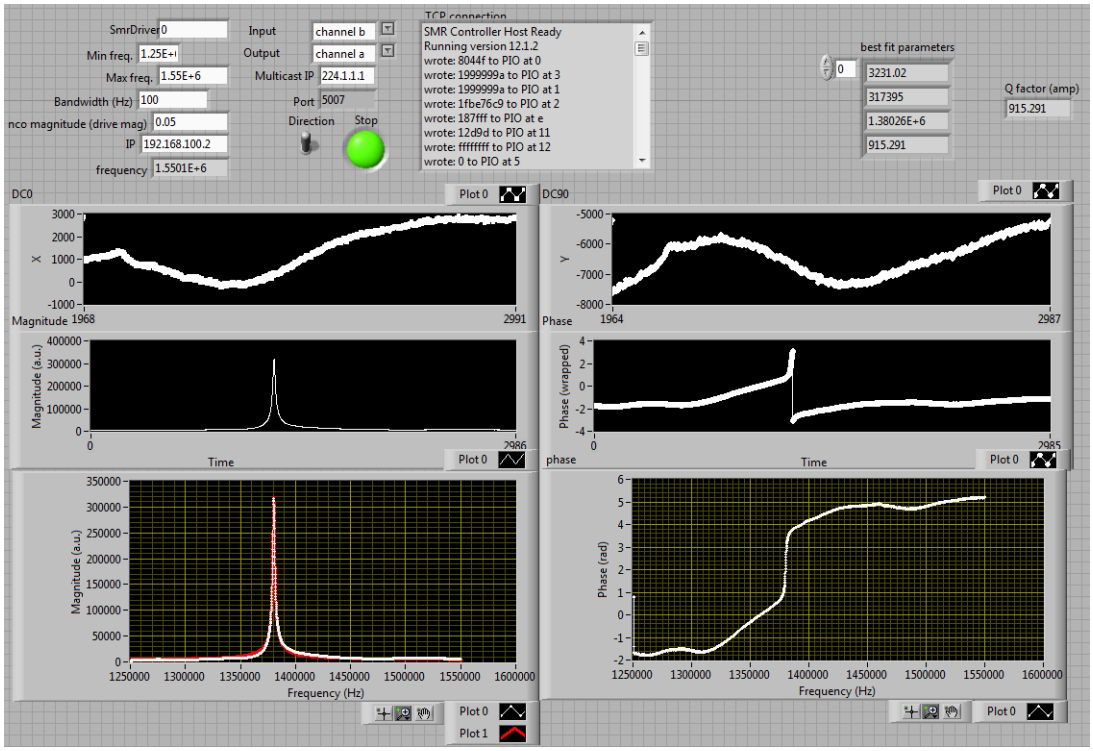

Figure B.2. LabVIEW script used to drive the piezoelectric ceramic in open-loop mode. This script is used to generate an electrical signal that drives the piezoelectric ceramic at different frequencies within a range that is set by the user. It is also possible to set the frequency step (bandwidth) and the driving signal magnitude. The magnitude and phase responses of the SNR resonator are measured through the optical or piezoresistive setups and they are analyzed to extract the resonance frequency and quality factor of the oscillator. In this example, a SNR0-type single-resonator SNR (see table 1.1) with de-ionized water flowing through the buried channel has a resonance frequency of $f_r = 1.38 MHz$ and a quality factor $Q = 915$.

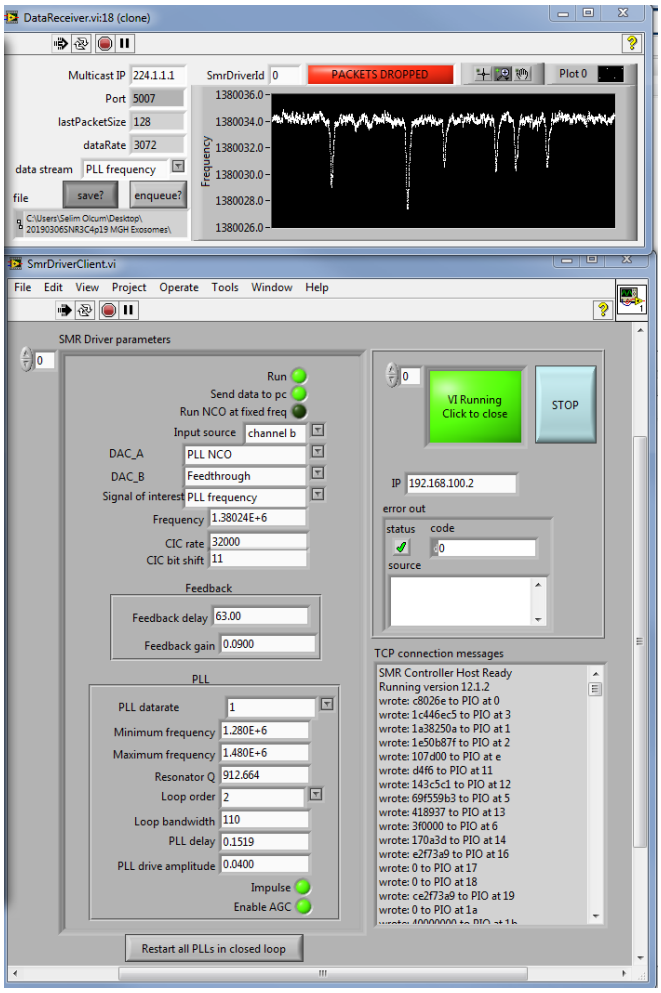

Figure B.3. LabVIEW script used to drive the piezoelectric ceramic in closed-loop mode. This script is used to generate an electrical signal that drives the piezoelectric ceramic at the resonance frequency of the SNR in use, previously measured using the script described in figure B.2. The SNR device used in this example has a first flexural mode resonance frequency of $f_r = 1.38MHz$ and a quality factor $Q = 915$, the feedback mode is set to PLL, the driving amplitude can be set to increase the signal-to-noise ratio or to decrease the probability of trapping events, the measurement sampling rate R_s is defined as the FPGA clock frequency ($100MHz$) divided by the CIC filter rate and the PLL datarate [29] and for this example is $R_s = \frac{100MHz}{CIC_{rate}PLL_{datarate}} = \frac{100MHz}{32{,}000 \cdot 1} = 3125Hz$. The Butterworth-type low-pass filter embedded in the PLL feedback system to remove high-frequency noise components can also be adjusted according to the measurement needs by setting its selectivity (filter order, m) and bandwidth. The latter is set according to a tradeoff between signal-to-noise ratio and particles speed through the buried channel (chapter 3, [29]). The window at the top of the figure shows the resonance frequency baseline ($f_r = 1.38MHz$) and six resonance frequency shifts caused by nanoparticles flowing through the SNR buried channel. This script is also used to simultaneously lock an array of N resonators in pSNR devices. Each resonator's settings can be adjusted independently.

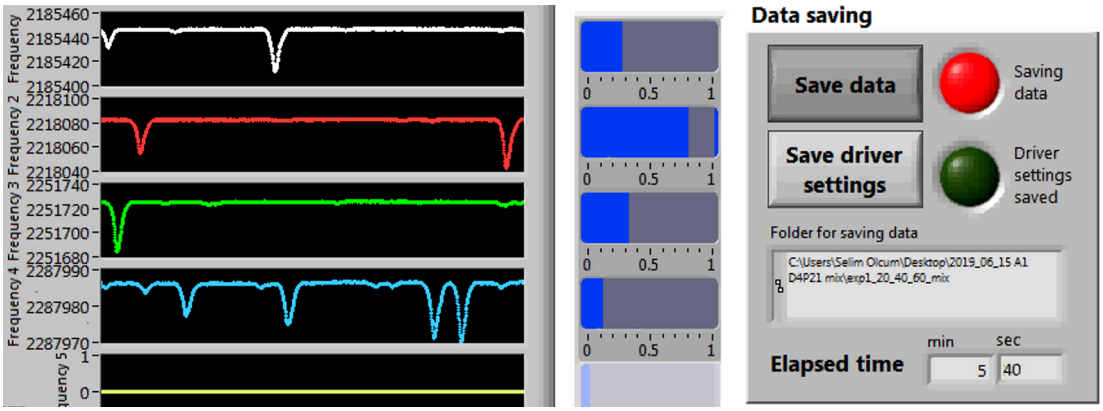

Figure B.4. LabVIEW script used to display and save the resonance frequency shifts of N simultaneously locked resonators in a pSNR array. This example shows four resonators embedded in a pSNR array of type *A1* being locked simultaneously in their first flexural mode. Their resonance frequency baselines are shifted when nanoparticles flow through the buried channel of SNRs (colored plots). This script allows to measure the noise affecting the resonance frequency baseline in real time (blue horizontal bars).

Appendix C

Results of optimization algorithm

	SNR0	*SNR1*	*SNR2*	*SNR3*
f_r	1.5 MHz	2.5 MHz	3.5 MHz	5 MHz
δm	0.712094 ag	0.375984 ag	0.246879 ag	0.158066 ag
δm_{th}	0.71192 ag	0.375926 ag	0.246851 ag	0.158052 ag
L_{res}	32.3 μm	25 μm	21.1 μm	17.7 μm
w_{res}	2.9 μm	2.9 μm	2.9 μm	2.9 μm
t	1.1 μm	1.1 μm	1.1 μm	1.1 μm
w_c	0.7 μm	0.7 μm	0.7 μm	0.7 μm
t_c	0.7 μm	0.7 μm	0.7 μm	0.7 μm
w_{ext}, w_{int}	0.5 μm	0.5 μm	0.5 μm	0.5 μm
t_{lid}	0.2 μm	0.2 μm	0.2 μm	0.2 μm
L_{pzr}	10.5 μm	8.6 μm	7.2 μm	5.6 μm
w_{pzr}	1.2 μm	1.2 μm	1.2 μm	1.2 μm
t_{pzr}	0.1 μm	0.1 μm	0.1 μm	0.1 μm
R_{pzr}	5.4$k\Omega$	5.01$k\Omega$	4.11$k\Omega$	2.88$k\Omega$
N_p	4.2 $10^{19} at/cm^3$	3.8 $10^{19} at/cm^3$	4 $10^{19} at/cm^3$	4.9 $10^{19} at/cm^3$
R_S	270 $\Omega/\square$	299.4 $\Omega/\square$	285.9 $\Omega/\square$	240 $\Omega/\square$
V_b	0.4V	0.3V	0.3V	0.2V
P_d	6.4 μW	4.6 μW	3.8 μW	3.3 μW
T_{rise}	0.14 $°C$	0.09 $°C$	0.07 $°C$	0.06 $°C$
Attenuation	-3.9 dB	-5.4 dB	-6 dB	-6 dB

Table C.1: Design parameters for different types of single-resonator SNR devices (table 1.1) obtained using the optimization algorithm described in chapter 2.

	SNR0	SNR1	A1 #10
f_r	1.5 MHz	2.5 MHz	2.5 MHz
δm	0.941656 ag	0.474646 ag	0.404204 ag
δm_{th}	0.941407 ag	0.474569 ag	0.404136 ag
L_{res}	31.6 μm	24.3 μm	25.1 μm
w_{res}	4.5 μm	3.9 μm	3.5 μm
t	1.1 μm	1.1 μm	1.1 μm
w_c	1 μm	0.7 μm	1 μm
t_c	0.7 μm	0.7 μm	0.7 μm
w_{ext}, w_{int}	1 μm, 0.5 μm	1 μm, 0.5 μm	0.5 μm
t_{lid}	0.2 μm	0.2 μm	0.2 μm
L_{pzr}	11.6 μm	9.1 μm	9.1 μm
w_{pzr}	2 μm	1.7 μm	1.5 μm
t_{pzr}	0.1 μm	0.1 μm	0.1 μm
R_{pzr}	4.66 $k\Omega$	4.55 $k\Omega$	4.72 $k\Omega$
N_p	3.2 $10^{19} at/cm^3$	3.1 $10^{19} at/cm^3$	3.4 $10^{19} at/cm^3$
R_S	339.4 $\Omega/\square$	353.1 $\Omega/\square$	329.3 $\Omega/\square$
V_b	0.4V	0.3V	0.3V
P_d	8.5 μW	5.5 μW	5.3 μW
T_{rise}	0.16 $°C$	0.1 $°C$	0.1 $°C$
Attenuation	-3.4 dB	-5 dB	-5.2 dB

Table C.2: Design parameters for single-resonator SNR devices and one of the resonators in the *A1* pSNR device (see tables 1.1, 1.2) obtained using the optimization algorithm described in chapter 2 after the parametric sweep study and using the dopant profile simulated with the SILVACO software.

Appendix D

T7-like virus buoyant mass measurement and limit of detection threshold

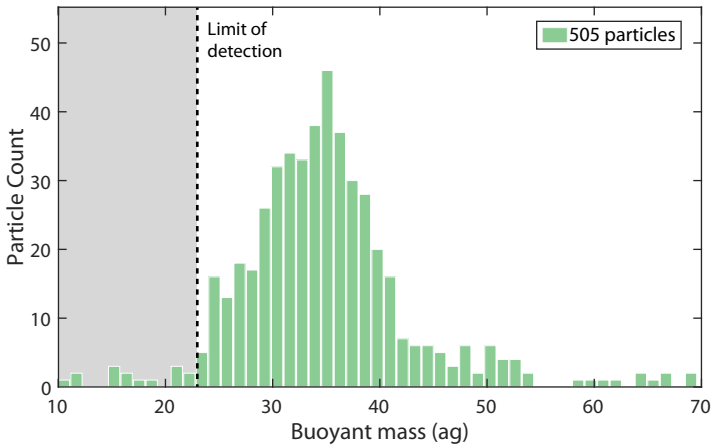

Figure D.1. Estimated buoyant mass of a T7-like virus measured in filtered ($200nm$) de-ionized water using a single-resonator SNR of type $SNR3$. 505 particles were counted during a two hours experiment. Particles were flowing slowly to be conservative with the resonance frequency shift peak height accuracy: for a measurement bandwidth $BW = 110Hz$ the average transit time was $220ms$, two times larger than the limit explored in chapter 3. The T7-like virus has a head which is $60nm$ in diameter and its estimated average buoyant mass is $35ag$. For this device the limit of detection threshold set in the post-processing MATLAB script is $23ag$. This value is typically higher than the minimum mass limit of detection extracted through the Allan deviation analysis and it is set by the user; the code will discard any random resonance frequency fluctuation below this threshold.

Appendix E

Flaws of pSNR current technology

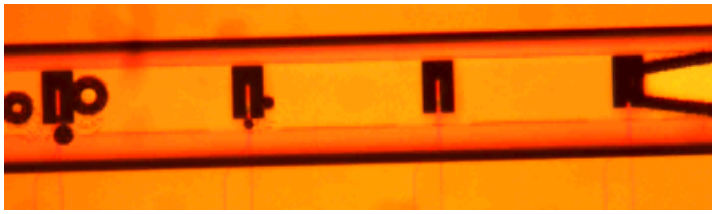

Figure E.1. Optical microscope image of a pSNR device showing air bubbles leaking into the de-ionized water filled vacuum chamber were resonators are sealed in. During operation of this device, the vacuum sealing between Silicon and the glass top layer got damaged and the buffer fluid that was running trough the channels of the device leaked into the vacuum chamber; air was then forced to flow through the buried channel and consequently ended up into the water-filled vacuum chamber. This particular technological flaw that does not affect single-resonator SNR devices probably may be due to a lower distance in pSNR between the vacuum chamber and the bypass channels: the contact area between the glass and Silicon layers is then reduced in pSNR with respect to single-resonator SNR meaning that the bonding is less effective.

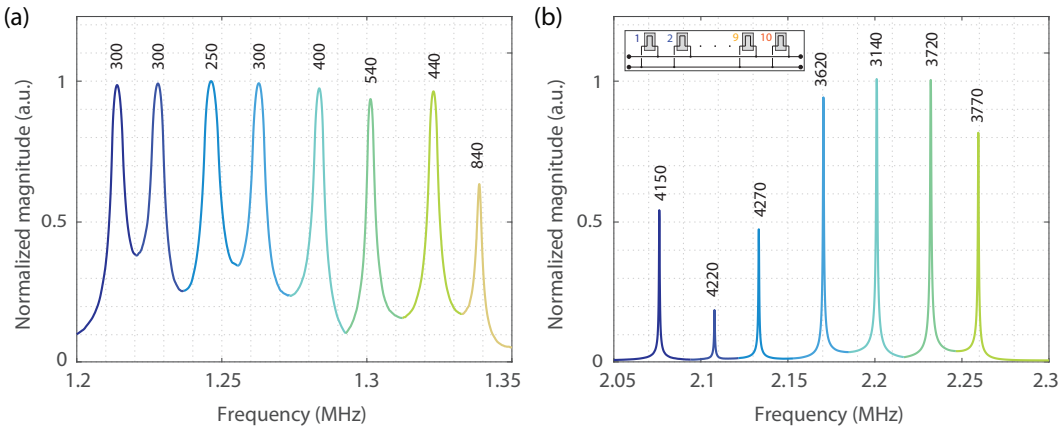

Figure E.2. Open-loop frequency sweep of two parallel SNR arrays of type showing the difference between a low quality factor device of type *A0* with 8 resonators working in piezoresistive mode (a) and a high quality factor device of type *A1* with 7 resonators working in piezoresistive mode (b). Resonance frequencies are equidistant in each pSNR array but the overlapping between neighboring peaks is affected by the quality factor. Cross-talk between adjacent resonators worsen the device performances in terms of signal-to-noise ratio and absolute mass sensitivity and I have observed the effect to be more prominent for arrays whose resonators have quality factors $Q < 1{,}000$. The inset of the figure on the right shows a schematics of a pSNR device; the colors used in the plots follow the same scheme as the SNR index colors in the inset. The quality factors of all active resonators are reported above each resonance peak.